A NUMERICAL STUDY ON THE DEFORMATION OF LIQUID-FILLED CAPSULES WITH ELASTIC MEMBRANES IN SIMPLE SHEAR FLOW

SUI YI
(*B. Sci., University of Science and Technology of China*)

A THESIS SUBMITTED

FOR THE DEGREE OF DOCTOR OF PHILOSOPHY

DEPARTMENT OF MECHANICAL ENGINEERING

NATIONAL UNIVERSITY OF SINGAPORE

2008

ACKNOWLEDGEMENTS

I would like to express my sincere gratitude to my Supervisors, Associate Professor H. T. Low, Professor Y. T. Chew and Assistant Professor P. Roy, for their invaluable guidance, encouragement and support on my research and thesis work.

Moreover, I would like to give my thanks to Professor C. S. Peskin (NYU, USA), Professor Z. L. Li (NCSU, USA) and Professor Z. G. Feng (XU, USA) for their helpful suggestions and discussions on my research. I also want to thank Dr. H. B. Huang, Dr. N. S. Liu, Dr. X. Shi and other colleagues in the Fluid Mechanics group who helped me a lot during the period of my research.

Many people have stood behind me throughout this work. I am deeply grateful to my wife, Chaibo, my parents and my sister, for their love and their confidence in me.

Finally, I am grateful to the National University of Singapore for granting me the Research Scholarship and the precious opportunity to pursue a Doctor of Philosophy degree.

Table of Contents

SUMMARY

In this thesis, a hybrid numerical method was developed to study the flow-induced deformation of capsules. Based on the numerical model proposed, the transient deformation of capsules, which consist of Newtonian liquid drops enclosed by elastic membranes, in simple shear flow was studied. Effects of membrane bending stiffness, inertia and shear rate on the capsule deformation were investigated.

In the hybrid method, the immersed boundary concept was developed in the framework of the lattice Boltzmann method, and the multi-block strategy was employed to improve the accuracy and efficiency of the simulation. The present method was validated by comparison with several benchmark computations. The results showed that the present method is accurate and efficient in simulating two-dimensional solid and elastic boundaries interacting with fluids.

Based on the hybrid method, the transient deformation of two-dimensional liquid capsules, enclosed by elastic membranes with bending rigidity, in shear flow was studied. The results showed that for capsules with minimum bending-energy configurations having uniform curvature, the membrane carries out tank-treading motion. For elliptical and biconcave capsules with resting shapes as minimum bending-energy configurations, it was quite interesting to find that with the bending stiffness increasing or the shear rate decreasing, the capsules' motion changes from tank-treading mode to tumbling mode, and resembles Jeffery's tumbling mode at large bending stiffness.

Inertia effect on the transient deformation of two-dimensional liquid-filled capsule with elastic membrane in simple shear flow was studied. The simulation results

showed that the inertia effect gives rise to a transient process, in which the capsule elongation and inclination overshoot and then show dampened oscillations towards the steady states. Inertia effect also promotes the steady deformation, and decreases the tank treading frequency of the capsule. Furthermore, inertia strongly affects the flow structure and vorticity field around and inside the capsule.

The hybrid method was extended to three-dimensional, and a finite element model was incorporated to obtain the forces acting on the membrane nodes of the three-dimensional capsule which was discretized into flat triangular elements. The present method was validated by studying the transient deformation of initially spherical and oblate spheroidal capsules with various membrane laws under shear flow. The transient deformation of capsules with initially biconcave disk shape was also simulated. The unsteady tank treading motion was followed for a whole period in the present work.

The dynamic motion of three-dimensional capsules in shear flow was investigated. The results showed that spherical capsules deform to stationary configurations and then the membranes rotate around the liquid inside (steady tank-treading motion). Such a steady mode was not observed for non-spherical capsules. It was shown that with the shear rate decreasing, the motion of non-spherical capsules changes from the swinging mode (the capsule undergoes periodic shape deformation and inclination oscillation while its membrane is rotating around the liquid inside) to tumbling mode.

NOMENCLATURE

Roman Letters

a	equivalent radius
a_i	shape parameter
b_i	shape parameter
B	width of a capsule
c	velocity $\Delta x/\Delta t$
c_i	shape parameter
c_s	speed of sound
C	ratio of membrane shear elasticity modulus and membrane dilation modulus
C_d	drag coefficient
C_l	lift coefficient
d_i	shape parameter
D_{xy}, D_{xz}	Taylor shape parameter
$\mathbf{e}_i$	particle velocity vector along direction i
E	shear elasticity modulus
$E_{\boldsymbol{B}}$	bending modulus
$E_{\boldsymbol{b}}$	reduced bending modulus
$\mathbf{f}$	Eulerian fluid force density
f	tank-treading frequency
f_i	particle distribution function
f_i^{eq}	equilibrium particle distribution function
$\mathbf{F}$	Lagrangian boundary force
F_d	drag force
F_l	lift force
I_1, I_2	strain invariants

G	dimensionless shear rate
k	shear rate
$l(t)$	instantaneous arc distance along the membrane
L	length of a capsule
m	bending moment
$\mathbf{n}$	normal direction
p	pressure
q	transverse shear tension
r	distance between the Lagrange and Eulerian nodes divided by the Eulerian grid space
R	volume adjusting factor
Re	Reynolds number
$\mathbf{s}$	spatial position vector in Lagrangian frame
St	Strouhal number
Δt	time step
$\mathbf{t}$	tangential direction
t	time
$\mathbf{T}$	membrane tension
$\mathbf{u}$	fluid velocity vector
U	characteristic velocity
U_t	average tank-treading velocity
U_∞	incoming fluid velocity
V_e	area of the element
W	strain energy density
$\mathbf{x}$	spatial position vector in Eulerian frame
Δx	lattice space

Greek Letters

α	angle of attack
θ	inclination angle of a capsule
λ	principle strain
μ	fluid viscosity
ν	kinetic fluid viscosity
δ	Dirac delta function
ρ	fluid density
ε	capillary number
ω	normalized vorticity magnitude
ω_i	weight coefficients for the equilibrium distribution function
Ω	fluid domain
Γ	Lagrangian boundary

Superscriprs

eq	local equilibrium
n	normal part
f	fine grid
c	coarse grid
t	tangential part

Subscriprs

i	the component in direction $\mathbf{e}_i$
xy	x-y plane
xz	x-z pane
0	initial state

Abbreviations

2D	two-dimensional
3D	three-dimensional
ALE	arbitrary Lagrangian Eulerian
BEM	boundary element method
IBM	immersed boundary method
LBE	lattice Boltzmann equation
LBM	lattice Boltzmann method
NH	Neo-hookean
SK	Skalak
ZT	Zero-thickness
RBC	Red blood cell

LIST OF FIGURES

LIST OF TABLES

Chapter 1 Introduction

1.1 General background

Capsules consisting of thin elastic or incompressible membranes enclosing viscous Newtonian liquid are often employed as models for many kinds of particles, including biological cells, eggs, lipid vesicles, etc. The flow-induced deformation of such a capsule has attracted much attention in the past few decades. The physics involved is important not only in fundamental research, but also in medical and industrial applications. For example, in blood diseases like cerebral malaria and sickle cell anemia, red blood cells lose their ability to deform and often block the capillaries due to the membranes becoming stiffer. To design clinical therapies for such blood diseases, it is necessary to understand how the interfacial mechanical properties affect the deformation of cells under flow. The knowledge is also important in other areas like microencapsulation to design capsules with desired properties. Furthermore, it is the first step to model more complex flow situations which involve capsule suspensions, such as human microcirculation, cell filtration and drug delivery.

1.2 Motion of a capsule in shear flow

1.2.1 Different motion modes

The dynamic motion of a capsule under shear flow has been studied experimentally, theoretically and numerically. Two types of motion are well-known: the tank-treading mode and the tumbling mode.

In the tank-treading mode, the capsule deforms to a steady configuration then the membrane rotates around the liquid inside. Schmid-Schönbein and Wells (1969), as well as Goldsmith (1971) were the first to experimentally demonstrate that red blood cells carry out tank-treading motion in shear flow, when the matrix fluid is much more viscous than the internal liquid of the cell and the shear rate is high. The tank-treading motion has also been observed in subsequent experiments of red blood cells (Fischer et al. 1978; Tran-Song-Tay et al.1984) or vesicles (de Hass et al. 1997) in shear flow. Vesicles are liquid-filled capsules with incompressible membrane, which has no shear elasticity. With small deformation theory, Barthès-Biesel (1980) as well as Barthès-Biesel and Rallison (1981) first predicted the tank-treading motion of spherical liquid-filled capsules with elastic or incompressible membranes in shear flow. The tank-treading motion has also been observed in studies by numerical simulation (Pozrikis 1995; Kraus et al. 1996; Eggleton and Popel 1998; Lac et al. 2004). The numerical simulations were not limited to small deformation.

In the tumbling mode, a capsule flips continuously. The tumbling motion of red blood cells in shear flow has been observed in experiments when the viscosity ratio of the internal liquid to the external liquid is high (Pfafferott et al. 1985) or the shear rate is low (Abkarian et al. 2007). The tumbling motion has also been observed, on non-spherical capsules, in studies by theoretical analysis (Keller and Skalak 1982; Misbah 2006; Skotheim and Secomb, 2007) as well as by numerical simulation (Ramanujan and Pozrikis 1998; Biben and Misbah 2003; Beaucourt et al. 2004).

Besides these two modes, a new “swinging” mode has been observed in recent experiments for non-spherical capsules (Walter 2001; Abkarian et al. 2007). The

swinging mode is similar to the tank-treading mode, because the capsule's membrane also rotates around the liquid inside. The difference from the tank-treading mode is that when the membrane is rotating, the capsule undergoes periodic shape deformation and inclination oscillation. The swinging mode has also been predicted theoretically (Misbah, 2006; Abkarian et al. 2007; Skotheim and Secomb, 2007; Noguchi and Gompper 2007) and numerically (Ramanujan and Pozrikis 1998; Noguchi and Gompper 2007).

The dynamic motion of a capsule under shear flow has been studied extensively. Several factors have been identified important in determining a capsule's motion mode, including the viscosity ratio of the internal fluid and the external fluid, the membrane viscosity, the membrane bending stiffness and the shear rate.

1.2.2 Effect of viscosity ratio

In shear flow, it has been found that capsules immersed in a low viscosity fluid tumble continuously, and capsules immersed in a fluid with sufficiently high viscosity carry out tank-treading motion. Goldsmith and Marlow (1972) were the first to experimentally observe this phenomenon on red blood cells. Later on, Pfafferott et al. (1985) found in experiments that when a red cell was subjected to shear flow, it underwent tank-treading motion approximately when the viscosity ratio (defined as the ratio of the internal fluid viscosity to the external fluid viscosity in this thesis) was less than two, and tumbling motion for higher viscosity ratios.

Keller and Skalak (1982) theoretically analyzed the dynamic motion of an ellipsoidal capsule in simple shear flow. It was found that for a capsule with a given

geometry, the transition from tank-treading mode to tumbling mode depends on the viscosity ratio between internal fluid and external fluid, and it is independent of shear rate. In Keller and Skalak's theory, the capsule was assumed to have a fixed shape. Rioual et al. (2004) also predicted this viscosity ratio induced transition with another analytical model, which was based on general considerations and does not resort to the explicit computation of the full hydrodynamic field inside and outside the vesicle.

This viscosity ratio dependent transition has also been recovered in numerical studies by Pozrikidis and co-workers (Ramanujan and Pozrikids, 1998; Pozrikidis, 2003) with boundary element method, as well as by Misbah and co-workers (Biben and Misbah, 2003; Beaucourt et al. 2004) with advected-field approach.

1.2.3 Effect of membrane viscosity

Barthès-Biesel and Sgaier (1985) theoretically studied liquid-filled capsules with viscoelastic membranes in shear flow. A regular perturbation solution of initially spherical capsules undergoing small deformation was obtained. It was found that with a purely viscous membrane (infinite relaxation time) the capsule deforms into an ellipsoid with a continuous tumbling motion; when the membrane relaxation time was of the same order as the shear time, the particle reaches a steady ellipsoidal shape with an inclination angle between 0° and 45°.

Noguchi and Gompper (2004, 2005, 2007) numerically studied vesicles with viscous membranes in simple shear flow. It was found that increasing the viscosity of

membrane will cause the capsule's motion change from tank-treading mode to tumbling mode.

In fact, the tank-treading to tumbling transition may be induced by either increasing the viscosity ratio or increasing the membrane viscosity. In both cases due to the fact that the viscosity increases, the transfer of shear torque to the membrane (or its underlying bulk) becomes more and more difficult (because of increasing dissipation), and then the capsule would behave like a solid body which then undergoes tumbling.

1.2.4 Effect of membrane bending stiffness

For liquid filled capsules enclosed by elastic membrane, flow induced deformation causes the development of not only in-plane elastic tensions, but also bending moments accompanied by transverse shear tensions. The interfacial bending moments develop physically due to the non-zero membrane thickness; the bending moments may also be generated because the membrane has a preferred configuration due to its certain structure. The bending moments is expressed by a constitutive law which involves the instantaneous Cartesian curvature tensor, curvature of the minimum bending-energy configuration, and the bending modulus. The bending modulus is generally independent of the in-plane elasticity modulus, and describes the flexural stiffness of the membrane.

For fluid capsules enclosed by lipid-bilayer membrane, such as red blood cells, the bending stiffness has been found to be quite important in determining the equilibrium configuration and shape oscillations (Fung, 1965; Lipowsky, 1991). For non-

equilibrium conditions such as capsules under flow, membrane bending rigidity also plays a significant role in avoiding the development of wrinkling and folding. For capsules whose membrane has a preferred configuration, it can be expected that bending stiffness will ensure that the capsule shape should not deviate greatly from its preferred profile. It is thus meaningful to investigate the effect of bending stiffness on the flow-induced deformation of liquid filled capsules enclosed by elastic membrane.

However, the bending effect has not been explored much and most previous studies neglected bending resistance. The numerical study of Pozrikidis (2001) of liquid-filled elastic capsules in simple shear flow, as well as Kwak and Pozrikids (2001) of axisymmtric capsules in uniaxial extensional flow showed that bending stiffness has significant rounding effect on the steady configuration of capsules. However, an important restriction in their studies was the requirement that the minimum bending-energy shape has uniform curvature. So far, there is no study on the transient deformation of elastic capsules whose minimum bending-energy configuration has non-uniform curvature.

1.2.5 Effect of shear rate

For a capsule in shear flow, it has been long recognized that the deformation of the capsule will be larger at higher shear rate. In the well know theory of Keller and Skalak (1982), it was found that for a capsule with a given geometry, the transition from tank-treading mode to tumbling mode depends on the viscosity ratio and it was independent of shear rate.

Recently, Walter et al. (2001) studied synthetic microcapsules, which were not perfectly spherical, in shear flow by experiment. It was found that during the tank-treading motion of the membrane, the capsule undergoes periodic shape deformation and inclination oscillation; the inclination oscillation amplitude increases as the shear rate decreases. Similar motion has also been found on red blood cells in shear flow by Abkarian et al. (2007): the cells present an oscillation of their inclination superimposed to the tank-treading motion, and the tank-treading-to-tumbling transition can be triggered by decreasing the shear rate. These novel experimental findings show that in shear flow, the dynamics of these capsules depends not only on viscosity ratio, but also on shear rate. Obviously, these findings cannot be recovered by the theory of Keller and Skakak (1982), which assumed a fixed configuration of the capsule.

Only recently, there are some pioneering analyses on these phenomena. Based on Keller and Skalak's theory, and further assuming that the membrane elastic energy undergoes a periodic variation during the tank-treading motion, the above experimental findings can be successfully predicted by the theoretical model of Skotheim and Secomb (2007) and Abkarian et al. (2007). Noguchi and Gompper (2007) numerically studied the three-dimensional vesicles with viscous membranes. It was also found that there is a shear-rate induced transition of vesicles' motion from swinging mode to tumbling mode. For liquid-filled capsules with elastic membrane, the shear-rate induced transition of capsules' motion has not been reported in studies with which take the capsule deformation into account.

1.3 Numerical methods

In the dynamic motion of capsules under flow, the fluid-structure interaction plays a key role, which makes theoretical analysis quite difficult. There are several reasons for these difficulties (Barthès-Biesel, 1980): First, the flow problem needs to be represented by an Eulerian reference system and the capsule solid mechanics problem needs a Lagrangian reference system; and the switch between the two representations is rather complex during the flow-induced deformation of the capsules. Second, the position of the capsule membrane, where to impose boundary conditions, is not known a priori. Also, the large elastic deformation theory, which is very complex, needs to be used. Due to these difficulties, in most theoretical studies (Barthès-Biesel, 1980; Barthès-Biesel and Rallison, 1981; Keller and Skalak, 1982; Skotheim and Secomb, 2007; Abkarian et al. 2007), simple geometry or small deformation of the capsules was assumed. As an alternative approach, numerical simulation has attracted much attention and various numerical methods have been developed.

1.3.1 Arbitrary Lagrangian Eulerian method

The arbitrary Lagrangian Eulerian (ALE) method (Hirt. et al., 1974; Liu and Kawachi, 1999; Yue et al., 2007) is a direct strategy to treat fluid-structure interaction, and it is based on body-fitted grid. The boundary of the fluid domain moves with the motion of the fluid-structure interface, and the mesh is reconstructed. The ALE method has been applied to study the bubble growth by Yue et al. (2007). The ALE method has high-order accuracy but is very computationally expensive. For capsules

with complex geometry or under large deformation, the re-meshing procedure would be very difficult and time-consuming.

1.3.2 Advected-field method

The advected-field method, directly inspired by the phase-field approach, was proposed by Biben and Misbah (2003). The local membrane incompressibility is imposed to the phase-field approach, and the shear elasticity of the membrane is not taken into account. Thus the advected-field method is very suitable to deal with the deformation of vesicles, which are liquid drops enclosed by incompressible membranes. However, vesicles are different from capsules which are liquid drops enclosed by elastic membranes. The advected-field approach has been applied to study the tank-treading to tumbling transition of vesicles due to the viscosity contrast (Biben and Misbah, 2003; Beaucourt et al. 2004).

1.3.3 Boundary element method

The boundary element method (BEM) (Pozrikidis, 1992) is most prevailing for studying capsule deformation in Stokes flow. One significant advantage of BEM is that the governing equations are solved only on the capsule interface, and thus the geometrical dimension of the problem can be reduced by one. With BEM, Pozrikidis and co-workers (Pozrikids, 1995; Ramanujan and Pozrikidis, 1998; Pozrikidis, 2001; Pozrikids, 2003) and Lac et al. (2004) have studied the transient deformation of capsules with various shapes and membrane properties, and obtained results

consistent with experiments. The BEM is valid for creeping flow conditions. For capsules with complex shapes, like the biconcave disk, the simulation of tank treading motion was of limited duration because of numerical instabilities due to grid degradation (Ramanujan and Pozrikidis, 1998; Pozrikidis, 2003).

1.3.4 Immersed boundary method

The immersed boundary method (IBM) developed by Peskin (1977; 2002) to simulate blood flow in the heart, is a kind of fixed grid method. In this method, a force density is distributed to the Cartesian mesh in the vicinity of the moving boundary in order to account for the effect of the boundary.

The immersed boundary method was originally developed for modeling interaction between incompressible viscous fluid and elastic boundary, and the force density is calculated from the boundary's constitutive law. However, it has been extended to deal with solid body by Goldstein (1993) and Saiki (1996) by employing a feedback forcing system. The disadvantages of this system are: it causes spurious oscillations and introduces two free parameters which must be determined by the flow conditions. Later, Mohd-Yusof (1997) and Fadlun (2000) proposed the direct forcing method, which has been proven to be more efficient and can be used at higher Reynolds number flows. Distributing force density on a narrow region near the boundary is an inherent feature of the immersed boundary method. This feature makes it necessary to use fine mesh near the boundary, especially at higher Reynolds number flows.

The IBM has been applied to study the deformation of three-dimensional and liquid-filled capsules with elastic membranes in simple shear flow by Eggleton and Popel (1998). In their study, uniform Cartisian mesh was employed, and the capsule response was followed for short times due to heavy computational load.

1.3.5 Lattice Boltzmann method

Unlike traditional CFD methods (e.g., FDM and FVM), the lattice Boltzmann method (LBM) is based on the microscopic kinetic equation for the particle distribution function and from the function, the macroscopic quantities can be obtained. The kinetic nature provides LBM some merits. Firstly, it's easy to program. Since the simple collision step and streaming step can recover the non-linear macroscopic advection terms, basically, only a loop of the two simple steps is implemented in LBM programs. Secondly, in LBM, the pressure satisfies a simple equation of state when simulating the incompressible flows. Hence, it's not necessary to solve the Poission equation by the iteration or relaxation methods as in usual CFD methods when simulating the incompressible flows. The explicit and non-iterative nature of LBM makes the numerical method easy to be parallelized (Chen et al., 1996).

Over the past two decades, the LBM has achieved great progress in fluid dynamics studies (Chen and Doolen, 1998; Yu et al. 2003). The LBM can simulate incompressible flows (Succi et al., 1991; Hou and Zou, 1995) and compressible flows (Yan et al., 1999; Sun 2000; Hinton et al. 2001). The LBM has also been successfully applied to multi-phase/multi-component flows (Grunau et al., 1993; Luo and Girimaji,

2002 and 2003; Asinari and Luo, 2008), flows through porous media (Chen et al., 1991; Pan et al. 2004; Ginzburg 2008), turbulence flows (Benzi and Succi, 1990; Teixeira, 1998; Yu et al., 2006) and particulate flows (Ladd 1994a and 1994b; Qi and Luo, 2003).

The numerical mesh for the standard LBM is the uniform Cartesian grid, which makes LBM not so efficient (case of uniform fine grid) or accurate (case of uniform coarse grid) to achieve high resolution in regions involving large gradient of macro-dynamic variables. Filippova and Hanel (1998, 2000) employed locally refined patches for uniform Cartesian grid in their studies. That means some finer grids are superposed on the basic, coarser grid. Yu and co-workers (Yu et al., 2002; Yu and Girimaji, 2006) (2002) suggested a multi-block method for viscous flows slightly different from Fillippova and Hanel (1998). The whole computational domain was decomposed into several sub-domains. Some sub-domains adopt fine meshes, the others adopt coarse meshes. The coupling of solutions on different meshes is identical to that of Fillippova and Hanel (1998) except the high order fitting for spatial and temporal interpolation is employed when transfer the information from coarse block to nearby fine grid. Another approach, the Taylor series expansion and least squares based lattice Boltzmann method (TLLBM), was proposed by Shu et al. (2003). This method can also be applied to study flow problems using non-uniform mesh. With these approaches, the computational accuracy and efficiency of lattice Boltzmann method has been substantially improved.

The lattice Boltzmann method has been combined with immersed boundary method, named immersed-boundary lattice Boltzmann method (IB-LBM), by Feng

and Michaelides (2004, 2005) for solving rigid particles flow. Peng et al. (2006) applied the multi-block strategy in the IB-LBM, based on the multi-relaxation-time collision scheme of d'Humières (1992) as well as Lallemand and Luo (2000), and studied flow past two-dimensional stationary solid boundaries. The combined method may be promising in studying the deformation of liquid-filled capsules with elastic membranes.

1.4 Objectives and scopes

The aim of the present study was to develop an efficient numerical method and apply this method to study the deformation of liquid-filled capsules with elastic membranes in shear flow. More specific aims were:

1) To develop an accurate and efficient numerical method for simulating fluid-structure interaction problems. The method should be general and could be applied to study flow-induced deformation capsules with arbitrary shapes and various types of membrane constitutive laws. Furthermore, the method should be able to take the inertia effect into account.

2) To apply the proposed method to study the effect of membrane bending stiffness on the transient deformation liquid-filled elastic capsules in shear flow. For the first time, the dynamic motion of capsules with non-spherical minimum bending energy shapes, under various bending rigidity and shear rates would be considered.

3) To apply the proposed method to study dynamic motion of liquid-filled elastic capsules in shear flow. For the first time, the effects of inertia would be considered. The inertia effects on the transient deformation process, steady configuration and tank

treading frequency of the capsule, as well as the flow structure and vorticity field around and inside the capsule, would be studied in detail.

4) To apply the proposed method to study the transient deformation of three-dimensional liquid-filled capsules with elastic membranes in shear flow under a broad range of shear rates. For the first time, the shear rate induced transition of a capsule's motion from tank-treading mode to tumbling mode would be explored.

The numerical method developed in the present study would enable one to study flow-induced deformation capsules with arbitrary shapes and various types of membrane constitutive laws, and the method would be able to take the inertia effect into account. The results of the present study may be meaningful in understanding how the mechanical properties of the membrane, as well as the flow condition, affect the dynamic motion of capsules under flow. The knowledge would enable researchers to use the observed dynamics to measure capsule properties, or use the simulations to suggest parameter regimes for experiments where the properties can be most sensitively deduced. The knowledge may also be useful in biomedical therapy design, as well as in the microencapsulation industry.

Because phenomenon of the deformation of capsules under flow is very complex, it is not practical to consider all the factors in the present numerical studies. There are some assumptions in our study: 1) the internal fluid of the capsule was assumed to be similar to the matrix fluid; 2) the membrane viscosity of the capsule was neglected. The effects of viscosity ratio and membrane viscosity have been discussed earlier.

1.5 Outline of the thesis

In chapter 2, a two-dimensional numerical method was developed for modeling the interactions between an incompressible viscous fluid and moving solid or elastic boundaries. The method was tested by the simulations of flow past a circular cylinder, two cylinders moving with respect to each other, flow around a hovering wing and a circular capsule deforming in simple shear flow.

In chapter 3, the transient deformation of two-dimensional liquid-filled capsules enclosed by elastic membranes with bending rigidity in shear flow was studied numerically, using the method developed in chapter 2. The deformation of capsules with initially circular, elliptical and biconcave resting shapes was studied; the capsules' minimum bending-energy configurations were considered as either uniform-curvature shapes (like circle or flat plate) or their initially resting shapes.

In chapter 4, the transient deformation of two-dimensional liquid-filled capsules with elastic membranes was studied in simple shear flow at small and moderate Reynolds numbers. Inertia effect on the transient deformation process, steady configuration and tank treading frequency of a capsule, as well as the flow structure and vorticity field around and inside a capsule were studied.

In chapter 5, a three-dimensional hybrid method was proposed to study the transient deformation of liquid filled capsules with elastic membranes under flow. The method was validated by studying the transient deformation of initially spherical and oblate-spheroidal capsules with various membrane constitutive laws under shear flow. The effects of inertia on the deformation of three-dimensional capsules in shear

flow, and the deformation of three-dimensional capsules with complex shapes were also studied.

In chapter 6, the dynamic motion of three-dimensional liquid-filled capsules with elastic membranes in shear flow was investigated, by the numerical method developed in chapter 5. The dynamic motion of capsules with initially spherical, oblate spheroidal and biconcave discoid unstressed shapes was studied, under a broad range of shear rates.

Chapter 2 A Two-dimensional Hybrid Immersed Boundary and Multi-block Lattice Boltzmann Method*

The present study of capsules deformation in simple shear flow involves fluid-structure interaction. It is still a challenge to achieve both accuracy and efficiency in simulating fluid-structure interaction. For numerical methods based on body-fitted grid, such as arbitrary Lagrangian Eulerian (ALE) method, the mesh is reconstructed with the motion of the structure. It has high order accuracy but is very computationally expensive. For fixed grid methods, such as the immersed boundary method, re-meshing is not needed, only the variables on the Cartesian mesh near the moving boundary are treated so that the effect of the boundary is considered. However, fine mesh near the moving boundary is needed in the fixed grid methods.

In this chapter, a two-dimensional hybrid numerical method is developed for modeling the interactions between incompressible viscous fluid and moving boundaries. The principle of this method is introducing the immersed boundary concept in the framework of the lattice Boltzmann method. In order to improve the accuracy and efficiency of the simulation, the multi-block strategy is employed so that the mesh near moving boundaries is refined. Besides elastic boundary with a

* Parts of this chapter have been published as "Sui, Y., Chew, Y. T., Roy, P. and Low H. T., A hybrid immersed-boundary and multi-block lattice Boltzmann method for simulating fluid and moving-boundaries interactions, Int. J. Numer. Meth. Fluids, 53: 1727-1754, 2007." Parts of this chapter have been published as "Sui, Y., Chew, Y. T. and Low, H. T., A lattice Boltzmann study on the large deformation of red blood cells in shear flow, Int. J. Mod. Phys. C, 18: 993-1011, 2007."

constitutive law, the method can also efficiently simulate solid moving-boundary interacting with fluid by employing the direct forcing technique. The present method is validated by the simulations of flow past a circular cylinder, two cylinders moving with respect to each other, flow around a hovering wing, as well as the deformation of circular capsules in simple shear flow.

2.1 Numerical method

2.1.1 The lattice Boltzmann method

The lattice Boltzmann method is a kinetic-based approach for simulating fluid flows. It has been developed from the lattice-gas automata and got rapid progress in recent years (Chen and Doolen, 1998; Yu et al., 2003). The lattice Boltzmann method decomposes the continuous fluid flow into pockets of fluid particles which can only stay at rest or move to one of the neighboring nodes. The D2Q9 model using a square lattice with nine possible velocities (see Figure 2.1) is one of the commonly used models in two-dimensional simulation, in which the discrete lattice Boltzmann equation has the form of:

$$f_i(\mathbf{x}+\mathbf{e}_i\Delta t, t+\Delta t) - f_i(\mathbf{x},t) = -\frac{1}{\tau}[f_i(\mathbf{x},t) - f_i^{eq}(\mathbf{x},t)] \tag{2.1}$$

where $f_i(\mathbf{x},t)$ is the distribution function for particles with velocity $\mathbf{e}_i$ at position $\mathbf{x}$ and time t, Δt is the lattice time interval, $f_i^{eq}(\mathbf{x},t)$ is the equilibrium distribution function and τ is the non-dimensional relaxation time.

In the D2Q9 model, the fluid particles have the possible discrete velocities stated as follows:

$$\mathbf{e}_0 = (0,0)$$

$$\mathbf{e}_i = (\cos[\pi(i-1)/2], \sin[\pi(i-1)/2])c \quad \text{for i=1-4}$$

$$\mathbf{e}_i = \sqrt{2}(\cos[\pi(i-9/2)/2], \sin[\pi(i-9/2)/2])c \quad \text{for i=5-8} \tag{2.2}$$

where $c = \Delta x / \Delta t$ and Δx is the lattice spacing.

The equilibrium distribution function $f_i^{eq}(\mathbf{x}, t)$ in the lattice Boltzmann equation is obtained by expanding the Maxwell-Boltzmann distribution function in Taylor series of velocity up to second-order. It is in the form of:

$$f_i^{eq} = E_i(\rho, \mathbf{u}) \tag{2.3}$$

$$\text{with } E_i(\rho, \mathbf{u}) = \omega_i \rho [1 + \frac{\mathbf{e} \cdot \mathbf{u}}{c_s^2} + \frac{\mathbf{uu} : (\mathbf{e}_i \mathbf{e}_i - c_s^2 \mathbf{I})}{2c_s^4}] \tag{2.4}$$

where ω_i are the weighing factors with the values:

$$\begin{cases} \omega_0 = 4/9 & \\ \omega_i = 1/9 & for \quad i = 1-4 \\ \omega_i = 1/36 & for \quad i = 5-8 \end{cases} \tag{2.5}$$

and $c_s = c/\sqrt{3}$ is the sound speed.

The Lattice Boltzmann Equation can recover the incompressible Navier-Stokes equation by Chapman-Enskog Expansion. The relaxation time in LBE is related to the kinematic viscosity in Navier-Stokes equation in the form of:

$$\nu = (\tau - \frac{1}{2}) c_s^2 \Delta t \tag{2.6}$$

It is known that the numerical error in the LBM is proportional to the square of a computational Mach number, $Ma = U_c/c_s$, where U_c is the characteristic velocity. Therefore, it is important to choose a relaxation time that keeps the Mach number

much smaller than unity.

Once the particle density distribution is known, the fluid density and momentum are calculated, using:

$$\rho = \sum_i f_i \tag{2.7}$$

$$\rho \mathbf{u} = \sum_i \mathbf{e}_i f_i \tag{2.8}$$

2.1.2 The Multi-block strategy

Recently, there has been a growing interest in employing the Cartesian grid for complex flow problems. In the standard lattice Boltzmann method, a uniform Cartesian mesh is employed. A challenge of the uniform grid is to offer high resolution near a solid body and to place the outer boundary far away from the body without wasting the grid resolution elsewhere.

Nannelli and Succi (1992) proposed the finite volume lattice Boltzmann scheme to handle Cartesian non-uniform grids. Based on an interpolation strategy, some studies also extended the LBGK method to curvilinear grids (He and Doolen 1997a, 1997b). However, if numerical mesh spacing is very different from the "molecular" lattice, the accuracy of the scheme may decrease in the regions of high gradients of macro-dynamic variables (Filippova and Hanel, 2000).

Filippova and Hanel (1998, 2000) employed locally refined patches for uniform Cartesian grid in their studies. That means some finer grids are superposed on the basic, coarser grid. Yu and co-workers (Yu et al., 2002; Yu and Girimaji, 2006) suggested a multi-block method for viscous flows slightly different from Fillippova

and Hanel (1998). The whole computational domain was decomposed into several sub-domains. Some sub-domains adopt fine meshes, the others adopt coarse meshes. The coupling of solutions on different meshes is identical to that of Fillippova and Hanel (1998) except the high order fitting for spatial and temporal interpolation is employed when transfer the information from coarse block to nearby fine grid. The computational efficiency of lattice Boltzmann method has been substantially improved by the multi-block strategy.

In the present paper, the multi-block lattice Boltzmann method proposed by Yu et al. (2002) is employed. The computational domain is divided into blocks which are connected through the interface. In each block, the constant lattice spacing equals the lattice time interval. On the interface between blocks, the exchange of variables follows a certain relation so that the mass and momentum are conserved and the stress is continuous across the interface.

Consider a two-block system to explain the idea of the multi-block method. The ratio of lattice space between the two blocks is defined as:

$$m = \frac{\Delta x_c}{\Delta x_f} \tag{2.9}$$

where Δx_c and Δx_f are the lattice space of the coarse and fine mesh blocks respectively. For a given lattice space, the fluid viscosity can be obtained from Equation (2.6). In order to keep a constant viscosity, the relaxation parameter τ_f in fine mesh and τ_c in coarse mesh, must satisfy the following relation:

$$\tau_f = \frac{1}{2} + m(\tau_c - \frac{1}{2}) \tag{2.10}$$

The variables and their derivatives on the grid must be continues across the block interface. To keep this continuity, the relation of the density distribution function in the neighboring blocks is proposed as:

$$\tilde{f}_i^c = f_i^{eq,f} + m\frac{\tau_c - 1}{\tau_f - 1}[\tilde{f}_i^f - f_i^{eq,f}] \tag{2.11}$$

$$\tilde{f}_i^f = f_i^{eq,c} + \frac{\tau_f - 1}{m(\tau_c - 1)}[\tilde{f}_i^c - f_i^{eq,c}] \tag{2.12}$$

where $\tilde{f}_i$ is the post-collision density distribution function.

The typical structure of interface is illustrated in Figure 2.2. The fine block boundary, line MN, is in the interior of the coarse block. The coarse block boundary, line AB, is in the interior of the fine block. This arrangement is convenient for information exchange. On the boundary of fine block MN, there is no information on the grid points denoted by the solid symbol ● in Figure 2.2. It is obtained from spatial interpolation based on the information on the grid nodes denoted by the open symbol ○ on the line MN. A symmetric, cubic spline spatial fitting (Yu et al., 2002) is used to avoid spatial asymmetry caused by interpolation:

$$\widetilde{f}(x) = a_i + b_i x + c_i x^2 + d_i x^3, \quad x_{i-1} \le x \le x_i, \quad \text{i} = 1, \ldots, \text{n} \tag{2.13}$$

where the constants (a_i, b_i, c_i, d_i) are determined by using the continuity conditions of f, f', f'' and suitable end conditions such as zero second derivative for f.

Because the fluid particle has the same streaming velocity on each block, the computation marches m steps on the fine-mesh block for every one step on the coarse-mesh block. On the fine block MN, temporal interpolation is needed to

obtain $\widetilde{f}_{\alpha}(t^{n+1/m}, \mathrm{MN})$. A three-point Lagrangian formula (Yu et al., 2002) is used for temporal interpolation.

$$y(t) = \sum_{k=1}^{3} y_k \left(\prod_{\substack{j=1 \\ j \neq k}} \frac{t - t_i}{t_k - t_j} \right) \tag{2.14}$$

2.1.3 The immersed boundary method

In the immersed boundary method (Peskin, 1977 and 2002; Lallemand et al. 2007; Peng and Luo, 2008), two different sets of coordinate system are used. The fluid region is represented by fixed Cartesian grids and the moving boundary immersed in the fluid is decomposed into a set of Lagrangian points. The Lagrangian points are advected by the flow field. The fluid-structure interaction is modeled by distributing a force density to the Cartesian mesh in the vicinity of the moving boundary in order to account for the effect of the boundary.

To explain the immersed boundary method, we consider a mass-less elastic filament with boundary Γ immersed in the fluid domain Ω (see Figure 2.3). The fluid domain Ω is represented by Eulerian coordinates **x**, while the boundary of the filament Γ, is represented by Lagrangian coordinates **s**. Any position on the filament can be written as **X**(**s**, t). The term **F**(**s**, t) represents the filament force density, which is a combination of internal link force induced by deformation and external force. The term **f**(**x**, t) represents the fluid body force density.

The non-slip boundary condition is satisfied by letting the flexible structure move at the same velocity as the fluid around it. That is:

$$\frac{\partial \mathbf{X}(\mathbf{s}, t)}{\partial t} = \mathbf{u}(\mathbf{X}(\mathbf{s}, t), t) \tag{2.15}$$

This motion will cause the filament to deform. The boundary force density **F**(**s**, t) is obtained from the constitutive law of the filament, and distributed to the fluid mesh points near it by a smoothed version of the Dirac Delta function, written as follow:

$$\mathbf{f}(\mathbf{x},t) = \int_{\Gamma} \mathbf{F}(\mathbf{s},t)\delta(\mathbf{x} - \mathbf{X}(\mathbf{s},t))d\mathbf{s} \tag{2.16}$$

where

$$\delta(r) = \begin{cases} \frac{1}{4}(1+\cos(\frac{\pi|r|}{2})) & r \le 2 \\ 0 & r > 2 \end{cases} \tag{2.17}$$

in which *r* equals the distance between the Lagrange and Eulerian nodes divided by the Eulerian grid space. For two-dimensional case, the smoothed version of Dirac Delta function can be written as:

$$\delta(\mathbf{X} - \mathbf{X}_{ij}) = \delta(x - x_{ij})\delta(y - y_{ij}) \tag{2.18}$$

The same smoothed version of the Dirac Delta function is used to obtain the velocities of the Lagrangian nodes on the moving boundary. The mathematical form can be written as follows, which illustrates the implementation of Equation (2.15):

$$\frac{\partial \mathbf{X}}{\partial t} = \int_{\Omega} \mathbf{u}(\mathbf{x},t)\delta(\mathbf{x} - \mathbf{X}(\mathbf{s},t))d\mathbf{x} \tag{2.19}$$

The immersed boundary method is originally developed for modeling interaction between incompressible viscous fluid and elastic boundary with a constitutive law. However, it has been extended to solve solid body immersed in fluid by several researchers. The key procedure is how to generate the force density. Goldstein et al. (1993) and Saiki et al. (1996) proposed a feedback forcing system. However, it causes spurious oscillations and introduces two free parameters which must be determined by the flow conditions.

Mohd-Yusof (1997) and Fadlun et al. (2000) proposed the direct forcing method, which has been proven to be more efficient and can be used at higher Reynolds number flows. The Navier-Stokes equation with a force density in discrete form is written as:

$$\rho(\frac{u_i^{n+1}-u_i^n}{\Delta t}+u_j^n u_{j,i}^n)=-p_{,i}^n+\mu u_{i,jj}^n+\mathbf{f}_i^{n+1} \tag{2.20}$$

If the boundary condition at $t = t^{n+1}$ can be imposed, the force density can be directly obtained from:

$$\mathbf{f}_i^{n+1}=\rho(\frac{u_i^{n+1}-u_i^n}{\Delta t}+u_j^n u_{j,i}^n)+p_{,i}^n-\mu u_{i,jj}^n \tag{2.21}$$

Recently, Feng et al. (2005) has proposed a new direct forcing scheme, in which at $t = t^{n+1}$ the velocity at the Lagrangian point equals the velocity of the solid boundary at the same point, U_i^{n+1}. Thus the force density is calculated from:

$$\mathbf{f}_i^{n+1}=\rho(\frac{U_i^{n+1}-u_i^n}{\Delta t}+u_j^n u_{j,i}^n)+p_{,i}^n-\mu u_{i,jj}^n \tag{2.22}$$

In the original presentation of the method by Mohd-Yusof (1997) and Fadlun et al. (2000), instead of creating a set of Lagrangian boundary points, the force density was computed for a regular node. This node was a point where the velocity was defined when a staging grid was used, or simply a velocity point next to the boundary. The new scheme of Feng et al. (2005) is more efficient for moving boundary problems.

2.1.4 The hybrid immersed boundary and multi-block lattice Boltzmann method

In the present section, the immersed boundary method is combined with the multi-block lattice Boltzmann method. In order to solve the flow field with a force density,

the lattice Boltzmann equation must be modified. Several forms of LBE which can handle a force density have been proposed. Guo's approach (Guo et al., 2002) is more accurate for unsteady flow with force changing with time and space, in which the modified lattice Boltzmann equation is in the form of:

$$f_i(\mathbf{x}+\mathbf{e}_i\Delta t, t+\Delta t) - f_i(\mathbf{x},t) = -\frac{1}{\tau}[f_i(\mathbf{x},t) - f_i^{eq}(\mathbf{x},t)] + \Delta t F_i \tag{2.23}$$

where
$$f_i^{eq} = E_i(\rho, \mathbf{u}^*) \tag{2.24}$$

with
$$\rho\mathbf{u}^* = \sum_i \mathbf{e}_i f_i + \frac{1}{2}\mathbf{f}\Delta t \tag{2.25}$$

$$F_i = (1-\frac{1}{2\tau})\omega_i[\frac{\mathbf{e}_i - \mathbf{u}}{c_s^2} + \frac{(\mathbf{e}_i\cdot\mathbf{u})}{c_s^4}\mathbf{e}_i]\cdot\mathbf{f} \tag{2.26}$$

In the computation in this chapter, a two-grid system is employed. The lattice space ratio between coarse and fine grids equals two. The solid or elastic boundaries are immersed in the fine mesh block. The present procedure for multi-block computation is very similar to that proposed by Yu et al. (2002). The only difference exists in the computation on the fine mesh block. That is a subroutine implementing the immersed boundary method is added before the streaming and collision steps. The computational sequence has been shown in Figure 2.4.

2.2 Validation of the numerical method

2.2.1 Flow passing a circular cylinder

The flow past a circular cylinder is a standard benchmark computation for testing many numerical methods. This case is used to validate our method for solving fluid-

solid boundary problem. The Reynolds number, drag coefficient, lift coefficient and Strouhal number are defined as:

$$\mathrm{Re} = \frac{\rho U_\infty D}{\mu}$$

$$C_d = \frac{F_d}{0.5\rho U_\infty^2 D}$$

$$C_l = \frac{F_l}{0.5\rho U_\infty^2 D}$$

$$St = \frac{f D}{U_\infty} \tag{2.27}$$

where ρ is the fluid density; μ is the fluid viscosity; U_∞ is the incoming velocity, D is the diameter of the cylinder; F_d and F_l are the drag and lift forces, and f is the oscillation frequency. The drag and lift forces can be simply obtained by looking at the x or y component of the force applied by the boundary to the fluid. These of course, are equal to the negative of the drag and lift, by Newton's third law of motion.

The flow is computed at Reynolds number of 100 and 200 using computational domain of 30 × 20. Such size of computational domain has been employed by other researchers, for example Russell and Wang (JCP 2003). The diameter of the cylinder is 1 and its center is located at [10, 10]; $\rho = 1$, $U_\infty = 0.1$. The mesh and block system is illustrated in Figure 2.5. The fine mesh block covers the area from 8 to 16 in x-axis and 8 to 12 in y-axis, which is about 5.3% of the whole computational domain by area. In the fine block, $\Delta x_f = \Delta y_f = \Delta t_f = 0.02$. The other area is covered by coarse mesh blocks, in which $\Delta x_c = \Delta y_c = \Delta t_c = 0.04$. On the far field boundary, the incoming velocity is set to be the velocity boundary condition and the density distribution function is set at its equilibrium state.

Figure 2.6 (a) and (b) present the drag and lift coefficients evolution history. The oscillation frequency of drag is twice that of lift. The stream-function and pressure contours are presented in Figure 2.7 (a, b) and Figure 2.8 (a, b). Figure 2.9 (a, b) presents the vorticity contour around the cylinder. The Karman vortex street is observed in the wake. From Figures 2.7 to 2.9, it is clear that the variables at the interface between blocks are continuous.

The drag coefficient, lift coefficient and Strouhal number are compared with that of previous literatures in Table 2.1. It shows that the present results are within the range of values reported by previous studies.

To demonstrate that the results are grid-independent, numerical simulation for several grids with different sizes were carried out, with the same two-block system. The drag coefficient is used as an indicator for this study. From the results in Table 2.2, the grid resolution of $\Delta x_f = \Delta y_f = 0.02$ is sufficient to capture the important characteristics.

With a fine mesh system covering the whole computational domain, which is actually the original immersed boundary lattice Boltzmann method, a numerical study is carried out on flow past a cylinder at $Re = 100$. The drag coefficient, lift coefficient and Strouhal number are found to be 1.436, 0.343 and 0.166 respectively, which are nearly the same as that of the present multi-block method. However, only about 5.3% of the computational area is covered by fine mesh with the present multi-block method. Computational effort is saved by using less mesh, and furthermore one time step on coarse mesh needs two time steps in fine mesh. The computational effort saved is estimated as:

$$1-\frac{(5.3\%\times 2+0(ib))\times 2+(100\%-5.3\%)}{(100\%\times 2+0(ib))\times 2}\approx 0.71$$

where 0(ib) is the computational effort incurred by implementing the immersed boundary condition, which is a small value compared with the fluid field computation effort. Conversely, it can be expected that under the same computational effort, the present method gives more accurate result as the near boundary region is covered with fine mesh.

2.2.2 Two circular cylinders moving with respect to each other

This example is used to test the present method in simulating solid moving boundaries immersed in fluid. It has been previously studied by Russell and Wang (2003), as well as Xu and Wang (2006). The initial geometry (Figure 2.10) is the same as theirs, and so is the far-field rigid wall boundary condition. The fine mesh block, with bold solid line as the boundary in Figure 2.10, covers the area from -3 to 19 in *x*-axis and -2 to 3.6 in *y*-axis. The other area is covered with coarse mesh. The grid resolutions in both blocks are the same as that in Section 2.2.1. The diameter of both cylinders equals 1, which is also the characteristic length. Each cylinder, oscillates for two periods about its initial position and then moves with respect to each other at the characteristic velocity $U = 0.025$ and $Re = 40$. Compared with Xu and Wang (2006) the same characteristic length is used, however the current characteristic velocity is 1/40 of theirs; so the time scale is 40 times of theirs. The position of the upper cylinder is:

$$x_u=\begin{cases}16-\dfrac{4}{\pi}\sin(\dfrac{\pi t}{160}) & 0\le t\le 640\\ 32-0.025t & 640\le t\le 1280\end{cases}$$

$$y_u = 1.5 \tag{2.28}$$

The position of the lower cylinder is:

$$x_l = \begin{cases} \frac{4}{\pi}\sin(\frac{\pi t}{160}) & 0 \le t \le 640 \\ 0.025t - 16 & 640 \le t \le 1280 \end{cases}$$

$$y_l = 0 \tag{2.29}$$

A non-equilibrium extrapolation method proposed by Guo et al. (2002) has been used to treat the rigid wall boundary condition in this section as well as Sections 2.2.3.

Figure 2.11(a) presents the vorticity contour when the two cylinders are closest to each other, at t = 960; Figure 2.11(b) shows the vorticity field at t = 1280, when the cylinders are separated from each other by a distance of 16. These results qualitatively agree with that of Xu and Wang.

The developing history of the drag and lift coefficients of the upper cylinder is shown in Figure 2.12(a, b), using the same time scale as Xu and Wang. Very good quantitative agreement is observed. From the results it is seen that the drag force increases when the two cylinders are approaching each other, which means they are repulsive. However, they are attracting each other when they move away in close proximity, because the drag force decreases.

This case is further studied with the original immersed boundary lattice Boltzmann method (IBLBM), which employs uniform mesh for the whole computational domain. The grid resolution (IBLBM) is the same as that of the fine block in this section. The temporal evolution of drag and lift coefficients is shown in Figure 2.12(a, b). It is seen that they are nearly the same as the results by the present multi-block method. However, only 24.1% of the computational domain is covered by fine mesh in the

current method; thus computational effort is saved, though not as much as that of Section 2.2.1.

2.2.3 Flow around a hovering wing

A rigid wing undergoing both translational and rotational motion within a rigid box is studied as a more stringent case to validate the present method. The wing has an elliptical shape with chord length c and aspect ratio e. Its positions in one period are shown in Figure 2.13. Mathematically, it is governed by:

$$A(t) = 0.5A_0(1+\cos\frac{2\pi t}{T})$$

$$\alpha(t) = \alpha_0(1-\sin(\frac{2\pi t}{T}-\zeta)) \tag{2.30}$$

where $A(t)$ is the displacement of the wing center with amplitude A_0, $\alpha(t)$ is the angle of attack with amplitude $2\alpha_0$, T is the flapping period and ζ is the phase difference. The inclination angle of the stroke plane is β (Figure 2.13). In the present study, the parameters are: c = 1, e = 4, A_0 = 2.5, $\alpha_0 = \pi/4$, $T = 50\pi$, ζ = 0 and $\beta = \pi/3$. The characteristic length is c, the velocity scale is $\pi A_0/T$ and the Reynolds number is $\pi A_0 c/Tv$, which equals 157. This example has been previously studied by Xu and Wang (2006); the only difference is that the present characteristic velocity is 1/20 of theirs and thus the present time scale is 20 times of theirs.

The present rigid box ranges from -10 to 6 in both x-axis and y-axis, which is also the computational domain. The fine mesh system covers the area from 8 to 13 in x-axis and 8 to 14 in y-axis. The other area is covered with coarse mesh. The grid resolutions in fine block are $\Delta x_f = \Delta y_f = \Delta t_f$ = 1/64, and $\Delta x_c = \Delta y_c = \Delta t_c$ = 1/32 in coarse block. Further refinement of the mesh gives nearly the same results.

Figure 2.14 presents four images of the vorticity field near the wing within one period. A pair of vortex with different mode are created and shed from the leading and trailing edges of the wing. The vorticity results are very similar to Xu and Wang, and its physical meaning was given in detail by Wang (2000).

The temporal evolution of the drag and lift coefficients of the hovering wing is plotted in Figure 2.15(a, b), using the same time scale as Xu and Wang. Reasonable quantitative agreement is observed.

2.2.4 Deformation of a circular capsule in simple shear flow

The deformation of a circular capsule with elastic membrane is studied in simple shear flow, to validate the present numerical method for simulating the interaction between incompressible viscous fluids and elastic moving boundaries with constitutive laws. For a flexible capsule subjected to a shear flow, the non-slip boundary condition is satisfied by letting the flexible membrane move at the same velocity as the fluid around it. This motion will cause the capsule to deform. The boundary force is obtained from the constitutive law of the capsule membrane. According to Newton's second law when the capsule membrane is massless, the membrane force equals the opposite of the fluid force. The opposite of the membrane force is then distributed to the fluid mesh points near it by a smoothed version of the Dirac Delta function to account the effect of the boundary.

The capsule is initially unstressed, and filled with Newtonian liquid similar to that outside. The capsule's membrane follows Hooke's law, which in the form of:

$$\tau^H = E(\frac{\partial l(t)}{\partial l_0} - 1) \tag{2.31}$$

where E represents the interfacial elasticity modulus, the term $l(t)$ is the instantaneous arc distance along the membrane, and the term l_0 represents the initial arc distance along the unstressed membrane. Thus at any time t, the membrane tension τ^H is a function of arc distance around the membrane contour.

The dimension of the capsule is at the order of 10 μm, which results in very small Reynolds number. One dimensionless parameter, the dimensionless shear rate, is identified to play an essential role in determining the capsule deformation. The dimensionless shear rate G, which determines the relative importance of shearing and elasticity, in the form of:

$$G = \frac{\mu k a}{E} \tag{2.32}$$

where μ is the viscosity of the surrounding fluid, k is the shear rate of the flow at infinity and the term a is the radius of the capsule.

The deformation of the capsule is described by the Taylor shape parameter, which is defined as:

$$D_{xy} = \frac{L - B}{L + B} \tag{2.33}$$

where L and B are the length and width respectively of a capsule. They are computed by the approach of Breyiannis et al. (2000). It involves mapping a deformed capsule to an ellipse that shares the tensor of the moments of inertia, where L and B denote the axis lengths of the ellipse. The principal direction of this tensor is identified with the capsule inclination.

In the present study, all variables are normalized by the characteristic length $2a$, velocity $2ka$, time $1/k$, and tension μka. The Reynolds number based on above characteristic length and velocity is 0.05, which is in the range of normal physiological conditions. The membrane shear elasticity modulus varied so that different dimensionless shear rates, up to 0.4, are simulated. The computational domain ranges from 0 to $16a$ in both x-axis and y-axis. The capsule is at the center of the domain, and its membrane is equally discretized into 150 Lagrangian nodes. The fine mesh block covers from $5a$ to $11a$ in both axes. The other area is covered with coarse mesh. The grid resolutions in fine and coarse block are $\Delta x_f = \Delta y_f = 0.05a$ and $\Delta x_c = \Delta y_c = 0.1a$, respectively. The characteristic velocity is set to be 1×10^{-4}, so that the relaxation parameters in coarse block and fine block are 0.62 and 0.74, respectively.

From the present results, it is found that the capsule deforms to a steady shape and then membrane rotates around the liquid inside (tank-treading motion). Figure 2.16 presents the streamline pattern inside and outside the capsule at steady state, for G = 0.04. A single eddy inside the cell and recirculating external flows are observed.

The time evolution of the capsule deformation parameter D_{xy} and inclination angle θ (with respect to x-axis) are presented in Figures 2.17(a, b), and compared with previous results of Breyiannis and Pozrikidis (2000) by boundary element method. Good quantitative agreements are observed. It is seen the time taken to achieve steady shape is shorter if the dimensionless shear-rate is lower. A lower shear rate means the ratio between elastic and shear forces is larger (Equation 2.32), thus the capsule only needs to deform a little to generate enough elastic force to balance the

viscous shear-force. The result (Figure 2.17(a)) also shows that at bigger shear rate G, the deformation parameter D_{xy} at steady state is larger and the inclination angle (Figure 2.17(b)) is smaller. That is, the initially-circular capsule is more deformed and aligned with the flow as would be expected.

To demonstrate that the results are grid-independent, numerical simulation were carried out for G = 0.0125 and 0.125, with the same two-block system. The diameter of the circular capsule $2a$ was covered by 20, 40 or 60 lattice spaces of the fine mesh block. The temporal evolution of Taylor deformation parameter D_{xy} was used as an indicator for this study. From the result plotted in Figure 2.18, the grid resolution of $\Delta x_f = \Delta y_f = 0.05a$ is sufficient to capture the important characteristics. The effect of computational domain on capsules deformation was also studied under this grid resolution and the result is presented in Figure 2.19. It is shown that a square computational domain with side $16a$ is large enough to neglect the boundary effect.

2.3 Concluding remarks

A two-dimensional hybrid immersed-boundary and multi-block lattice Boltzmann method is presented to simulate moving boundaries interacting with incompressible viscous fluid. The present method preserves the advantages of the immersed-boundary method and lattice-Boltzmann method; and at the same time improves their accuracy and efficiency by employing a multi-block strategy.

The present method can accurately and efficiently simulate solid moving boundaries interacting with fluids; this is achieved by employing the direct forcing technique. Three benchmark computations were carried out to validate this capacity:

flow past a circular cylinder, two cylinders moving with respect to each other, and flow around a hovering wing.

The deformation of a circular liquid-filled capsule with elastic membrane in simple shear flow was also studied. The present results agree very well with previously published results, and show the present method reliable for simulating the interaction between incompressible viscous fluids and elastic moving boundaries with constitutive laws.

	Re = 100			Re = 200		
	C_d	C_l	St	C_d	C_l	St
Lai and Peskin (2000)	1.4473	0.3299	0.165	-	-	0.190
Russel and Wang (2003)	1.43	0.339	0.175	1.45	0.75	0.202
Xu and Wang (2006)	1.423	0.34	0.171	1.42	0.66	0.202
Chew and Shu (2002)	1.3668	0.375	0.164	-	-	-
Present	1.438	0.344	0.166	1.449	0.709	0.197

Table 2.1 Comparison with previous studies on flow past a circular cylinder

Grid resolution in fine block	Re = 100	Re = 200
1/30	1.454	1.459
1/40	1.443	1.451
1/50	1.438	1.449
1/60	1.436	1.448
1/70	1.435	1.448

Table 2.2 Drag coefficients for different grid size

	C_d	C_l	St
Cylinder without filament	1.438	0.344	0.166
Cylinder with filament	1.406	0.396	0.156

Table 2.3 Comparison of flow characteristics for flow past a circular cylinder with and without a downstream filament

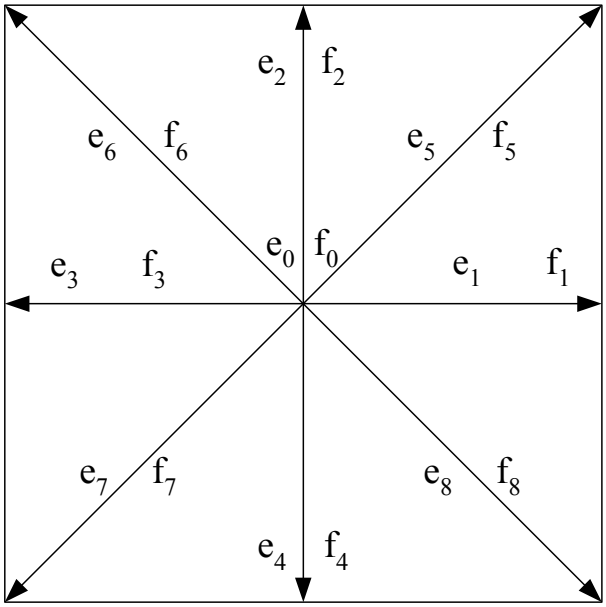

Figure 2.1 D2Q9 lattice model

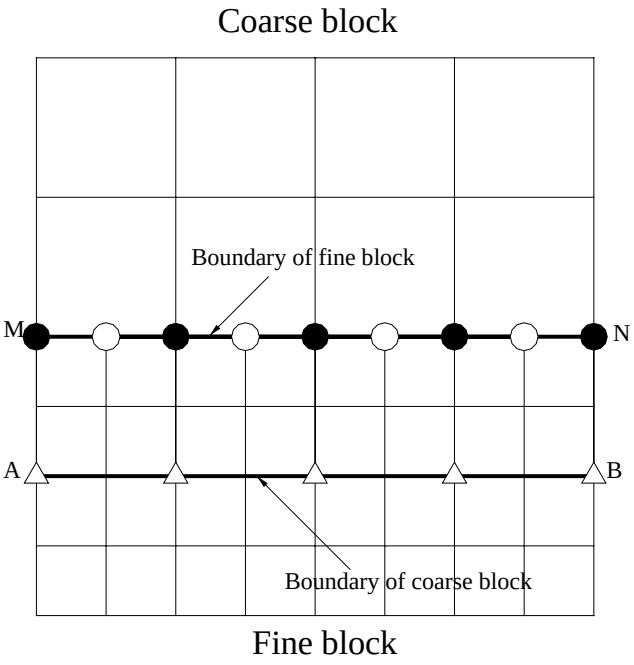

Figure 2.2 Interface structures between two blocks

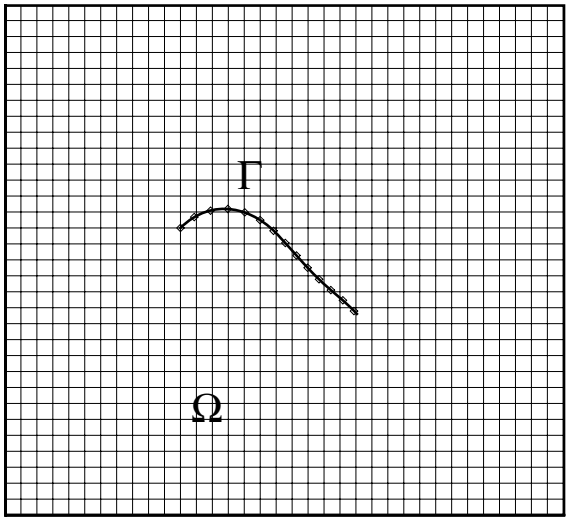

Figure 2.3 An elastic boundary immersed in a fluid

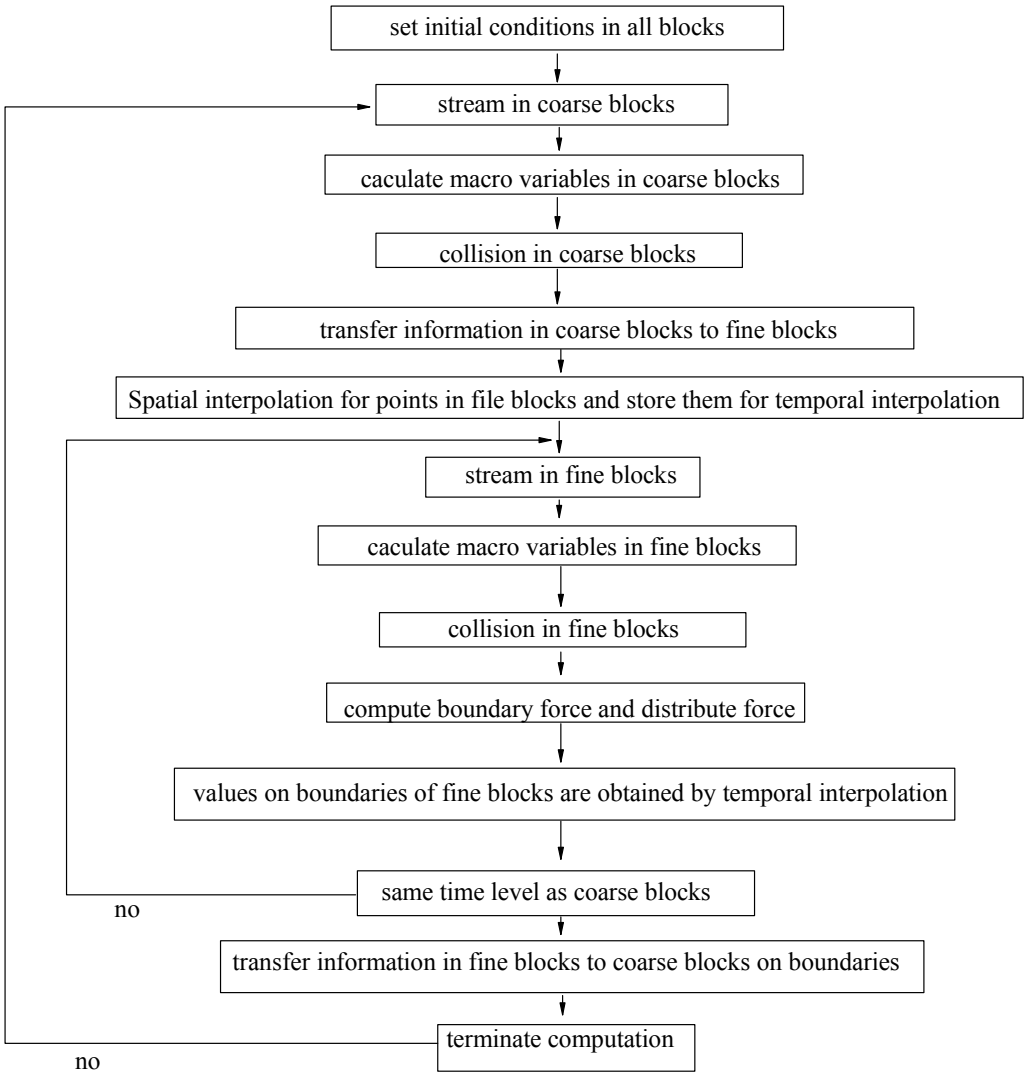

Figure 2.4 General computational procedure

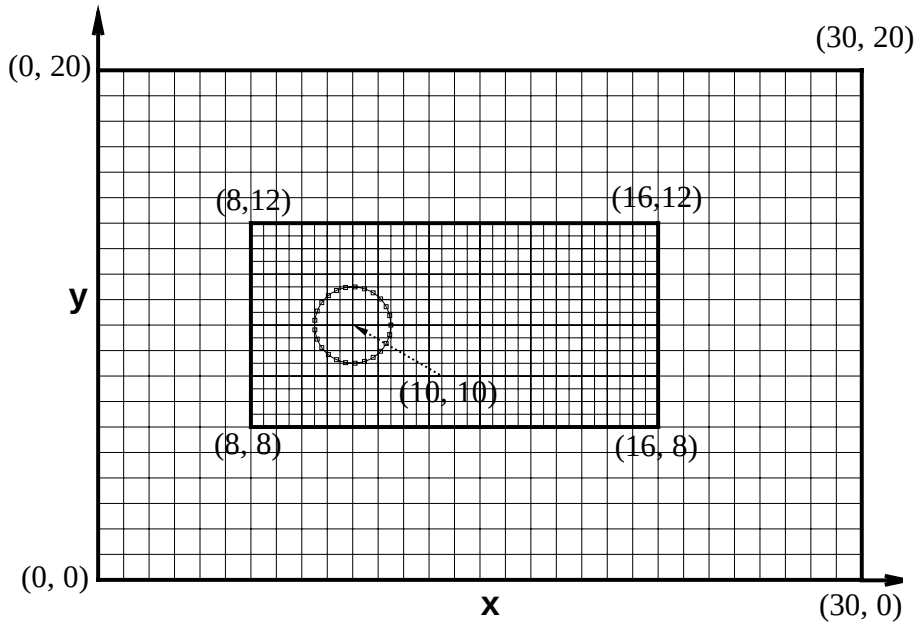

Figure 2.5 Illustration of mesh and block system on the computational domain of flow past a circular cylinder. The block area is adjusted and the mesh density is reduced by a factor of 25 for clarity

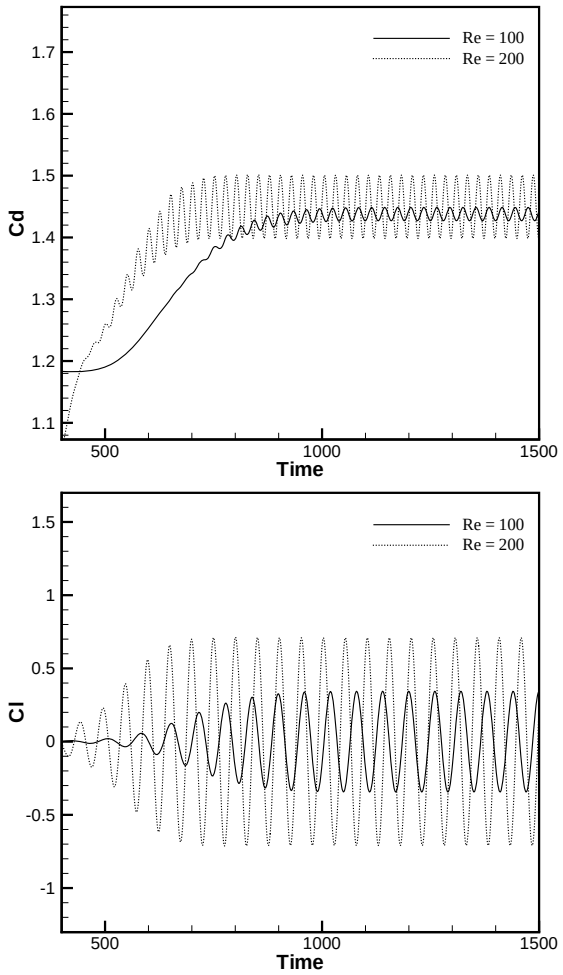

(a) (b)

Figure 2.6 Evolution of force coefficients for flow past a circular cylinder at Re = 100 and 200: (a) drag, (b) lift

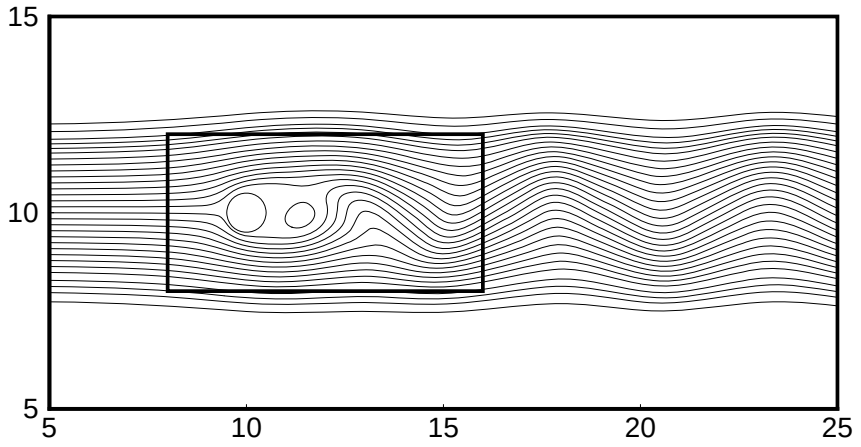

(a)

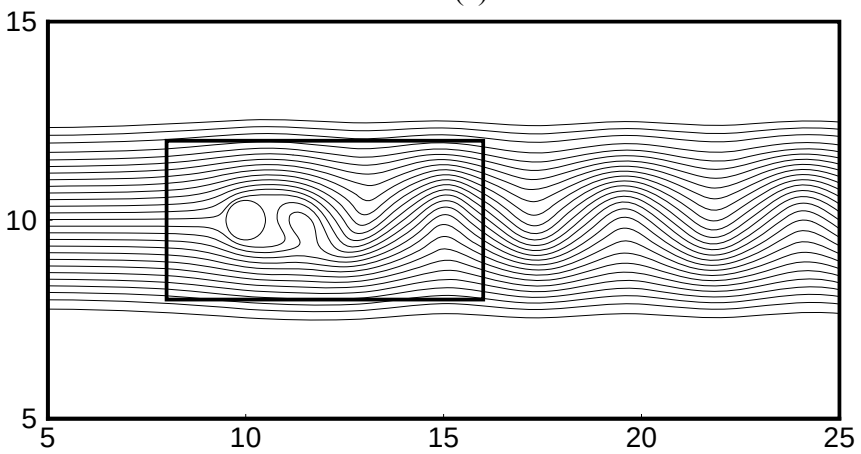

(b)

Figure 2.7 Stream function contour for flow past a circular cylinder at: (a) Re = 100, (b) Re = 200

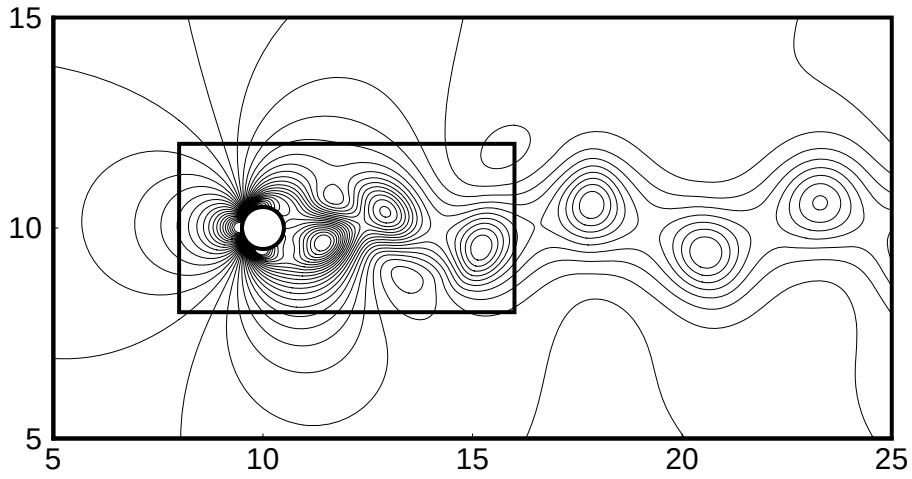

(a)

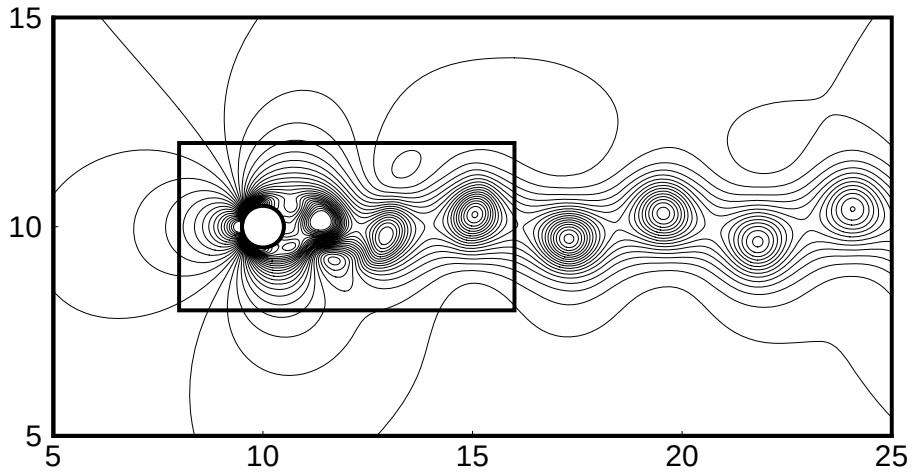

(b)

Figure 2.8 Pressure contours for flow past a circular cylinder at: (a) Re = 100, (b) Re = 200

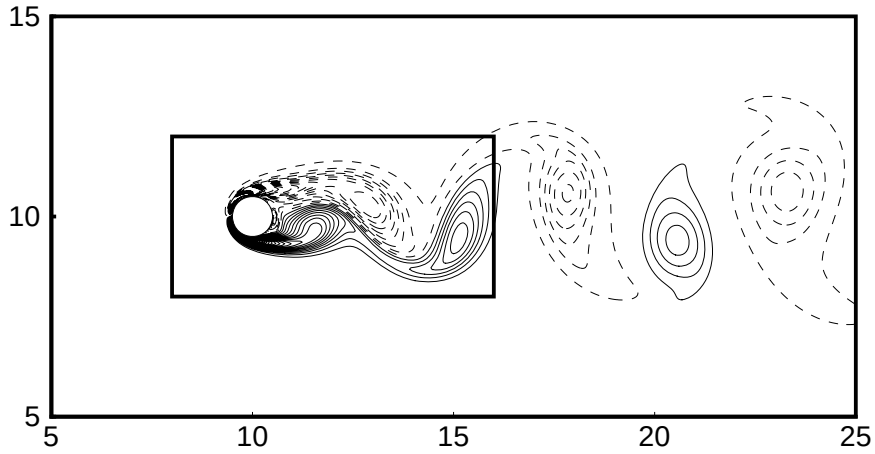

(a)

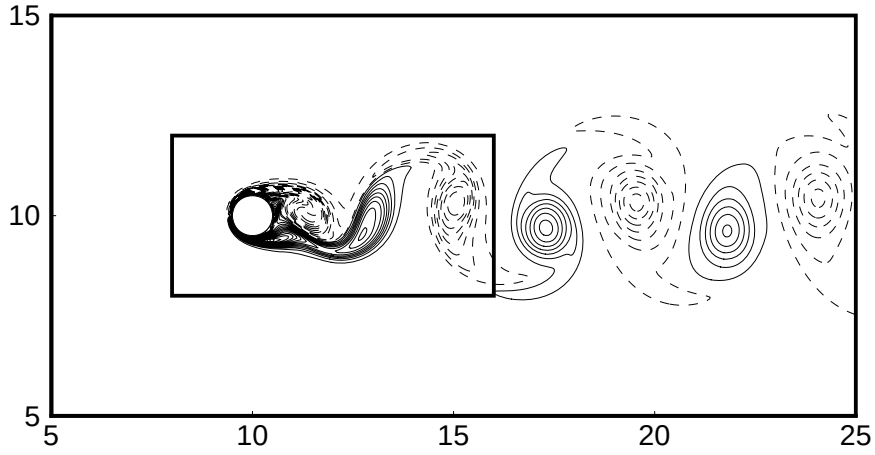

(b)

Figure 2.9 Vorticity contours for flow past a circular cylinder at: (a) Re = 100, (b) Re = 200

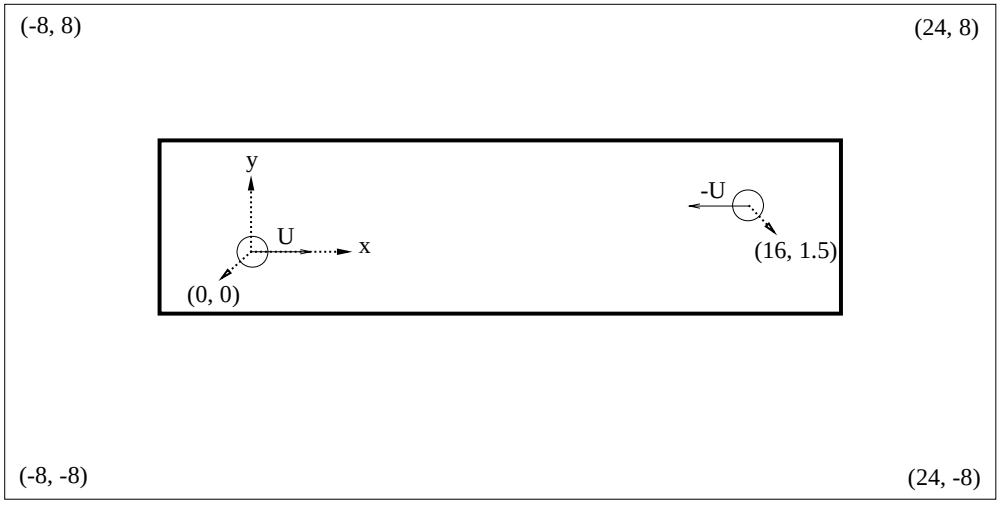

Figure 2.10 Computational geometry for two cylinders moving respect to each other

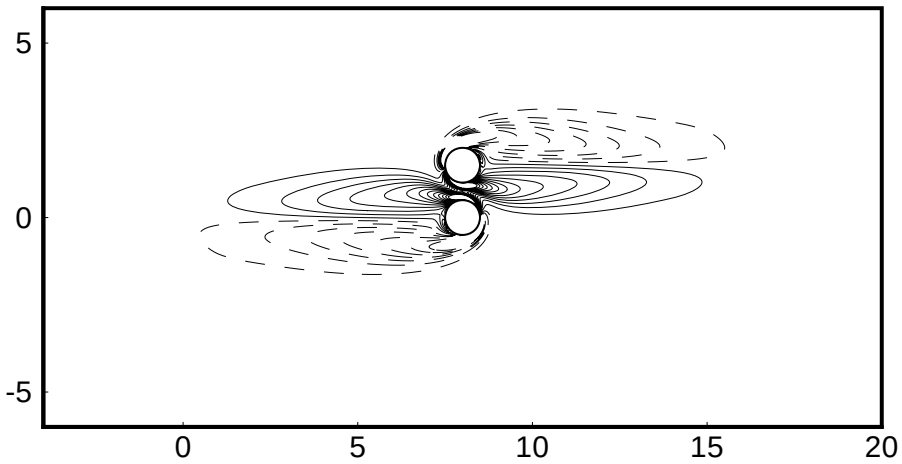

(a)

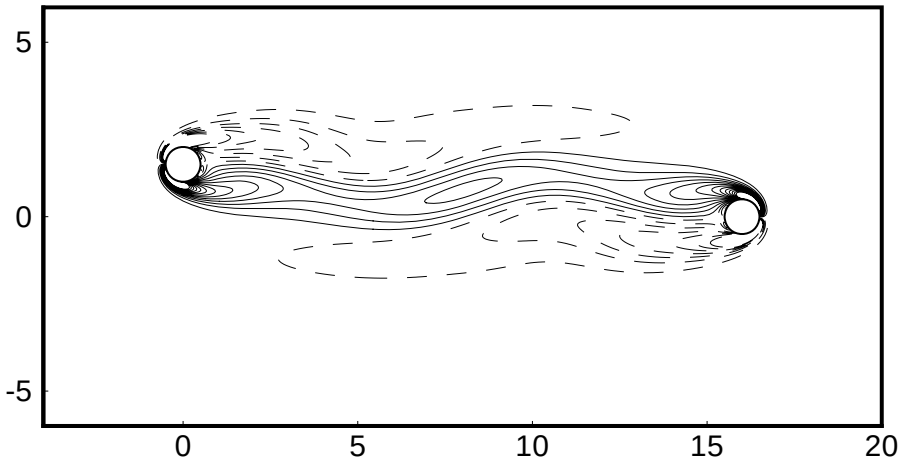

(b)

Figure 2.11 Vorticity fields around two cylinder moving with respect to each other; (a) cylinders are closest to each other; (b) cylinders are separated by a distance of 16

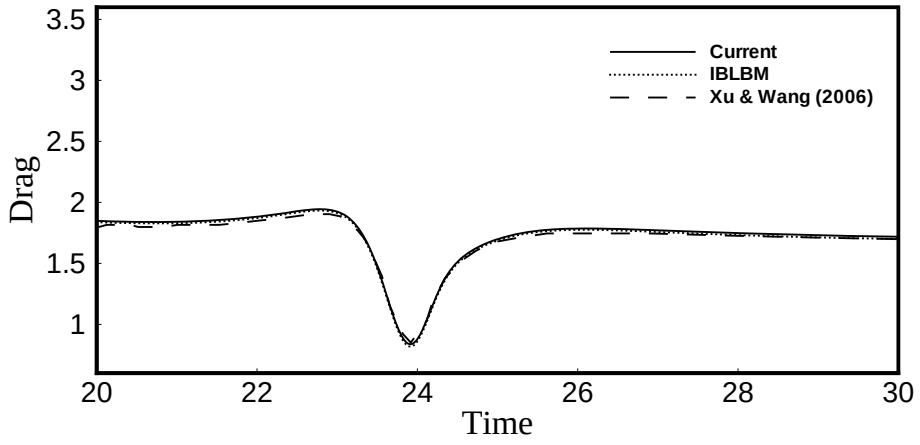

(a)

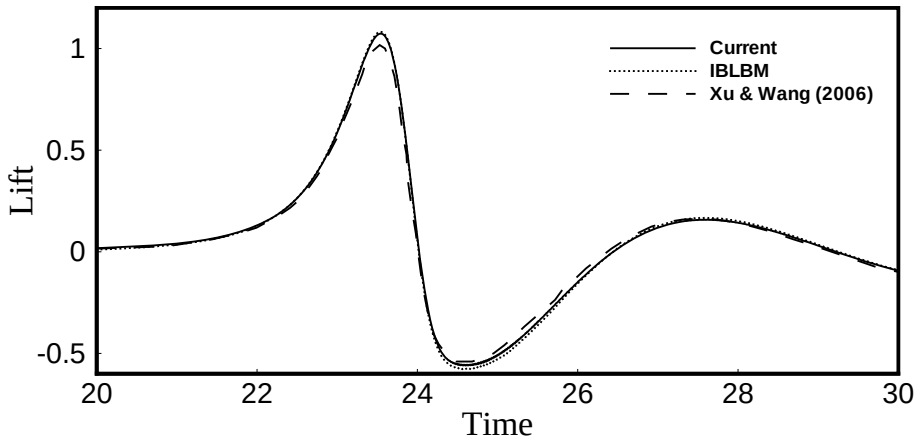

(b)

Figure 2.12 Temporal evolution of (a) Lift and (b) Drag coefficients for the upper cylinder in flow around two cylinder moving respect to each other

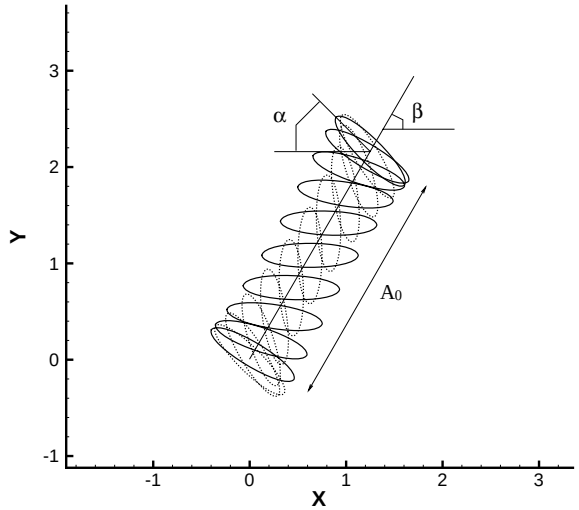

Figure 2.13 Positions of a hovering wing in one period. The solid ellipses represent the downstroke phase and the dotted ellipses represent the upstroke phase

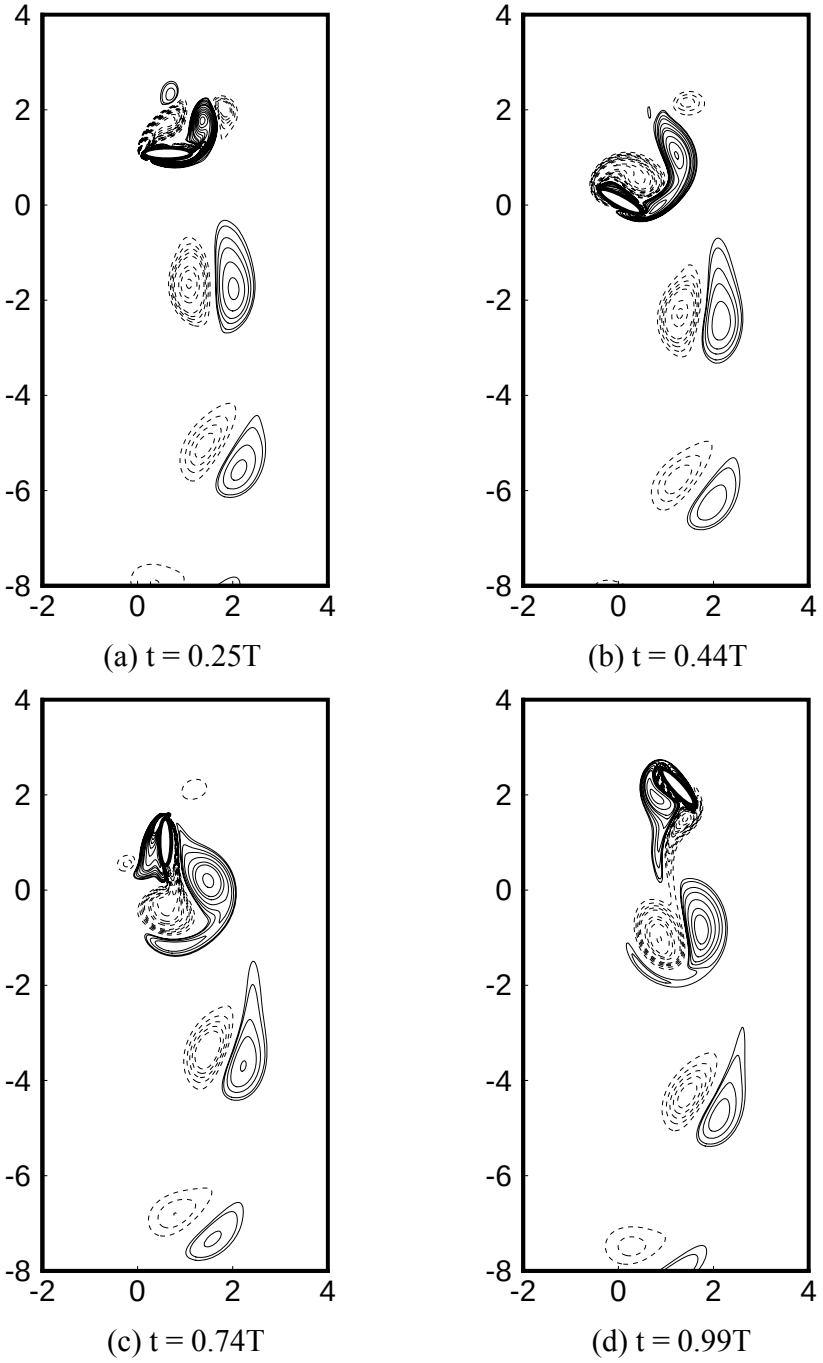

(a) t = 0.25T (b) t = 0.44T

(c) t = 0.74T (d) t = 0.99T

Figure 2.14 Vorticity fields around a hovering wing at four different instants in a period

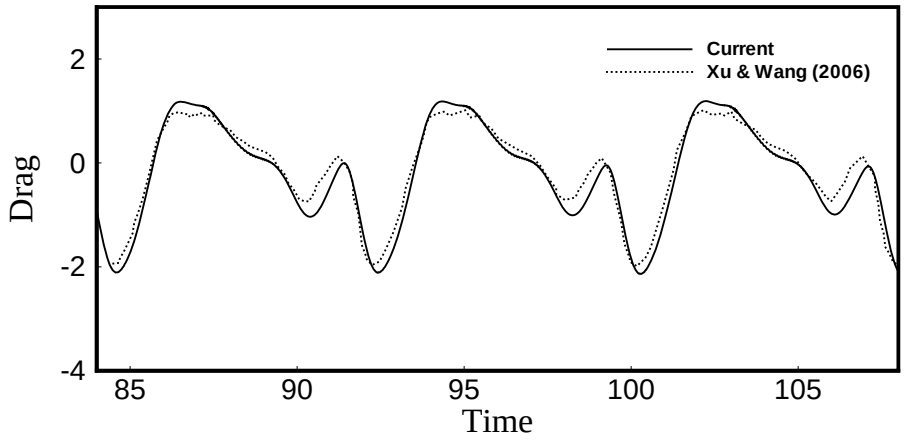

(a)

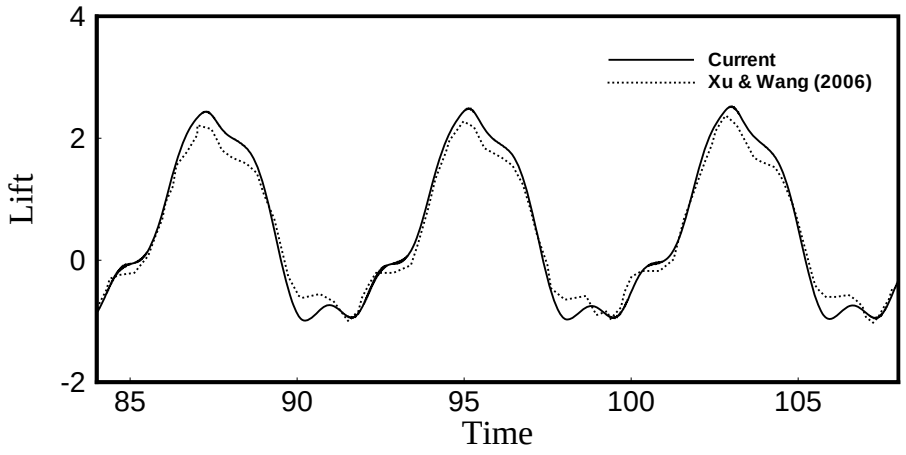

(b)

Figure 2.15 Temporal evolution of (a) Drag and (b) Lift coefficients for flow around a hovering wing at Re = 157

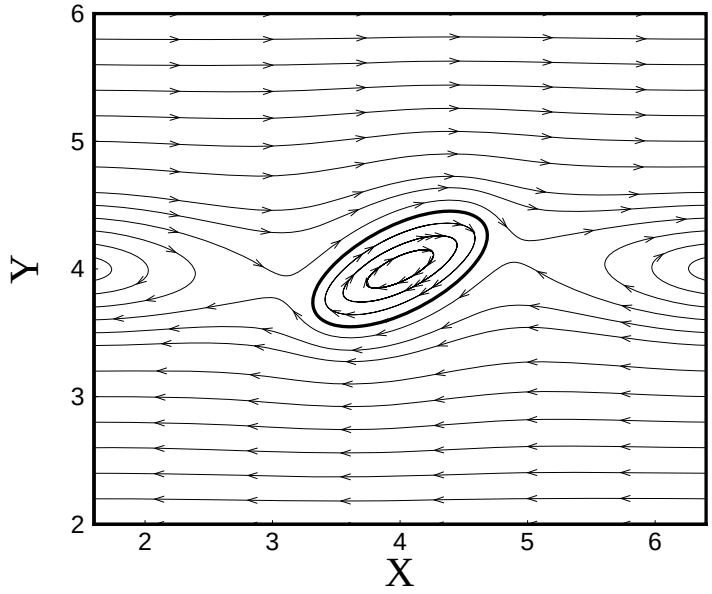

Figure 2.16 The streamline pattern inside and outside the capsule at steady state for G = 0.04

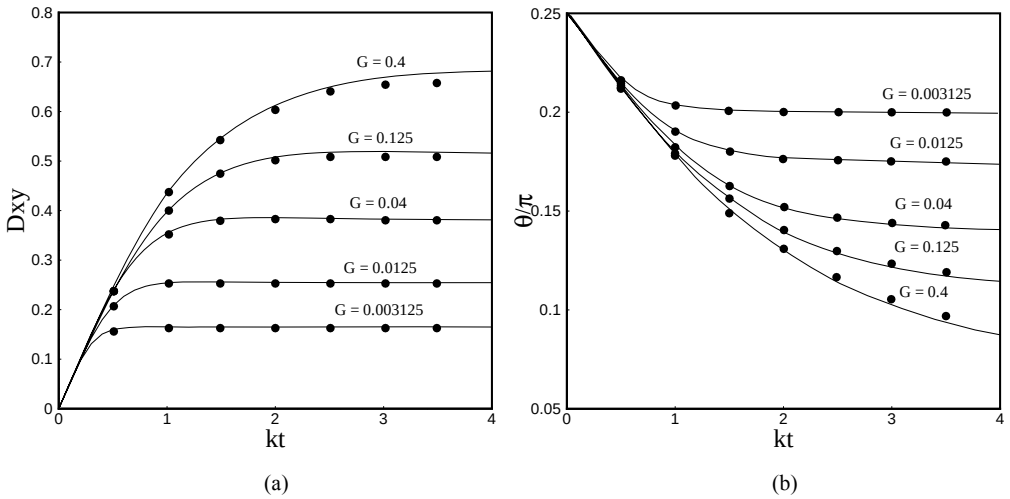

(a) (b)

Figure 2.17 Temporal evolution of : (a) Taylor deformation parameter; (b) orientation angle. _____, present method; ●, boundary element method (Breyiannis and Pozrikidis, 2000).

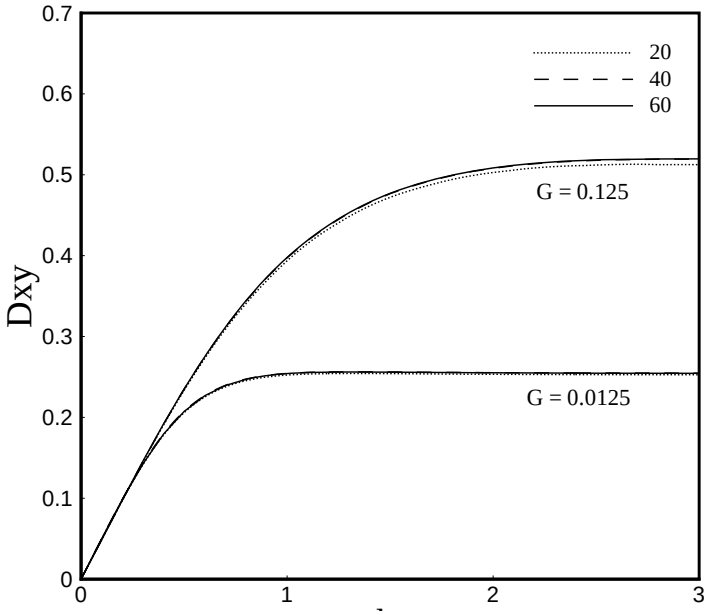

Figure 2.18 Temporal evolution of Taylor deformation parameter for different grid resolutions

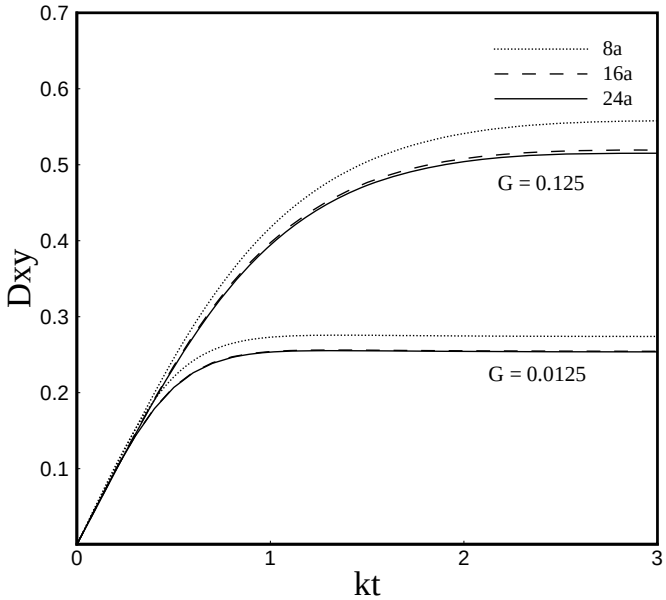

Figure 2.19 Temporal evolution of Taylor deformation parameter for different size of computational domains

Chapter 3 Effect of Membrane Bending Stiffness on the Deformation of Two-dimensional Capsules in Shear Flow*

For liquid filled capsules enclosed by elastic membrane, flow induced deformation causes the development of not only in-plane elastic tensions, but also bending moments accompanied by transverse shear tensions. The bending stiffness has been found quite important in determining the equilibrium configuration and shape oscillations of capsules, as well as in avoiding the development of wrinkling and folding of capsules under flow. A numerical study of Pozrikidis (2001) showed that bending stiffness has significant effect on the steady configuration of elastic capsules in simple shear flow. However, an important restriction was the requirement that the minimum bending-energy shape has uniform curvature. So far, there is no study on the transient deformation of elastic capsules whose minimum bending-energy configuration has non-uniform curvature.

In this chapter, the transient deformation of two-dimensional elastic capsules, filled with a Newtonian liquid similar to that outside, is studied numerically under simple shear flow condition. The purpose of the present study is to investigate the effect of membrane bending stiffness on the deformation of such capsules. The deformation of capsules with initially circular, elliptical and biconcave resting shapes was studied;

* The results of this chapter have been published as "Sui, Y., Chew, Y. T., Roy, P., Chen. X. B. and Low H. T., Transient deformation of elastic capsules in shear flow: effect of membrane bending stiffness, Phys. Rev. E, 75: 066301, 2007."

the capsules' minimum bending-energy configurations were considered as either uniform-curvature shapes (like circle or flat plate) or their initially resting shapes.

The present study is based on the hybrid method proposed in Chapter 2. In this approach the flow field is solved by the lattice Boltzmann method, the fluid-capsule interaction is solved by the immersed boundary method, and the multi-block strategy is used to refine the mesh around the deforming capsule. The present model has been validated in Chapter 2, in which the bending stiffness is not considered.

One must acknowledge that the two-dimensional model is a large simplification; however, previous studies (Zhou and Pozrikidis, 1995; Biben and Misbah, 2003; Beaucourt et al., 2004) have provide sufficient grounds which show that two-dimensional study maintains most common features of the two-dimensional capsule motion, for example the transition from tank treading mode to tumbling mode.

3.1 Numerical model

3.1.1. Membrane mechanics

In the present study, the deformation of a two-dimensional capsule is considered to be subjected to the two dimensional incident shear flow along the x-axis, $\mathbf{u} = (ky, 0)$, as illustrated in Figure 3.1. The unit tangent vector $\mathbf{t}$ is pointing in the direction of increasing arc length and $\mathbf{n}$ is the unit normal vector pointing into the ambient fluid.

During the capsule deformation, the velocity across the interface is continuous in order to satisfy the non-slip condition. But there is a jump of the interfacial tension $\Delta\mathbf{F}$, which is in the form of (Pozrikidis, 2003a):

$$\Delta \mathbf{F} = \Delta F^n \mathbf{n} + \Delta F^t \mathbf{t} = -\frac{d\mathbf{T}}{dl} = -\frac{d}{dl}(\tau \mathbf{t} + q\mathbf{n}) \tag{3.1}$$

where $\mathbf{T}$ is the membrane tension, consisting of the in-plane tension τ and transverse shear tension q. Expanding out the derivatives of the products on the left-hand side of Equation (3.1), and using the relations

$$\frac{d\mathbf{t}}{dl} = -\tau \mathbf{n} \tag{3.2}$$

$$\frac{d\mathbf{n}}{dl} = \tau \mathbf{t} \tag{3.3}$$

where κ is the curvature of the membrane curvature, the normal and tangential loads in Equation (3.1) are in the form of:

$$F^n = \kappa\tau - \frac{dq}{dl} \tag{3.4}$$

$$F^t = -\frac{d\tau}{dl} - \kappa q \tag{3.5}$$

The in-plane tension τ is obtained from the membrane's constitutive law. In the present study, Hooke's law is employed due to its simplicity; however it is sufficient to take deformability into account. It has the form:

$$\tau = E(\frac{\partial l(t)}{\partial l_0} - 1) \tag{3.6}$$

where E represents the interfacial elasticity modulus, the term $l(t)$ is the instantaneous arc distance along the membrane, and the term l_0 represents the initial arc distance along the unstressed membrane. Thus at any time t, the membrane tension τ^H is a function of arc distance around the membrane contour. The Hooke's law is only valid for small deformation. However, the Hooke's law has been employed in previous studies on flow induced deformation of capsules (Breyiannis and Pozrikidis, 2000).

For large capsule deformation, it will describe the relation of membrane strain and stress in an exaggerated or understated way (Breyiannis and Pozrikidis, 2000).

The transverse shear tension q, is expressed in terms of bending moment m:

$$q = \frac{dm}{dl} \tag{3.7}$$

The bending moment is given by:

$$m = E_B(\kappa(l) - \kappa_0(l)) \tag{3.8}$$

where E_B is the bending modulus, $\kappa(l)$ is the instantaneous membrane curvature and $\kappa_0(l)$ is the curvature of membrane at minimum bending-energy configuration (Steigmann et al., 1997).

In the present simulation, there is no special constraint for the volume of the capsule. The results show that the volume change during capsule deformation is less then 0.1%.

Due to the small length scale (10^{-6} – 10^{-5} m) of the capsule and the small surrounding fluid velocity (10^{-3} – 10^{-2} m/s), the inertia effect is neglected. Two dimensionless parameters are identified to play an essential role in determining the capsule deformation. One is the dimensionless shear rate G, which determines the relative importance of shearing and elasticity, in the form of:

$$G = \frac{\mu k a}{E} \tag{3.9}$$

where μ is the viscosity of the surrounding fluid, k is the shear rate and the term a is the equivalent radius, in the form of $a = (capsule\ area/\pi)^{0.5}$. Another important parameter is the reduced ratio of bending to elasticity moduli, in the form of:

$$E_b = \frac{E_B}{a^2 E} \tag{3.10}$$

3.1.2. Numerical method

The present study is based on the hybrid method proposed in Chapter 2. The computational domain ranged from 0 to $16a$ in both x-axis and y-axis. Numerical experiment showed that the size of this computational domain is large enough to neglect the boundary effect. The capsule was at the center of the domain, and its membrane was equally discretized into 160 Lagrangian nodes. The fine mesh block covered from $5a$ to $11a$ in both axes. The other area was covered with coarse mesh. The grid resolutions in fine and coarse block were $\Delta x_f = \Delta y_f = 0.05a$ and $\Delta x_f = \Delta y_f = 0.1a$, respectively. Grid-independent study showed that this mesh density was sufficient.

3.2 Results and discussion

3.2.1 Initially circular capsules

The deformation of capsules with initially circular shape in simple shear flow is studied. The initial shape is also the resting shape concerning the in-plane tension. The results presented in this section corresponds to capsules whose initial shape is also the minimum bending-energy profile. Capsules with flat minimum bending-energy shape are found to behave in a similar way.

In the present study, all variables are normalized by the characteristic length $2a$, velocity $2ka$, and time $1/k$. The Reynolds number based on the above characteristic

length and velocity was 0.05. The membrane shear elasticity modulus was varied so that different dimensionless shear rates were obtained and studied. The characteristic velocity was set to be 1×10^{-4}, so that the relaxation parameters in coarse block and fine block were 0.62 and 0.74, respectively.

The present results show that the capsules deform to steady shapes and then the membrane rotate around the liquid inside (tank-treading motion). Figure 3.2(a) presents a family of configurations of steady deformed capsules for reduced bending modulus $E_b = 0 \sim 0.4$ at the dimensionless shear rate $G = 0.04$. As expected, the effect of bending stiffness is apparent. It restricts the global deformation of capsules, and locally prevents the development of highly curved shapes at the two tips. With the increase of the bending modulus, the shapes of the steady deformed capsules become closer to a circle and the orientations become less aligned with the flow direction. If the shear rate is higher, as shown in Figure 3.2(b) for $G = 0.125$, it is seen that the capsules are more deformed for the same reduced bending modulus.

To quantitatively illustrate the effect of bending stiffness on the capsules deformation, the temporal evolution of the Taylor deformation parameter and inclination angle (with respect to x-axis) are presented in Figure 3.3, for $G = 0.04$ and 0.125. The quantitative results confirm that increased bending stiffness reduces the capsule deformation and makes it less aligned with the flow. It is also seen that the time taken to achieve steady shape is shorter under lower dimensionless shear rate or higher reduced bending modulus. That is because the capsule only needs to deform a little to generate enough elastic force to balance the viscous shear force.

After the capsule deforms to a steady configuration, its membrane rotates around the liquid inside with period T. The normalized tank treading frequency, $f = 4\pi/(kT)$, is presented in Figure 3.4 for various bending modulus at $G = 0.04$ and 0.125. It is seen that, with increasing bending modulus, the dimensionless frequency asymptotically approaches towards the value of unity, corresponding to that of a solid circular cylinder in simple shear flow.

3.2.2 Initially elliptical capsules

In this section, the deformation of initially elliptical capsules, with a semi-major to semi-minor axes ratio of 2:1 and equivalent radius a, is simulated. The capsules are initially unstressed concerning the in-plane tension. Various resting configurations concerning the bending moments are considered: uniform curvature shapes (circle and flat plate) and non-uniform curvature shape (the initially elliptical configuration). The computational domain, block system, mesh resolutions and characteristic scales are the same as that in the previous section.

First considered are capsules with the minimum bending-energy shape having uniform curvature shape which is circular. The area of the circle is the same as that of the initially elliptical capsule. Figure 3.5(a, b) presents the configurations of steady deformed capsules with the reduced bending modulus increasing up to 0.2, at the dimensionless shear rate $G = 0.04$ and 0.125, respectively. The overall deformation of the capsules is quite similar to that of the initially circular capsules. As the bending modulus increases, the steady configurations of capsules tend to become circular. Figure 3.6(a, b) presents the steady Taylor deformation parameters and inclination

angles of capsules with different bending modulus ratios. It is shown from the results that as E_b increases, the Taylor deformation parameter decreases while the inclination angle increases monotonically. The minimum bending-energy shape having uniform curvature, which is flat, has also been studied. It was found that they behave in a similar way.

For a capsule membrane with a certain structure, composing for example of polymeric or proteinic networks, the membrane may prefer a certain resting configuration concerning the bending moments, due to the membrane structure. This preferred minimum bending-energy configuration may have non-uniform curvature. However, the transient deformation of elastic capsules with minimum bending-energy configuration having non-uniform curvature has not been studied so far. In this Section, the capsules' initially elliptical shape is chosen as the minimum bending-energy configuration. The present membrane model is able to describe the in-plane elasticity and bending moments, but it does not represent the polymerized structures of the membrane.

Without bending stiffness, a capsule deforms to a stationary shape with a finite inclination angle; then the membrane rotates around the liquid inside, as presented in Figure 3.7(a). When there is bending stiffness, it will try to keep the instantaneous curvature of the capsule akin to its initial curvature.

From the present results, it is interesting to find that with a finite but small bending modulus, the membrane still carries out tank treading motion. However, two protrusions develop on the membrane and rotate around the liquid inside, as presented in Figure 3.7(b, c) for $E_b = 0.005$ and 0.02, respectively. The animation of the capsule

contours shows that the capsule inclination is undergoing periodic oscillation while the membrane with protrusions rotates. These observations are different from that of a capsule without bending stiffness or with a minimum bending-energy shape of uniform-curvature. As the bending modulus increases, the protrusions become larger (see Figure 3.7), and so does the oscillation amplitude of the capsule's inclination angle.

When the reduced bending modulus reached 0.06, the motion of the capsule has changed from tank treading mode to tumbling mode accompanied with periodic deformation. Figure 3.8 presents a series of capsule contours for $E_b = 0.06$ and $G = 0.04$, at the dimensionless time kt = 0, 1.6, 6.4 and 8. The symbol ● represents the same Lagrangian node on the membrane. From the results, it is seen that the capsule is undergoing tumbling motion. It is elongated or compressed by the shear flow periodically.

With further increase in bending stiffness the tumbling motion continues, but the capsule is hardly deformed and behaves like a rigid body. Figure 3.9 presents the capsule contour for $E_b = 0.4$ and $G = 0.04$ at kt = 0, 2 and 6.4. It is seen that the capsule tumbles without visible shape changes.

Figure 3.10 presents the temporal evolution of the capsule inclination angle for various bending modulus at $G = 0.04$. It is seen that without bending stiffness ($E_b = 0$), a steady tank treading mode is achieved; with a finite but small bending stiffness ($E_b = 0.005$, 0.02 and 0.04), the capsule's orientation undergoes oscillation with amplitude increasing as the bending modulus increases. Further increasing the bending rigidity ($E_b = 0.06$ and 0.4) causes the mode transition, that is the oscillation

amplitude is larger than π. Figure 3.10 shows that the transition happens between $E_b = 0.04$ and 0.06. For a rigid ellipse rotating in two dimensional shear flow at vanishing Reynold number, its orbit can be predicted by Jeffery's theory (Jeffery, 1922). The angular rotation is given by:

$$\theta = \tan^{-1}(r \tan \frac{rkt}{1+r^2}) \tag{3.11}$$

where r is the aspect ratio, which equals 2 in the present study. Jeffery's solution is plotted in Figure 3.10. For $E_b = 0.06$, the capsule is undergoing tumbling motion. However due to its deformability, the result departs largely from Jeffery's theory. For $E_b = 0.4$ when the deformation of the capsule is small, reasonable quantitative agreement is observed, which confirms that the capsule tumbles like a rigid body.

Simulation for capsules with various bending modulus for dimensionless shear rate $G = 0.125$ has also been carried out. It was found that the behavior of the capsules is similar to that for $G = 0.04$. However, the critical bending modulus for modes transition is higher.

Through the above observations, it is found that with the bending stiffness increasing, the motion of a capsule can be divided into four sequential stages: 1) steady tank treading mode (at zero bending stiffness); 2) tank treading with orientation oscillation and shape deformation (at finite but small bending stiffness); 3) tumbling with periodic shape deformation (at moderate bending stiffness); 4) tumbling like a rigid body (at large bending stiffness). The motion of the capsule at stage 2 seems similar to the "vacillating-breathing" mode, which is theoretically predicted by Misbah (2006).

Without bending stiffness, the shear elasticity of the capsule membrane can only resist membrane in-plane stretching. Thus the shear torque can be easily transferred to the membrane, which will lead to steady tank treading motion. However, transition to tumbling may be triggered for cases where: a) the viscosity contrast is large enough; b) the membrane viscosity is increased. In both cases due to the fact that the viscosity increases, the transfer of shear torque to the membrane becomes more and more difficult; and then the capsule would behave like a solid body which undergoes tumbling.

In this section, the elliptical capsule's initial shape is the minimum bending-energy shape. Due to the bending stiffness, the membrane's instantaneous curvature $\kappa(l)$ must keep akin to $\kappa_0(l)$, the curvature of the elliptical shape. This will restrict the deformability of the capsule. In shear flow, with the bending stiffness increasing, it becomes more and more difficult for the capsule to deform. Thus it becomes more difficult for the shear torque to be transferred to the membrane; and then the capsule will undergo tumbling motion. With a large bending stiffness, the capsule is hardly able to deform and thus tumbles like a rigid body.

With the initial shape considered as the minimum bending energy shape, the deformation of initially elliptical capsules with $E_b = 0.01$ is studied under various dimensionless shear rates. Figure 3.11 presents snapshots of capsules' profiles during the deformation. Figure 3.12 presents the temporal evolution of the capsule inclination angle for various dimensionless shear rates at $E_b = 0.01$. It is interesting to find that decreasing the shear rates will also result in a transition of the capsule's motion mode, from tank treading to tumbling. That is because when the shear rate

decreases, the relative importance of membrane bending rigidity and shear elasticity will increase, which makes the capsule relatively solidified.

3.2.3 Initially biconcave capsules

The biconcave capsule has an initial shape (Pozrikidis, 2003b) given by:

$$x = a\alpha \sin\chi$$

$$y = a\frac{\alpha}{2}(0.207 + 2.003\sin^2\chi - 1.123\sin^4\chi)\cos\chi \tag{3.12}$$

where α is the cell radius ratio which equals 1.39 for a red blood cell, and the parameter χ ranges from -0.5π to 1.5π. This shape is the cross section of a three dimensional red blood cell with equivalent radius a. Its two dimensional equivalent radius is $0.74a$. The capsules are initially unstressed concerning the in-plane tension. Various minimum bending-energy configurations, including uniform curvature shapes (circle and flat plate) and non-uniform curvature shape (the initially bi-concave configuration), are studied. The computational domain, block system, and mesh resolutions are the same as that in previous sections. The characteristic length is the equivalent diameter of the biconcave capsule, which equals $1.48a$. The characteristic velocity is $1.48ka$, and the Reynolds number is at 0.027.

The deformation of capsules with circular minimum bending-energy shape is first considered. The area of the circle is the same as that of the biconcave capsule. Figure 3.13 presents the configurations of steady deformed capsules with the reduced bending modulus increasing up to 0.1, at the dimensionless shear rate $G = 0.025$. The rounding effect is apparent. As the bending modulus increases, the circularity of the

steady deformed capsules increases. Capsules with flat resting shape concerning the bending moments have also been studied. Similar phenomenon was observed.

Also studied is the deformation of capsules with the initially biconcave shape as the minimum bending-energy configuration. Figure 3.14 presents the capsule profiles at different time for $E_b = 0.015$ and $G = 0.025$. From the results it is seen that the capsule still carries out motion of the tank treading mode. Protrusions develop along the membrane and rotate around the internal liquid. The animation of the capsule configurations shows that the capsule inclination is undergoing periodic oscillation while the membrane rotates. The oscillation amplitude increases with the bending modulus increasing and finally the motion changes to tumbling mode.

Figure 3.15 presents a family of capsule contours for $E_b = 0.02$, at the dimensionless time kt = 0, 1.26, 7.38, 14.22 and 15.66. The results show that the capsule is tumbling continuously. The animation of the capsule contours shows that the tumbling motion is accompanied by periodic deformation. The capsule is elongated (illustrated in Figure 3.15b) or compressed (illustrated in Figure 3.15d) by the shear flow. Further increasing the bending stiffness makes the capsule carry out rigid-body like tumbling motion, which resembles Jeffery's mode, as illustrated in Figure 3.16 for $E_b = 0.2$.

Figure 3.17(a) presents the temporal evolution of the capsule inclination angle for various bending modulus at $G = 0.025$. It is seen that for low bending modulus, the inclination is undergoing small oscillations. The oscillation amplitude increases as the bending modulus increases, and finally causes the change from tank treading to tumbling modes. The result shows that this transition happens between $E_b = 0.015$

and 0.02. During the tumbling motion, the capsule rotates faster when perpendicular to the flow and slower when aligned with the flow direction. For $E_b = 0.2$ in which the deformation of the capsule is small, the orbit of the capsule is compared with Jeffery's theory. In Equation (3.7), the aspect ratio is determined following the approach of Goldsmith and Marlow (1972), as well as Ramanujan and Pozrikids (1998). That is, it is chosen so that the numerical tumbling period matches that predicted by theory. Satisfactory quantitative agreement is observed in Figure 3.17(a).

It has been shown in previous studies (Zhou and Pozrikidis, 1995; Sui et al., 2007) that a two-dimensional biconcave capsule achieves a steady tank-treading mode without bending stiffness. In the present section, a four-stage motion, similar to that in Section 3.2.2, is found for a biconcave capsule with various bending stiffness. The physical mechanism should also be the same.

It is well known that red blood cell membrane is strongly resistant to area dilatation. The membrane model employed here does allow area dilatation. However, the present methodology allows incorporation of incompressible membrane models. With the Hooke's law used in the present study, by increasing the membrane stiffness, a case with membrane incompressibility can be approximated. This case was studied with $G = 0.0025$ under various bending stiffness. The maximum membrane area change was within 0.5%. The temporal evolution of the capsule inclination angle is presented in Figure 3.17(b). The capsule motion is closely similar to that for $G = 0.025$ and so is the transition to tumbling mode. However, the critical bending modulus for motion transition is lower.

With the initial shape considered as the minimum bending energy shape, the deformation of initially elliptical capsules with $E_b = 0.01$ is studied under various shear rates. Figure 3.18 presents snapshots of capsules' profiles during the deformation under dimensionless shear rate $G = 0.04$, 0.02, 0.01 and 0.001. Figure 3.19 presents the temporal evolution of the capsule inclination angle under these dimensionless shear rates. Similar to the deformation of elliptical capsules, unsteady tank treading motion is observed for $G = 0.04$ and 0.02. The tank-treading-to-tumbling transition is between $G = 0.02$ and 0.01. For very small shear rate, the capsule carry out rigid-body like tumbling motion, as illustrated in Figure 3.18 (d). For $G = 0.001$ the deformation of the capsule is small, the capsule' orbit is compared with Jeffery's theory.

3.3 Concluding remarks

The effect of interfacial bending stiffness on the deformation of liquid capsules enclosed by elastic membranes in shear flow has been studied numerically, using an improved immersed boundary-lattice Boltzmann method. Initially circular, elliptical and biconcave capsules with various minimum bending-energy shapes, including circular, flat plate, or their initially resting shapes have been studied. The results show that for capsules with minimum bending-energy configurations having uniform curvature (circular, flat plate), the steady deformed shapes are more rounded with increasing bending stiffness. For initially elliptical and biconcave capsules with their initial configurations as the minimum bending-energy shapes, it is interesting to find that with the bending stiffness increasing or the shear rate decreasing, the capsules'

behavior change from tank-treading mode to tumbling mode, and achieves Jeffery's tumbling mode with a large bending stiffness. The present study shows that, besides viscosity ratio and membrane viscosity, the membrane bending stiffness may be another factor which can lead to the transition of a capsule's motion from tank treading to tumbling.

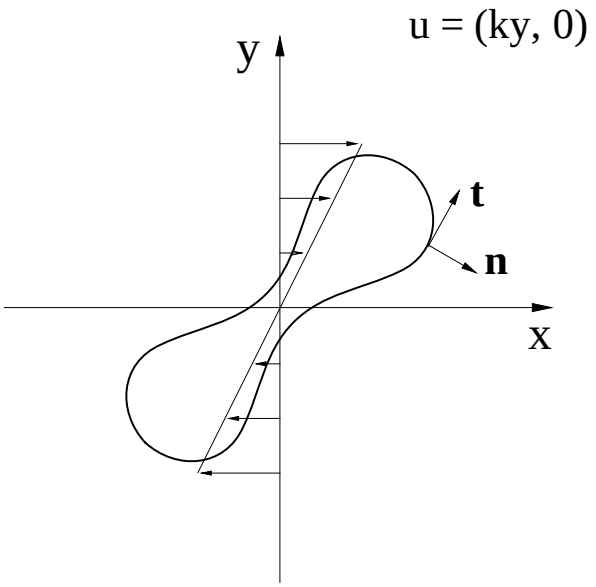

Figure 3.1 Schematic illustration of a two-dimensional capsule in simple shear flow

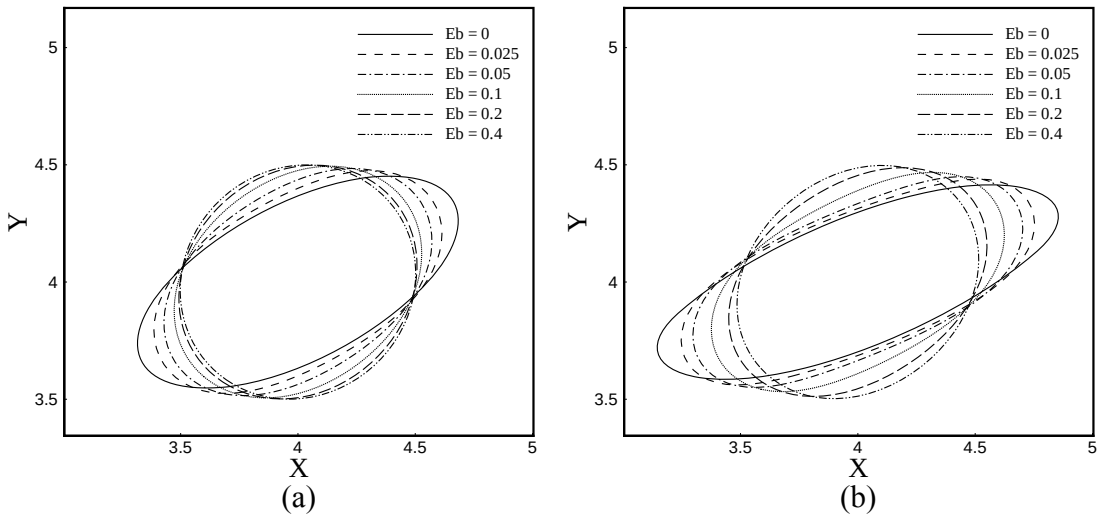

Figure 3.2 Contours of steady deformed capsules with circular initial shape for various bending modulus at dimensionless shear rate: (a) $G = 0.04$; (b) $G = 0.125$

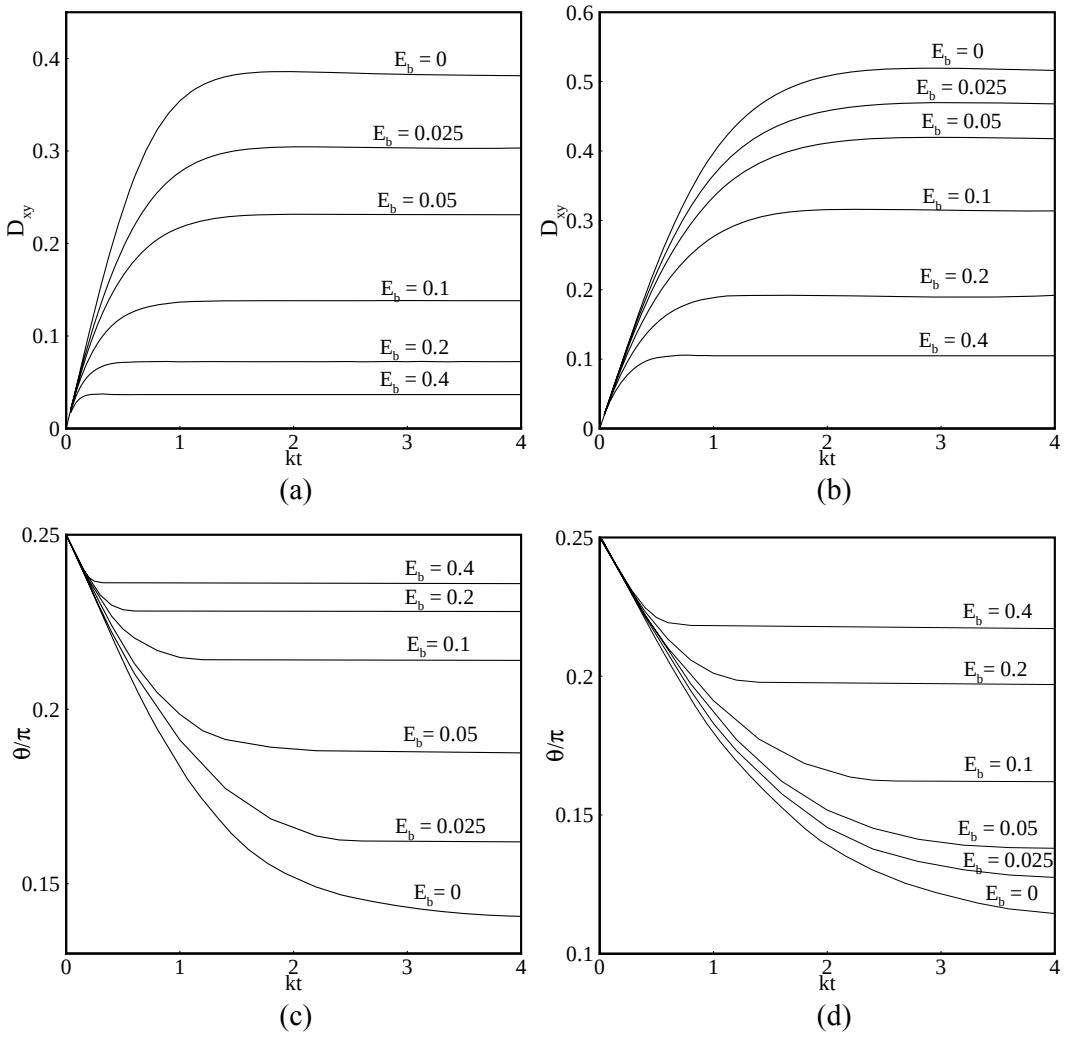

Figure 3.3 Temporal evolution of Taylor deformation parameter for: (a) $G = 0.04$; (b) $G = 0.125$; and inclination angle for: (c) $G = 0.04$; (d) $G = 0.125$

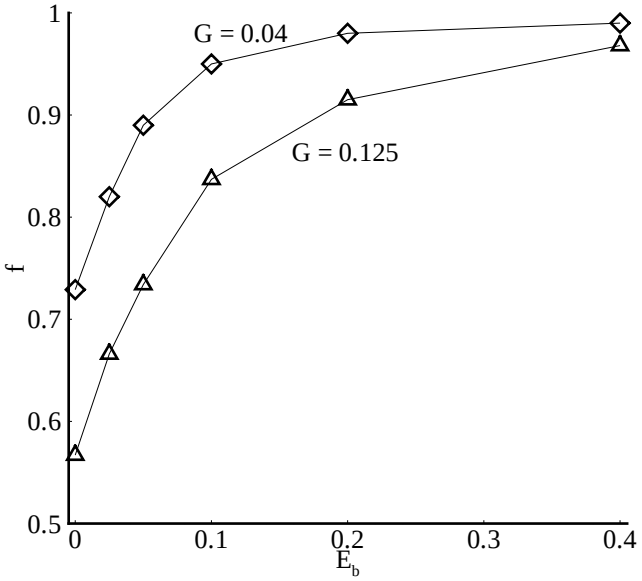

Figure 3.4 The normalized tank treading frequency for various reduced bending modulus at $G = 0.04$ and 0.125

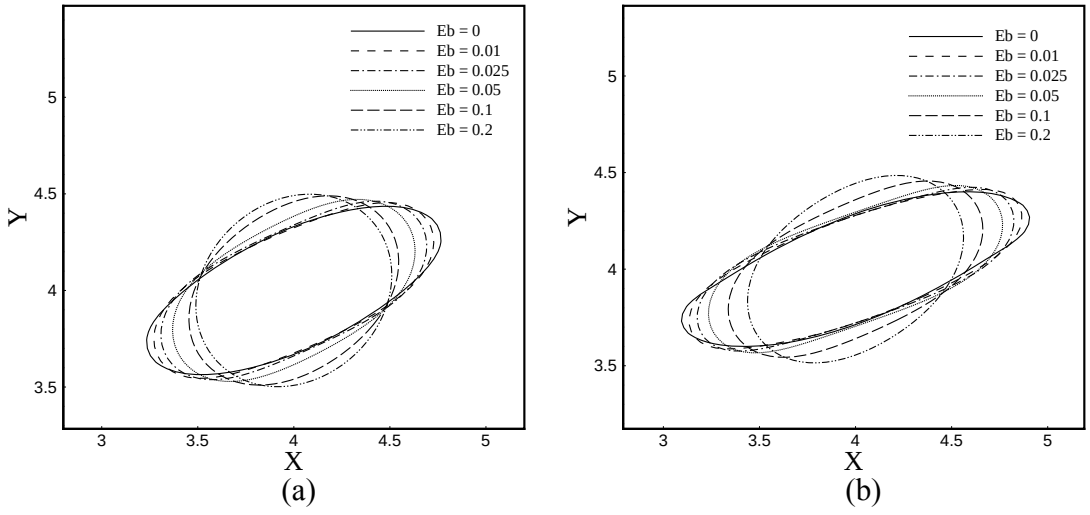

Figure 3.5 Configurations of steady deformed capsules with elliptical initial shape and circular minimum bending-energy configuration under various bending modulus at dimensionless shear rate: (a) $G = 0.04$; (b) $G = 0.125$

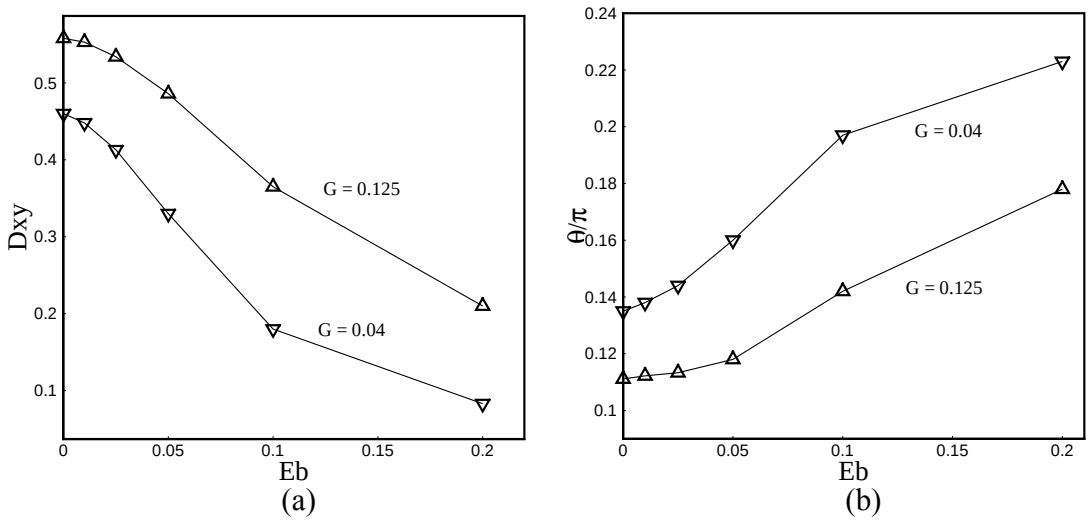

Figure 3.6 Steady (a) Taylor deformation parameters; (b) inclination angles of capsules with different reduced bending modulus at $G = 0.04$ and 0.125

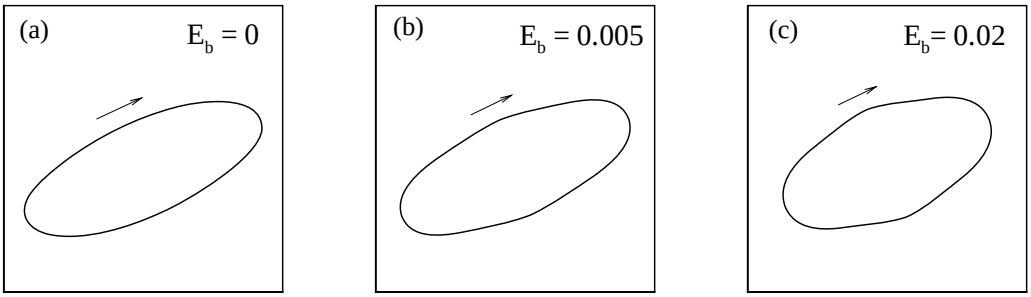

Figure 3.7 Tank treading motion of capsules with the elliptical initial shape as the minimum bending-energy configuration at different bending modulus at $G = 0.04$

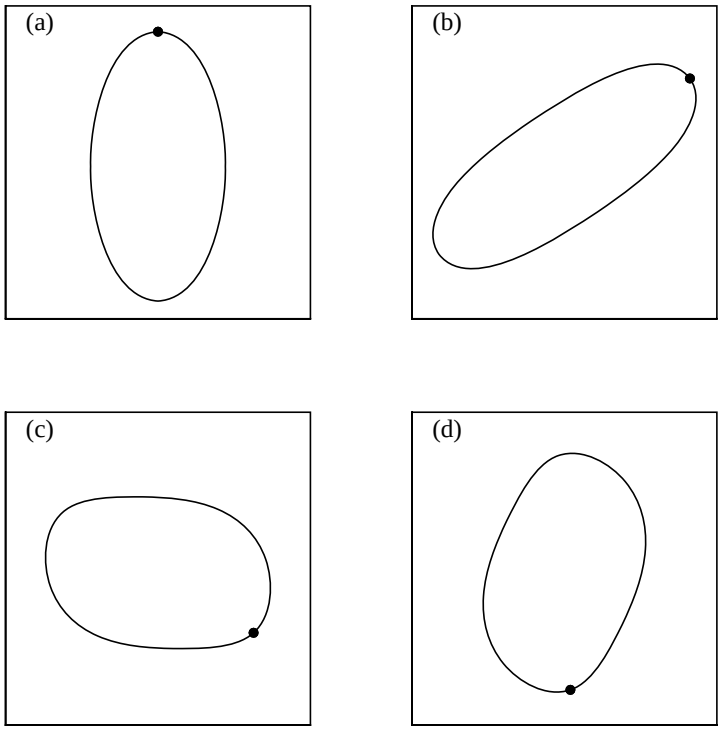

Figure 3.8 Rotating and deforming of a capsule with the elliptical initial shape as the minimum bending-energy configuration at $E_b = 0.06$ and $G = 0.04$. Corresponding dimensionless time are $kt =$ (a) 0, (b) 1.6, (c) 6.4, (d) 8

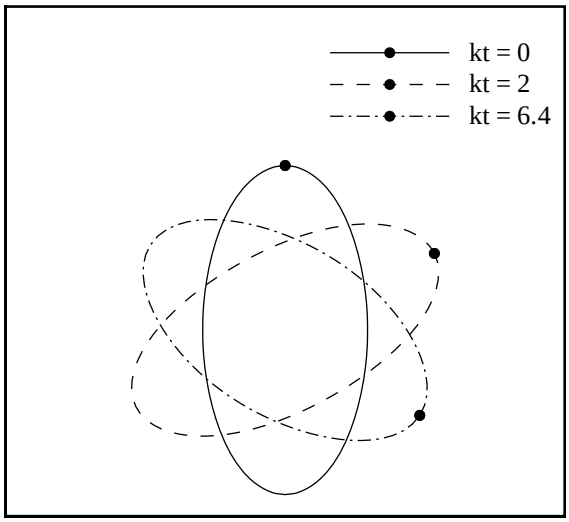

Figure 3.9 Rotating and deforming of a capsule with the elliptical initial shape as the minimum bending-energy configuration at $E_b = 0.4$ and $G = 0.04$

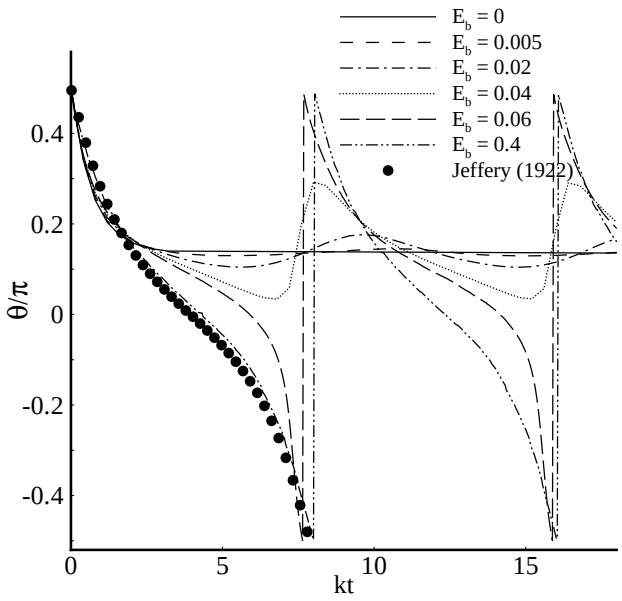

Figure 3.10 Evolution of inclination angle of capsules with the elliptical initial shape as the minimum bending-energy configuration at $G = 0.04$

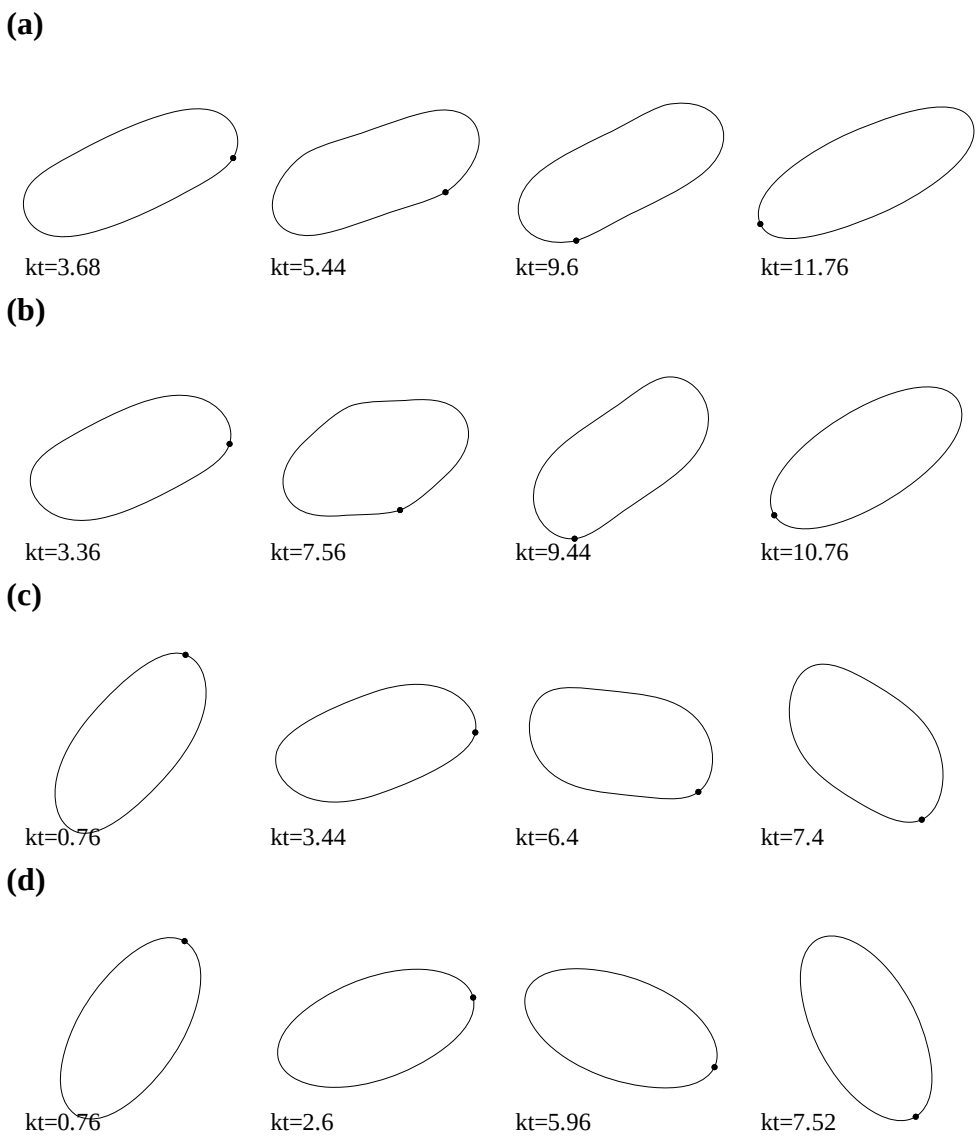

Figure 3.11 Instantaneous snapshots of elliptical capsules' profiles during deformation at $E_b = 0.01$, (a) $G = 0.04$; (b) $G = 0.0125$; (a) $G = 0.00625$; (d) $G = 0.001$

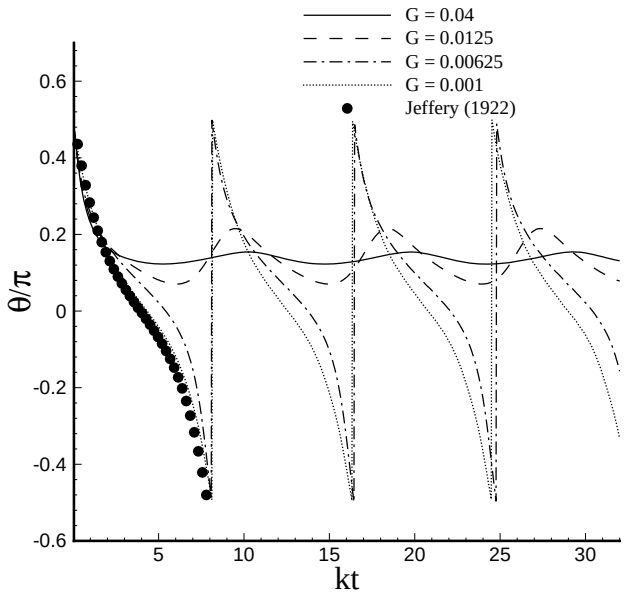

Figure 3.12 Evolution of inclination angle of capsules with the elliptical initial shape as the minimum bending-energy configuration at $E_b = 0.01$

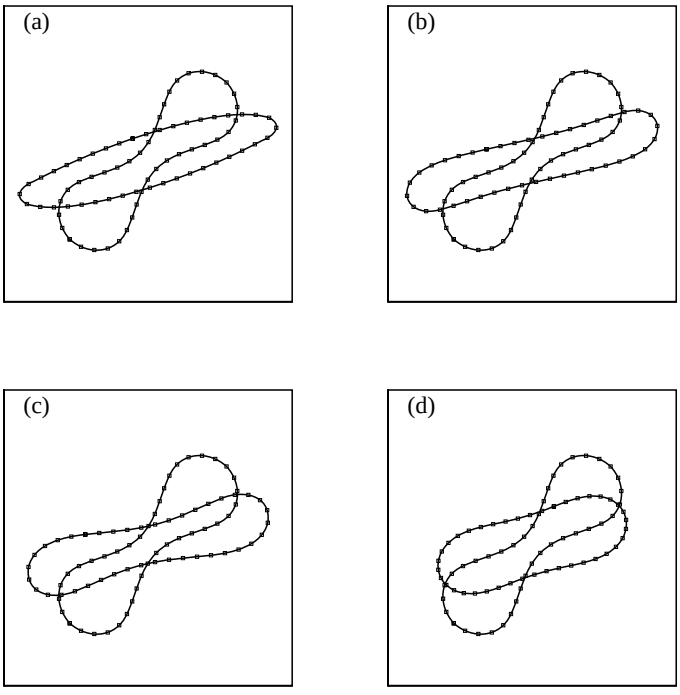

Figure 3.13 Equilibrium shapes of initially biconcave capsules with circular minimum bending-energy configuration at reduced bending modulus E_b = (a) 0, (b) 0.005, (c) 0.02, (d) 0.1 at $G = 0.025$

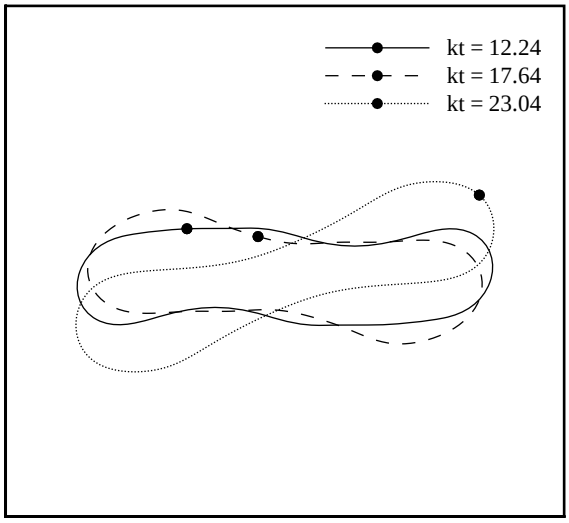

Figure 3.14 Tank treading and deforming of a capsule with the elliptical biconcave shape as the minimum bending-energy configuration at $E_b = 0.015$ and $G = 0.025$

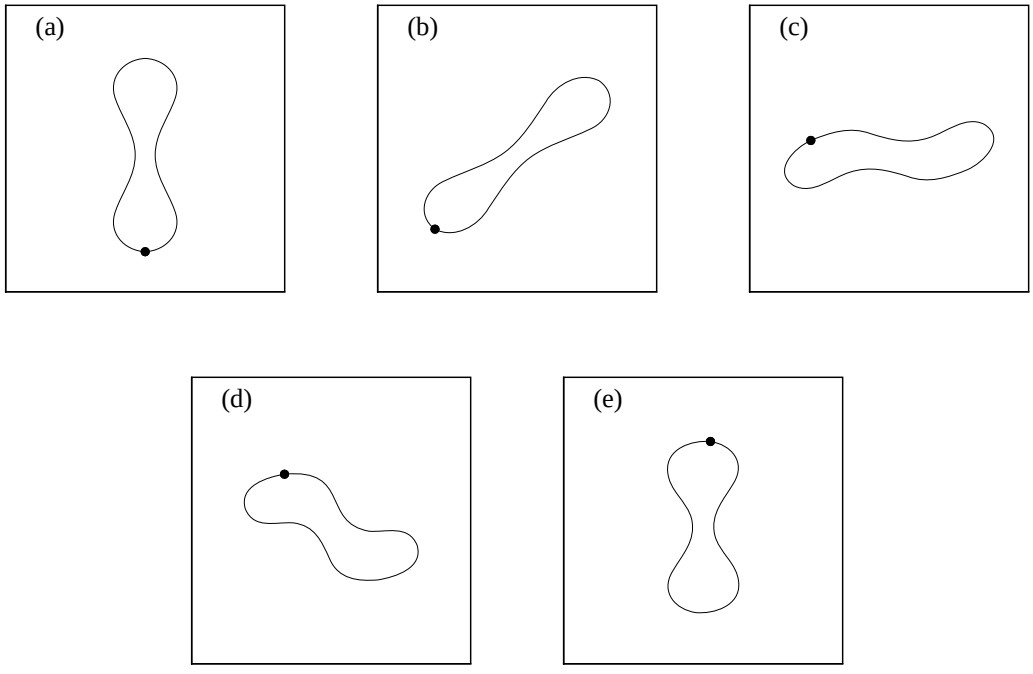

Figure 3.15 Rotating and deforming of a capsule with the elliptical biconcave shape as the minimum bending-energy configuration at $E_b = 0.02$ and $G = 0.025$.
Corresponding dimensionless times are $kt =$ (a) 0, (b) 1.26, (c) 7.38, (d) 14.22, (e)15.66

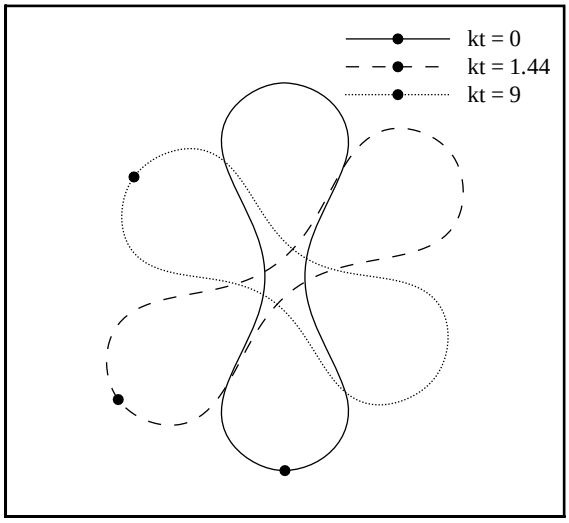

Figure 3.16 Rotating and deforming of a capsule with the elliptical biconcave shape as the minimum bending-energy configuration at $E_b = 0.2$ and $G = 0.025$

(a)

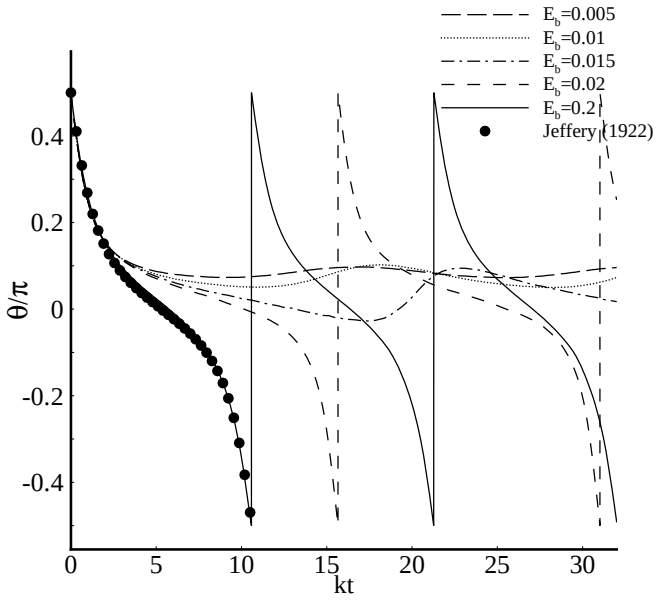

(b)

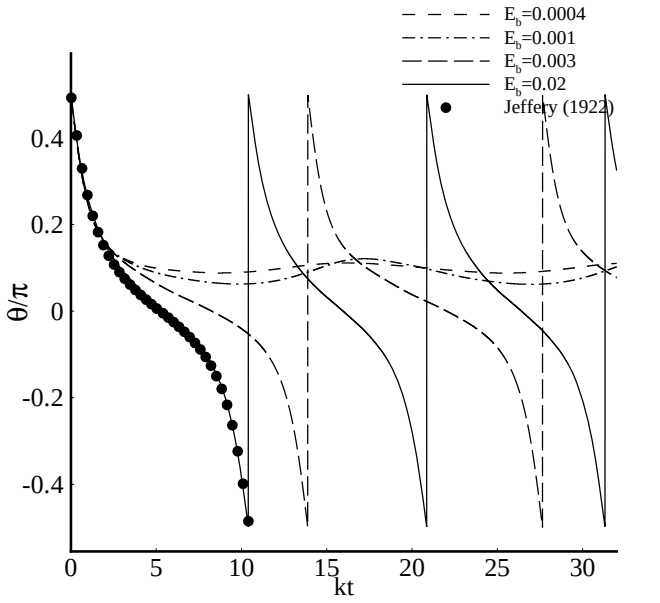

Figure 3.17 Evolution of inclination angle of capsules with the biconcave initial shape as the minimum bending-energy configuration at: (a) $G = 0.025$; (b) $G = 0.0025$

(a)

kt=8.64 kt=16.2 kt=21.06 kt=25.56

(b)

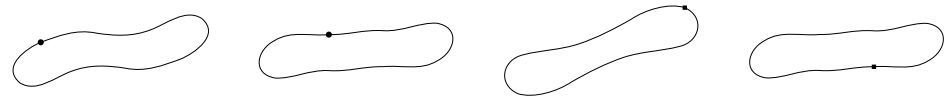

kt=6.66 kt=13.14 kt=19.98 kt=31.36

(c)

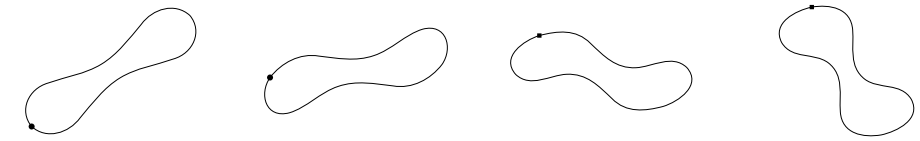

kt=1.62 kt=4.32 kt=11.34 kt=13.5

(d)

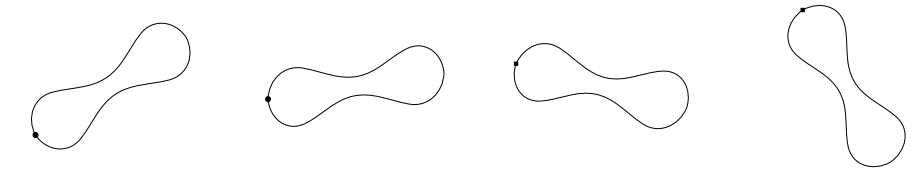

kt=1.62 kt=3.78 kt=7.38 kt=9.9

Figure 3.18 Instantaneous snapshots of biconcave capsules' profiles during deformation at $E_b = 0.01$, (a) $G = 0.04$; (b) $G = 0.02$; (a) $G = 0.01$; (d) $G = 0.001$

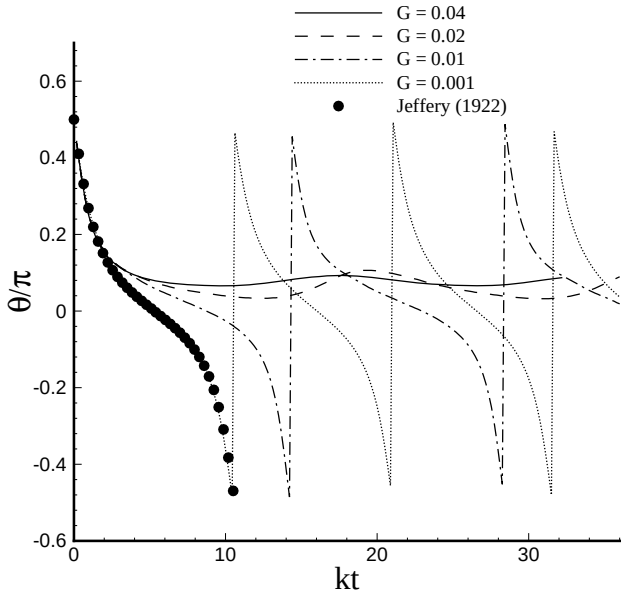

Figure 3.19 Evolution of inclination angle of capsules with the biconcave initial shape as the minimum bending-energy configuration at $E_b = 0.01$

Chapter 4 Inertia Effect on the Deformation of Two-dimensional Capsules in Simple Shear Flow*

The deformation of an elastic capsule under simple shear flow has been studied extensively in the past by experimental observation, theoretical analysis or numerical simulation. Previous researchers have found that there are some factors which play important roles in determining the capsule behaviour in shear field. These factors include the capsule's membrane bending rigidity, membrane viscosity and the viscosity ratio of the internal and external liquids. However, the effects of inertia on the deformation of an elastic capsule and the flow field around it have so far not been explored in simple shear flow. In a related area, Sheth and Pozrikidis (1995) conducted numerical simulations and found that inertia tends to promote the deformation of liquid drops in simple shear flow. Subsequently, Lee and Pozrikidis (2006) found that inertia gives rise to an initial transient process. However, it is known that liquid drops do not have membranes and have constant surface tension. Liquid drops are thus different from the present topic of study, which is on the deformation of liquid filled capsules with elastic membranes.

In this chapter, the transient deformation of two-dimensional liquid-filled capsules is simulated in simple shear flow at small and moderate Reynolds numbers up to Re =

* The results of this chapter have been accepted and will be published as "Sui, Y., Chew, Y. T., Roy, P. and Low H. T., Inertia effect on the transient deformation of elastic capsules in simple shear flow, Comput. Fluids, 38: 49-59, 2009."

100. The capsule is modeled as a closed elastic membrane, filled with a Newtonian liquid similar to that outside. The membrane model follows Hooke's law. The present simulations are carried out with the hybrid method developed in Chapter 2. The purpose of the present study is to investigate the inertia effect on the transient deformation of the elastic capsule, as well as the flow pattern around and inside it.

4.1 Numerical model

In the present study, a two-dimensional capsule is considered to be subjected to a linear shear flow along the x-axis, as illustrated in Figure 4.1. The numerical model employed in this chapter is nearly identical to that in chapter 3, in which the modeling details can be found, and the only difference is that the membrane bending stiffness is neglected. The capsule's membrane follows Hooke's law, as defined by Equation 3.6.

In the present study of the capsules' dynamic motion, the capsule membrane is assumed quite thin compared with the dimension of the capsule. Thus the bending moments are neglected as it is small compared with the shear elasticity effect. It should be noted that the bending stiffness is important in determining the static configuration of capsules.

Finally, the membrane load of an elastic capsule has the form, similar to that of Breyiannis and Pozrikidis (2000):

$$\mathbf{F} = -\frac{d}{dl}(\tau \mathbf{t}) = \kappa \tau \mathbf{n} - \frac{d\tau}{dl}\mathbf{t} \tag{4.1}$$

For drops without surfactant (Sheth and Pozrikidis, 1995), due to the constant interfacial tension τ, the tangential force in Equation 4.1 vanishes.

In the simulations, two dimensionless parameters are identified to play an essential role in determining the capsule deformation and flow structure. One is the dimensionless shear rate G, which determines the relative importance of shearing and elasticity, defined in Chapter 3, Equation 3.9. Another important parameter is the Reynolds number which is the ratio of inertia force to viscous force, defined as:

$$\mathrm{Re} = \frac{\rho UL}{\mu} = \frac{\rho(2ka)(2a)}{\mu} \tag{4.2}$$

where ρ is the fluid density, U represents the characteristic velocity and D is a characteristic length

The present study is based on the hybrid method proposed in Chapter 2. In this approach the flow field is solved by the lattice Boltzmann method, the fluid-capsule interaction is solved by the immersed boundary method, and the multi-block strategy is used to refine the mesh around the deforming capsule. The method is capable to take the inertia effect into account because it solves the lattice Boltzmann equation, which can recover the full Navier-Stokes equation. In study of micro-capsules, for example in Chapter 3, the resulted Reynolds number is less than 0.1, thus inertia effect is negligible.

4.2 Results and discussion

The deformation of capsules with initially circular and elliptical resting shapes (shapes at which the in-plane tension around the membrane is zero everywhere) in

simple shear flow is studied, at various dimensionless shear rates and Reynolds numbers. All cases considered in the present study are for shear rate G below the critical values, in which the capsules can achieve steady profiles. Around and above the critical values, the deformation of the capsules will be very large and high curvature regions will develop, and mesh refinement is needed. The results presented in this section correspond to capsules with circular resting shape. Capsules with elliptical resting shape (semimajor to semiminor axes ratio 2:1) are found to behave in a similar way.

4.2.1 Numerical performance

The present study is on the deformation of a capsule in infinite simple shear flow. It is quite important to choose a computational domain which is large enough to neglect the boundary effect and a sufficient grid resolution to get convergent results. Numerical simulations are carried out under various computational domain sizes and grid resolutions to test the performance of the numerical method. The temporal evolution of the capsule's Taylor shape parameter D_{xy} and the capsule's inclination angle (with respect to x-axis) are chosen as indicators.

First studied is the computational domain effect. The square computational domains with side length of $12a$, $16a$ and $20a$ are tested. The capsule is at the center of the domain, and its membrane is discretized into 160 Lagrangian nodes equally-spaced with respect to arc length around the membrane contour. The fine mesh block covers a small square box with side length $6a$ and center coinciding with that of the computational domain. The other area is covered with coarse mesh. The grid

resolutions in fine and coarse block are $\Delta x_f = \Delta y_f = 0.05a$ and $\Delta x_c = \Delta y_c = 0.1a$, respectively. In the present study, the initial flow field is chosen to be the unperturbed simple shear flow. The density distribution functions are set to be the equilibrium values. During the computation, the outer boundary condition is set to be the unperturbed simple shear flow. A non-equilibrium extrapolation method proposed by Guo et al. (2002) is used to treat this boundary condition. The temporal evolution of Taylor shape parameter and capsule inclination angle under various domain sizes at Re = 100 is presented in Figure 4.2(a) and Figure 4.2(b) respectively. It is shown that a square computational domain with side 16a is large enough to neglect the boundary effect.

Grid convergence study was carried out on the computational domain with side 16a. The diameter of the circular capsule 2a was covered by 30, 40 or 50 lattice spaces of the fine mesh block, and the capsule membrane was discretized into 120, 160 or 200 Lagrangian nodes equally-spaced with respect to arc length, respectively. The ratio of the marker spacing to grid width was kept to be about 0.79. The temporal evolution of Taylor shape parameter and capsule inclination angle under various grid resolutions at Re = 100 is presented in Figure 4.3(a) and Figure 4.3(b). From the result it is seen that the grid resolution of $\Delta x_f = \Delta y_f = 0.05a$ is sufficient to capture the important characteristics. With the same mesh resolution, the capsule membrane was discretized into 240 Lagrangian nodes. The temporal evolution of Taylor shape parameter and capsule inclination angle (Figure 4.3) nearly coincide for the two discretizations. Thus for all cases considered in this paper, the computational domain is a square box with side length 16a, the grid resolution is $\Delta x_f = \Delta y_f = 0.05a$, and the capsule

membrane is discretized into 160 Lagrangian nodes equally-spaced with respect to arc length.

The deformation of capsules in simple shear flow at vanishing Reynolds numbers was studied by the present authors with the same numerical model in Chapter 2; the results were compared with that in published literatures. Satisfactory agreements were observed which validated the present model. With the multi-block technique, the typical computational time for a case is around 10 hours (on the SVU linux 64 cluster).

4.2.2 The capsule deformation

The deformation of capsules under various dimensionless shear rates and Reynolds numbers is simulated. As soon as the capsules are immersed into the unperturbed linear shear field, they start to elongate. Figure 4.4 shows the effect of Reynolds number on the temporal evolution of the Taylor shape parameter of the capsule under various dimensionless shear rates. From the results it is seen that before the capsules achieve steady states, there is a transient process due to the inertia effect, especially at higher Reynolds numbers and lower dimensionless shear rates. This phenomenon is quite different from that of capsule deformation in simple shear flow at zero Reynolds number, in which the capsules achieve steady states monotonically. In the transient period, the Taylor shape parameter shows dampened oscillations. Under the same dimensionless shear rates, the oscillation amplitudes increase with increasing Reynolds number, and so does the transient period. Similar transient process, which is due to the effect of inertia, has been observed for liquid drops in the study of

Pozrikidis and coauthors (Sheth and Pozrikidis, 1995; Lee and Pozrikidis, 2006). In the study of Sheth and Pozrikidis, continued deformation of the drops was observed when the Taylor shape parameter exceeded 0.6. The present results for capsules shows that even the Taylor shape parameter exceeds 0.75, the capsule could still deform to a steady shape. This is because of the different interfacial properties of drops and elastic capsules. After the transient period, the capsules achieve steady configurations. Through comparison of the steady Taylor shape parameters at different Reynolds numbers, it is found that the inertia effect promotes the capsule deformation. The curves in Figure 4.4(a) are for Re = 1, for which the inertia effect would not be large. Nevertheless, some differences are perceptible when compared with those without inertia, especially at higher shear rates.

Figure 4.5 presents the temporal evolution of the inclination angle (with respect to x-axis) of the capsule under various dimensionless shear rates and Reynolds numbers. Similar to that of the Taylor shape parameter, a transient process which is especially apparent at higher Reynolds numbers and lower dimensionless shear rates is observed. An interesting phenomenon, which also documents the importance of inertia, is that the capsule inclination exceeds 45 degrees and even approaches 90 degrees at higher Reynolds numbers. This is impossible for capsule deformation in simple shear flow without inertia, in which the capsule inclination has a maximum limit of 45 degrees (Barthès-Biesel, 1980). In Figure 4.5(a), it was found that the present results for Re = 1 are very different from that of Breyiannis and Pozrikids (2000). This is because their results is for Re = 0 by the boundary element method. This shows that the inclination is sensitive to inertia effect.

To give a more direct illustration of the inertia effect on capsule deformation, the steady configurations of capsules with constant dimensionless shear rates at various Reynolds numbers are presented in Figure 4.6. The results show that inertia promotes capsule elongation. In Figure 4.6 (b), it is seen that at Re = 100, the capsule is highly elongated and dimples formed at the middle, which makes the capsule look like the cross section of a dumbbell. This is quite different for capsules under large elongation in simple shear flow without inertia, in which the capsule are more slender at the two ends. As for the capsule inclination, it is seen that for G = 0.003125 the inclination angle is larger at higher Reynolds numbers; however, this is not apparent for G = 0.04.

In all the cases considered, the capsule finally achieves steady shapes and then the membrane rotates around the liquid inside (tank treading motion). The tank treading velocity and tank treading frequency of the capsules under various Reynolds numbers are studied. The tank treading frequency is calculated by: $f = 2\pi/T$, where T is the time for the capsule membrane to rotate for a whole circle. The tank treading frequency is normalized by the shear rate k. From the results presented in Figure 4.7, it is seen that the tank treading velocity decreases with increasing Reynolds number. As the capsule elongation is larger at higher Reynolds number, the tank treading frequency will be further lower (Figure 4.7b); that is, inertia slows the membrane rotation.

4.2.3 Flow structure and vorticity field

The flow structure around and inside a capsule may be of interest in areas such as drug delivery to estimate the mass transport. From the present results, it is found that inertia has large effect on the flow pattern around and inside a capsule. Figures 4.8(a - d) present the streamline patterns and velocity vectors for G = 0.003125, at different Reynolds numbers. The bold solid line represents the capsule interface. It is seen that the interface forms a closed streamline, with the arrow showing the direction of tank treading. This confirms that the capsules have achieved steady states. Single eddies formed inside the capsule and recirculating regions are observed at the two ends of the capsule. The intensity of the velocity field is presented by velocity vectors shown in the figures. Around the cell, the velocity magnitude decreases with increasing Reynolds.

Figures 4.9(a - d) present the result for higher G = 0.04, at various Reynolds numbers. The capsule deformation is larger and most flow features are similar to that in Figure 4.8. However, it is quite interesting to find in Figure 4.9(d) that the internal flow separates at the high curvature regions and two secondary eddies have developed. The inertia has caused flow separation.

Also studied is the effect of inertia on the vorticity field around and inside a capsule. Vorticity is produced on the interface due to the elastic tension and fluid viscosity, then it is advected by the surrounding fluid, and at the same time diffuses into the fluid. Figures 4.10(a - d) and Figures 4.11(a - d) present the three-dimensional and contour plots of vorticity magnitude for G = 0.003125 and 0.04, at

various Reynolds numbers. The vorticity is normalized by the shear rate k. The bold solid line represents the capsule interface. In all cases studied, it is found that the maximum vorticity appears at the region with highest curvature. From the three-dimensional contour plots of vorticity magnitude, it is seen that with increasing Reynolds number, the vorticity magnitude increases. At higher Reynolds numbers, the convective effect is more prevalent and the vorticity gradient is larger on the interface.

4.3 Concluding remarks

By combining the immersed boundary method with the multi-block lattice Boltzmann model, the transient deformation of a cylindrical liquid-filled capsule with elastic membrane is studied in simple shear flow at small and moderate Reynolds numbers. The purpose of the study is to investigate the inertia effect on the transient deformation of the elastic capsule and the flow structure around it.

The simulation results show that the inertia effect gives rise to a transient process, in which the capsule elongation and inclination overshoot and then show dampened oscillations towards the steady states. Inertia effect also promotes the steady deformation, and decreases the tank treading frequency of the capsule. Inertia effect strongly affects not only the capsule deformation, but also the flow pattern. There is flow separation inside the capsule. Also, the vorticity magnitude and gradient on the capsule interface increase with increasing Reynolds number.

The present model is general in that it can be implemented to capsules with arbitrary resting configurations and membrane constitutive laws. The present simulation is two-dimensional, and quantitative differences may arise if three-dimensional simulations are carried out. However, the major conclusion of the present investigation is expected to hold in three-dimensional study.

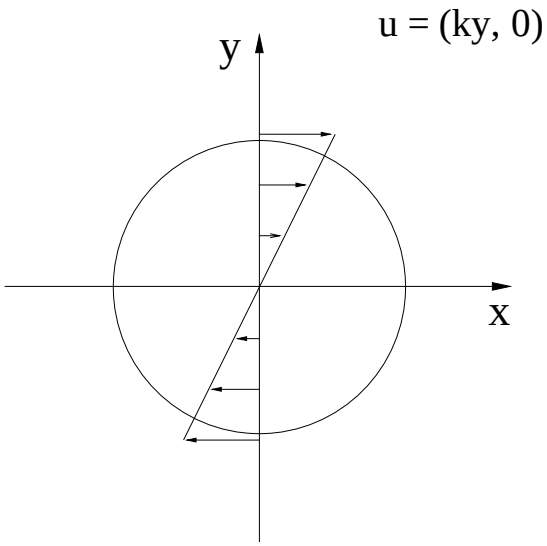

Figure 4.1 Schematic illustration of a two-dimensional circular capsule in simple shear flow

(a)

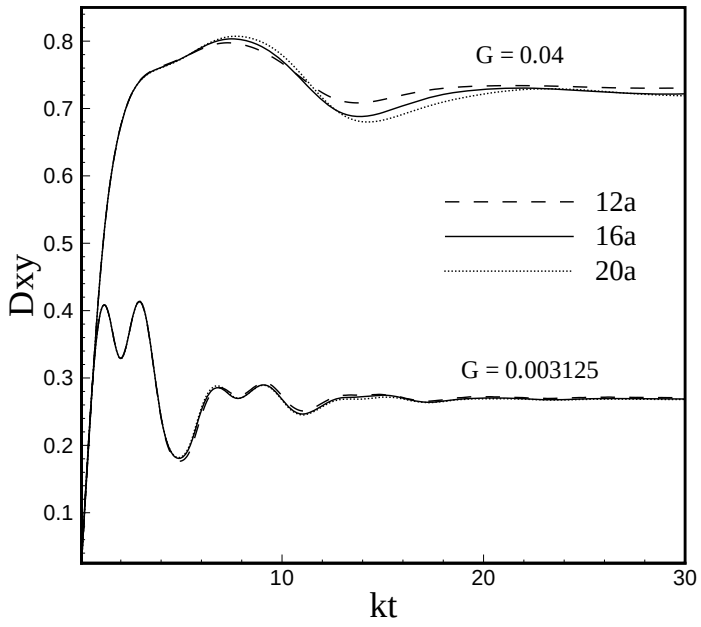

(b)

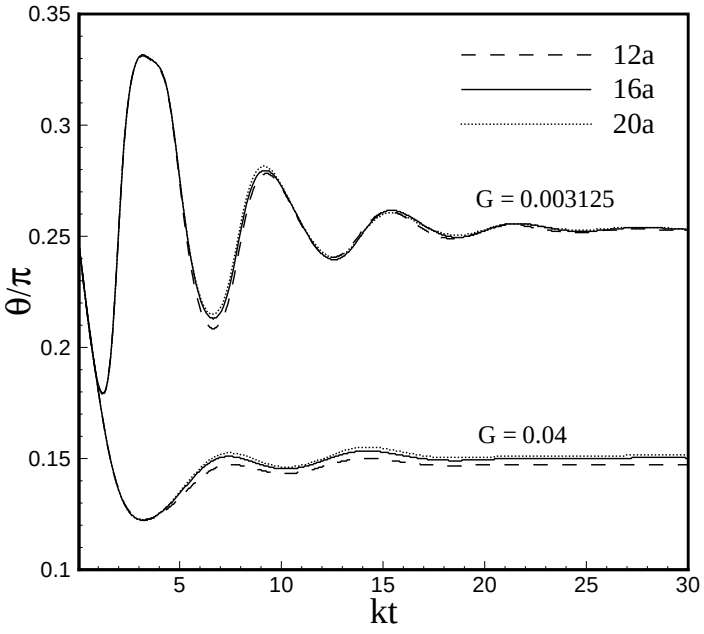

Figure 4.2 Temporal evolution of the capsule's (a) Taylor shape parameter; (b) inclination angle under various domain sizes at Re = 100

(a)

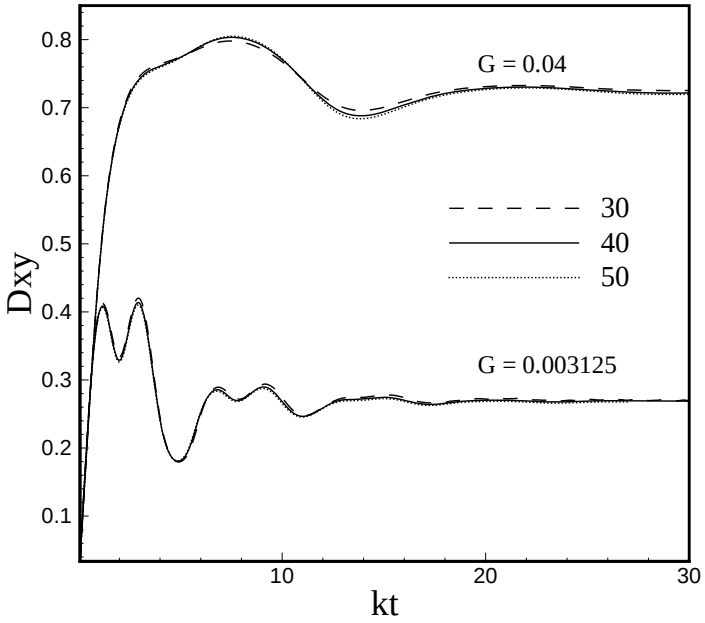

(b)

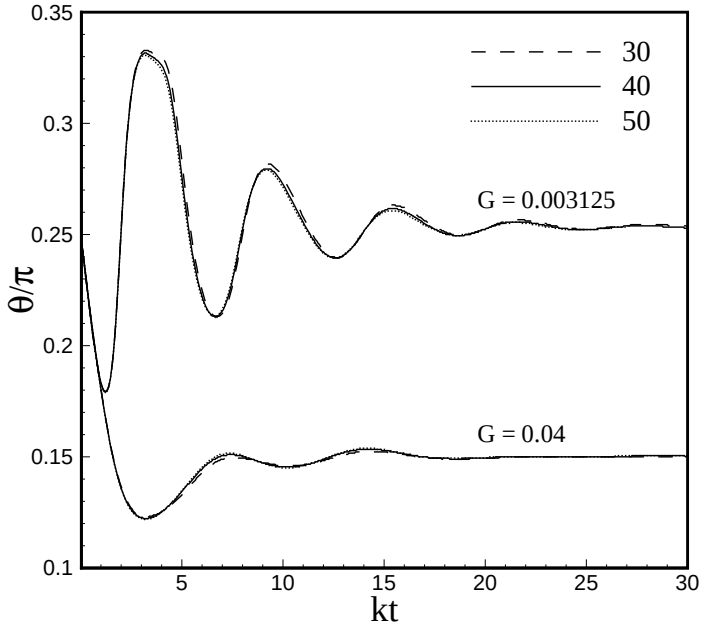

Figure 4.3 Temporal evolution of the capsule's (a) Taylor shape parameter; (b) inclination angle under various grid resolutions at Re = 100

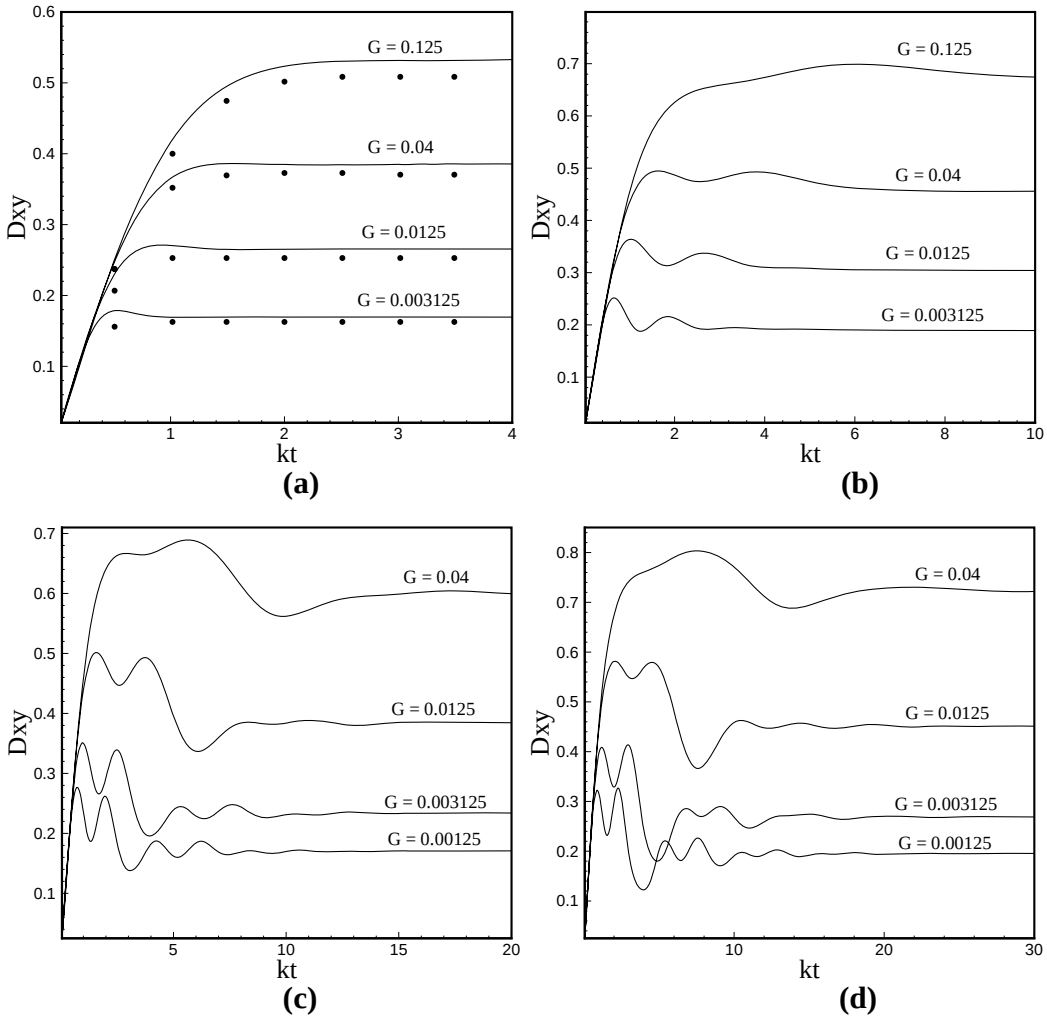

Figure 4.4 Effect of Reynolds number on the evolution of Taylor shape parameter of the capsule under various simensionless shear rates. (a) Re = 1 (● is the result of Breyiannis and Pozrikids (2000) for Re = 0); (b) Re = 10; (c) Re = 50; (d) Re = 100

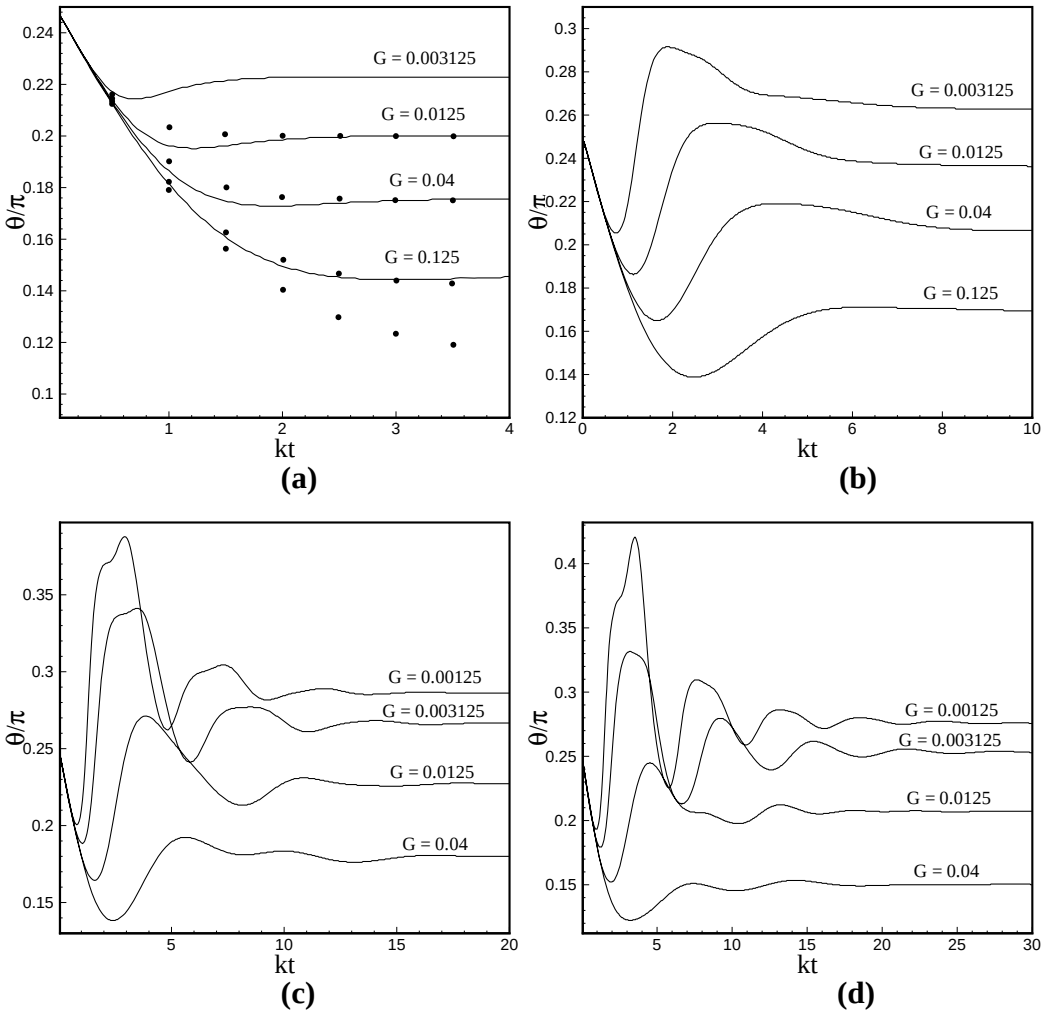

Figure 4.5 Effect of Reynolds number on the evolution of inclination angle of the capsule under various simensionless shear rates. (a) Re = 1(● is the result of Breyiannis and Pozrikids (2000) for Re = 0); (b) Re = 10; (c) Re = 50; (d) Re = 100

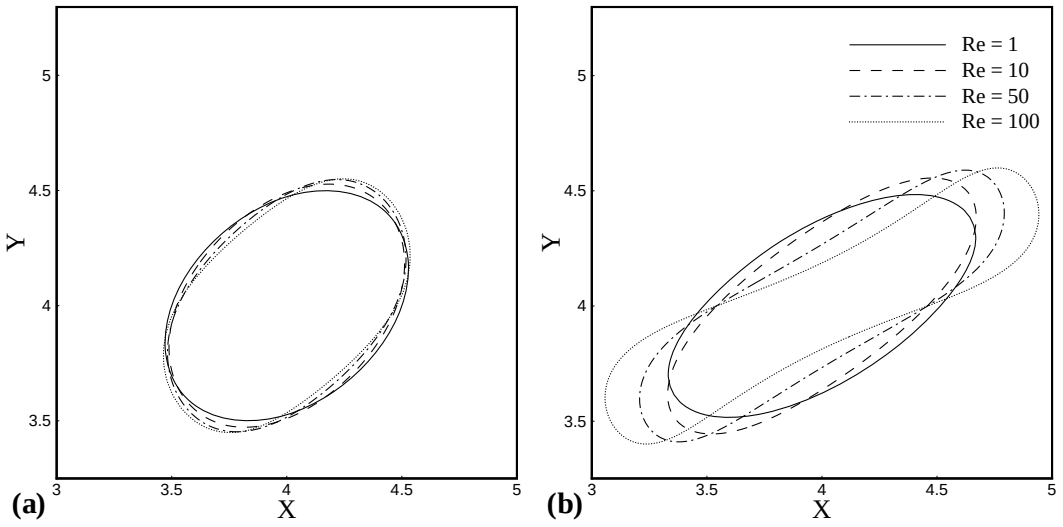

Figure 4.6 Steady configurations of capsules at various Reynolds numbers.(a) G = 0.003125; (b) G = 0.04

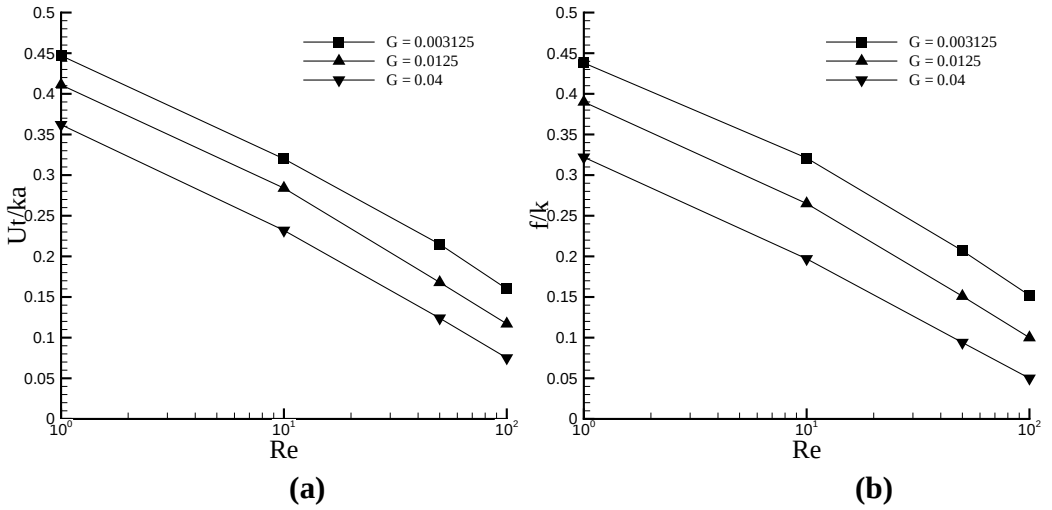

Figure 4.7 (a) Averge tank treading velocity; (b) tank treading frequency of capsules at various dimensionless shear rates and Reynolds numbers

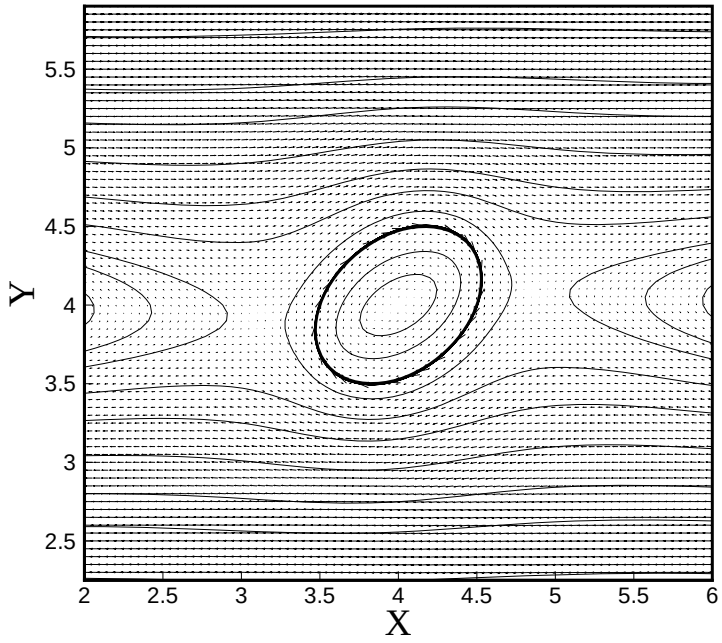
5.5
5
4.5
4
3.5
3
2.5
Y
2
2.5
3
3.5
4
4.5
5
5.5
6
X

(a)

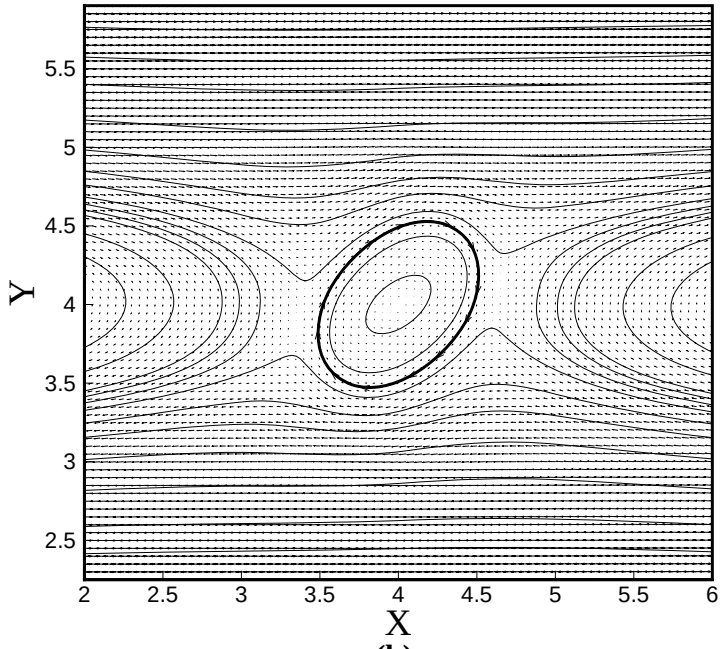
5.5
5
4.5
4
3.5
3
2.5
Y
2
2.5
3
3.5
4
4.5
5
5.5
6
X

(b)

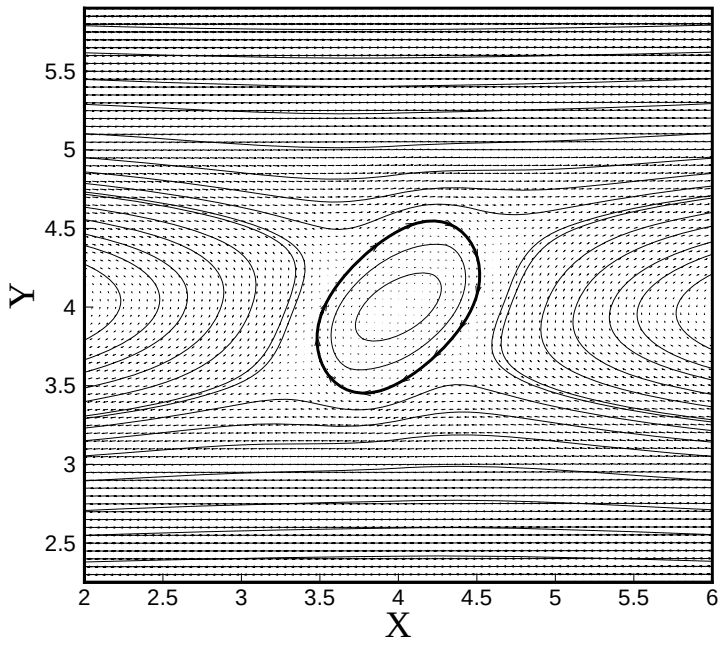

(c)

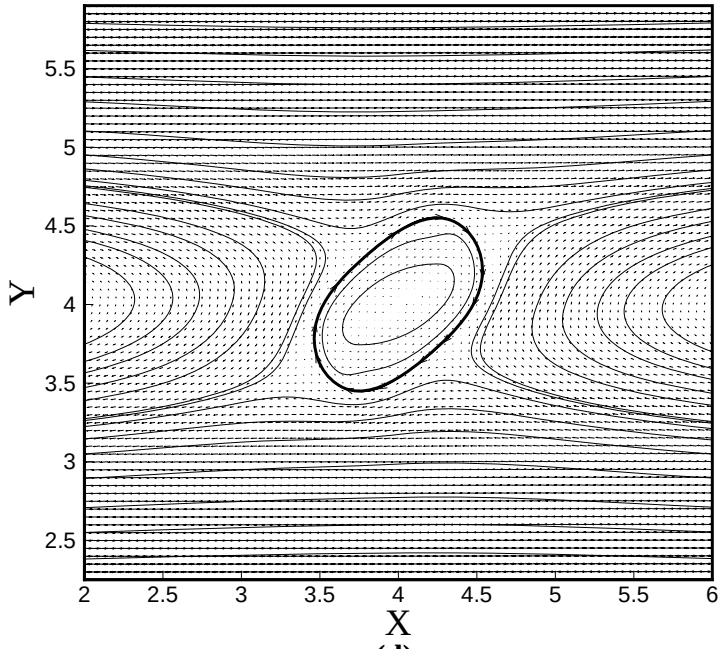

(d)

Figure 4.8 Stream patterns and velocity vectors around the capsule for G = 0.003125. (a) Re = 1; (b) Re = 10; (c) Re = 50; (d) Re = 100

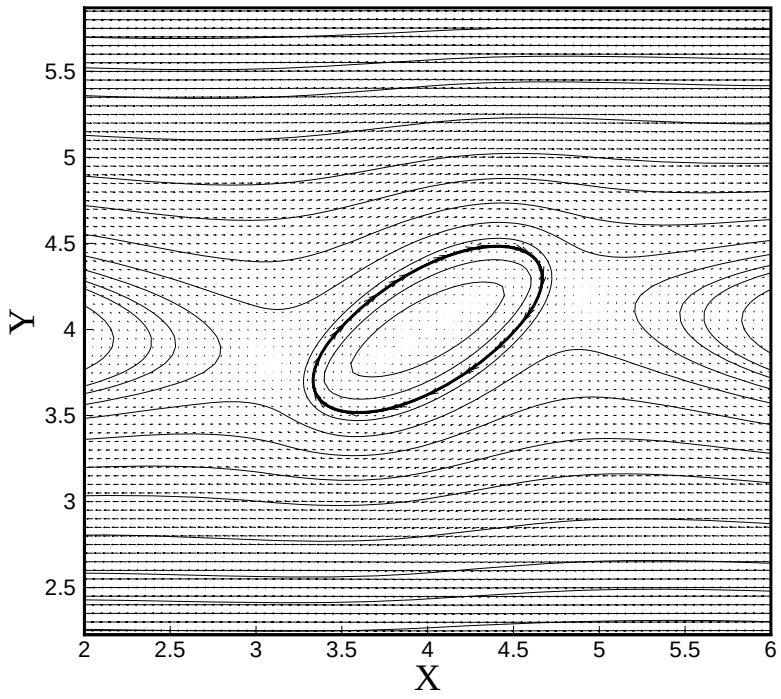
Y
X
5.5
5
4.5
4
3.5
3
2.5
2
2.5
3
3.5
4
4.5
5
5.5
6

(a)

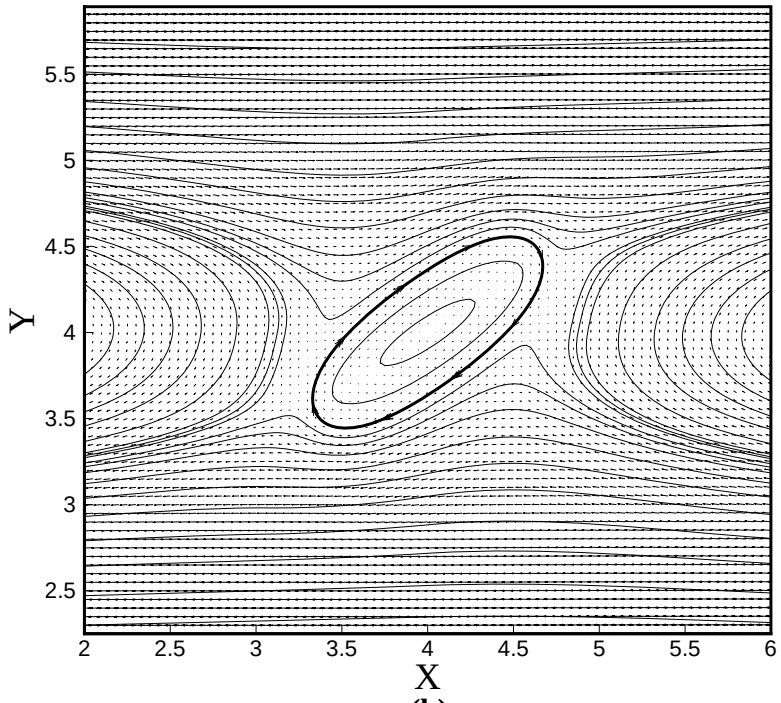
Y
X
5.5
5
4.5
4
3.5
3
2.5
2
2.5
3
3.5
4
4.5
5
5.5
6

(b)

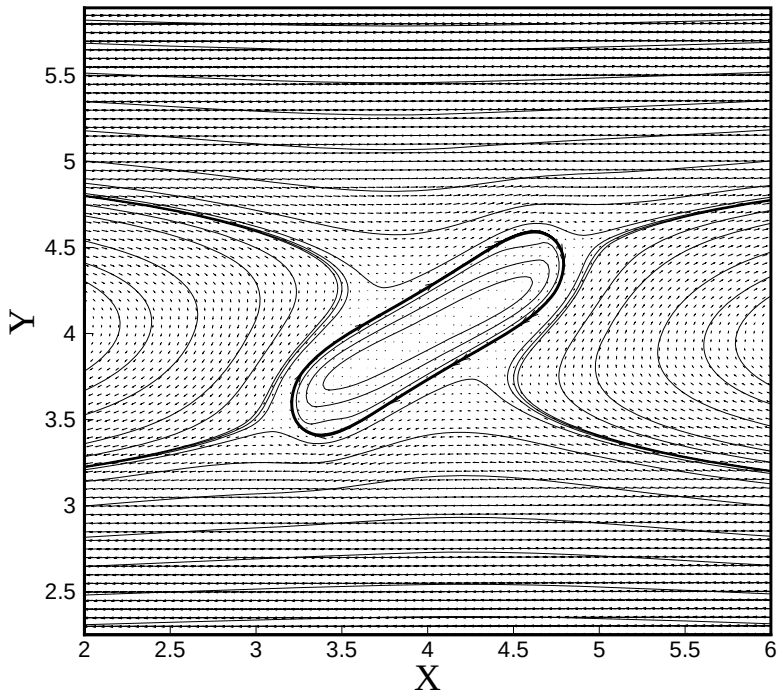

(c)

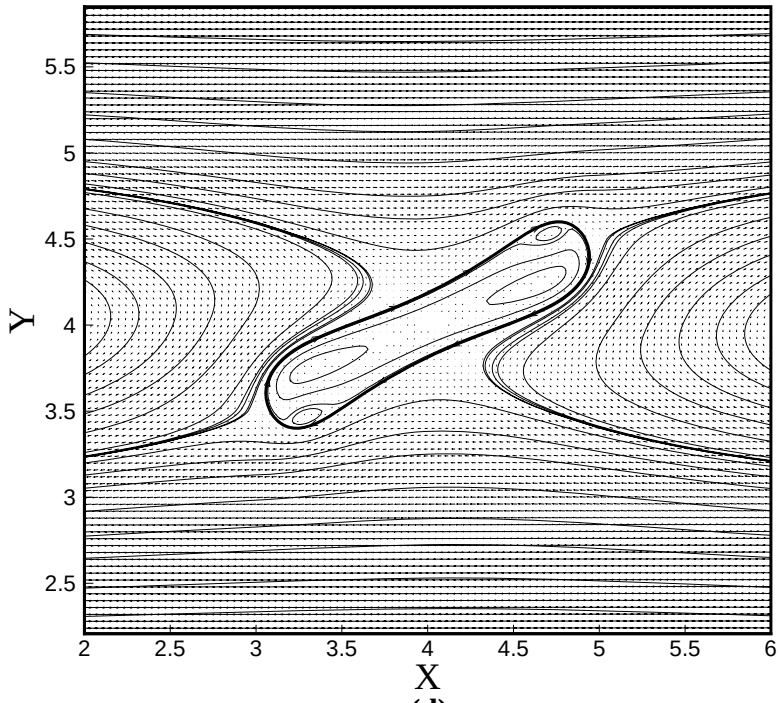

(d)

Figure 4.9 Stream patterns and velocity vectors around the capsule for G = 0.04. (a) Re = 1; (b) Re = 10; (c) Re = 50; (d) Re = 100

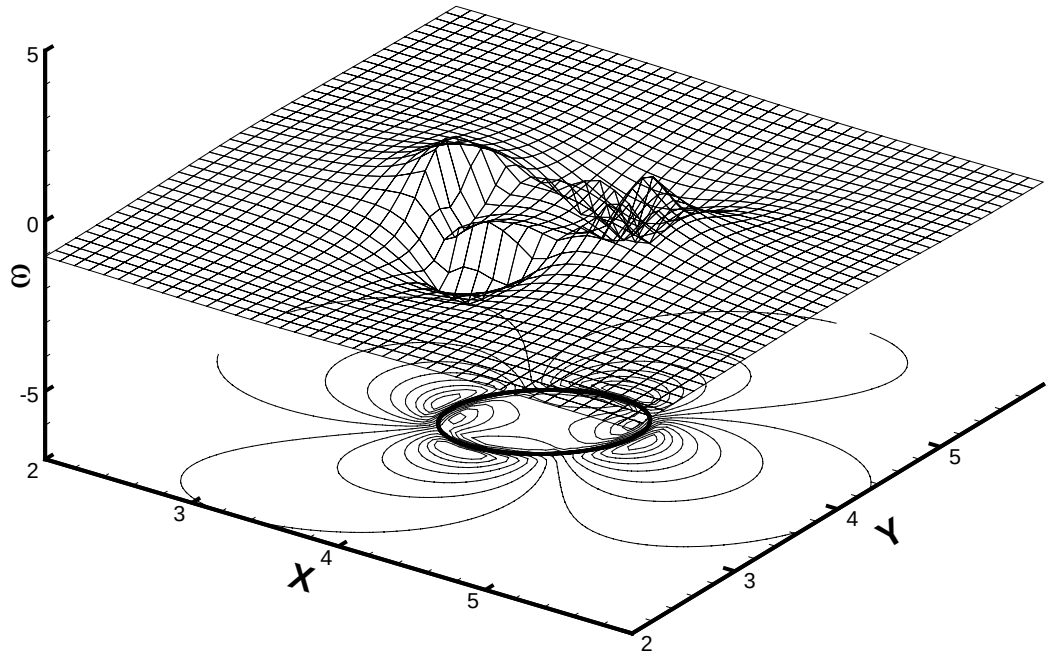

(a)

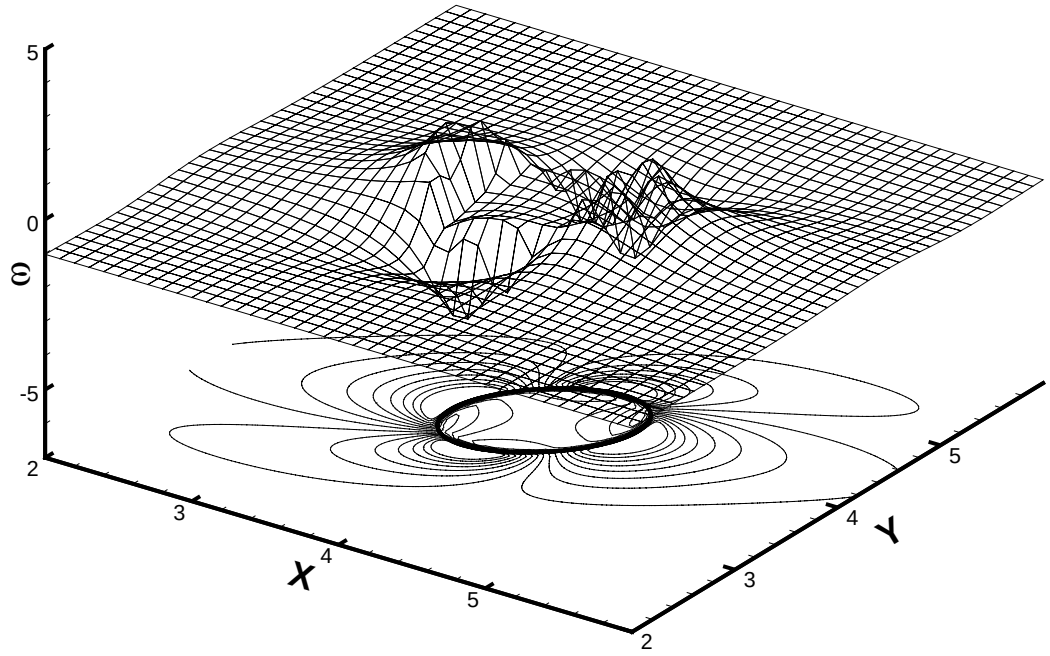

(b)

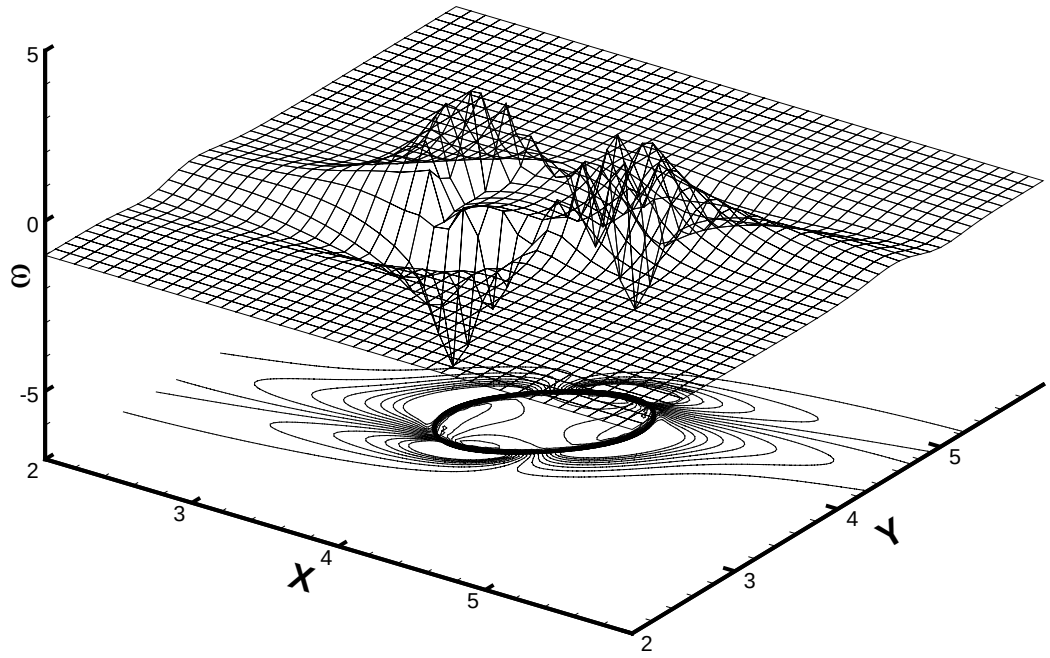

(c)

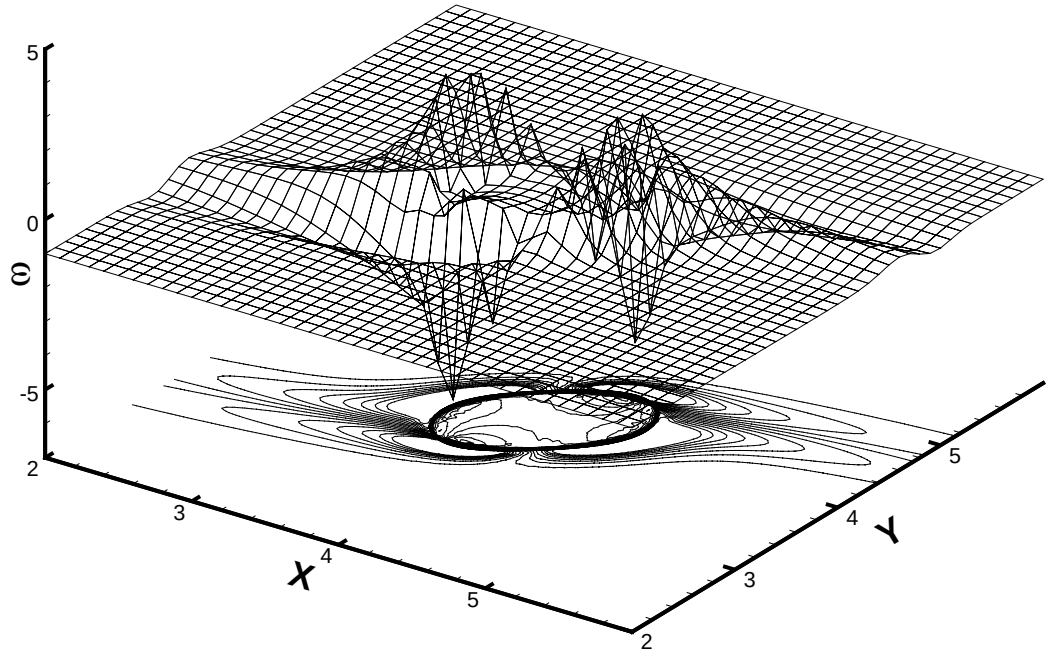

(d)

Figure 4.10 Three-dimensional and contour plots of vorticity for G = 0.003125 at (a) Re = 1; (b) Re = 10; (c) Re = 50; (d) Re = 100

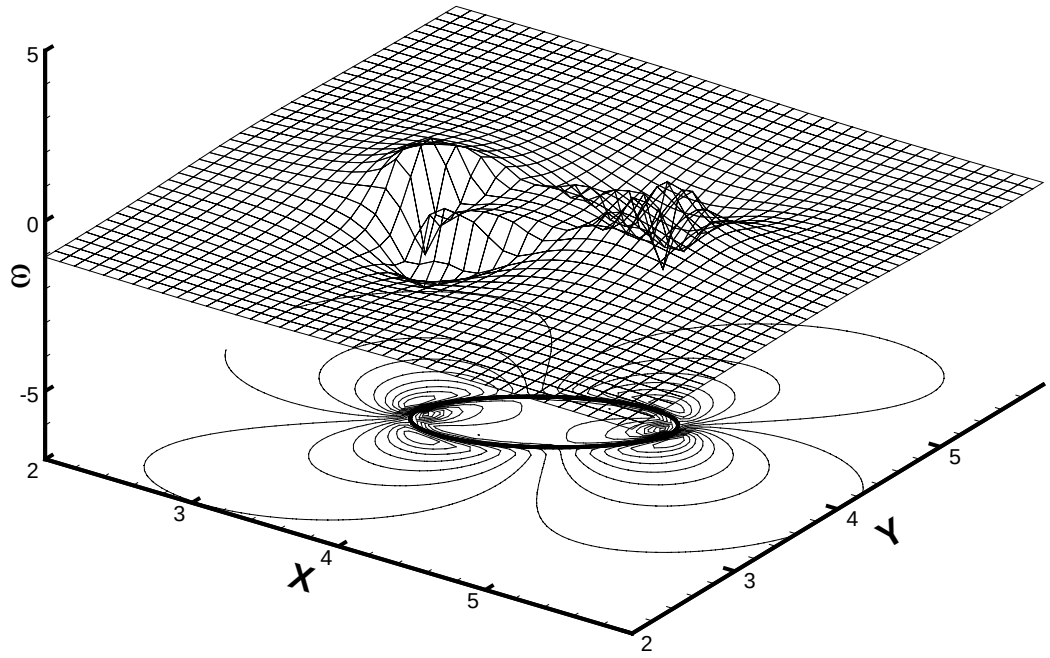

(a)

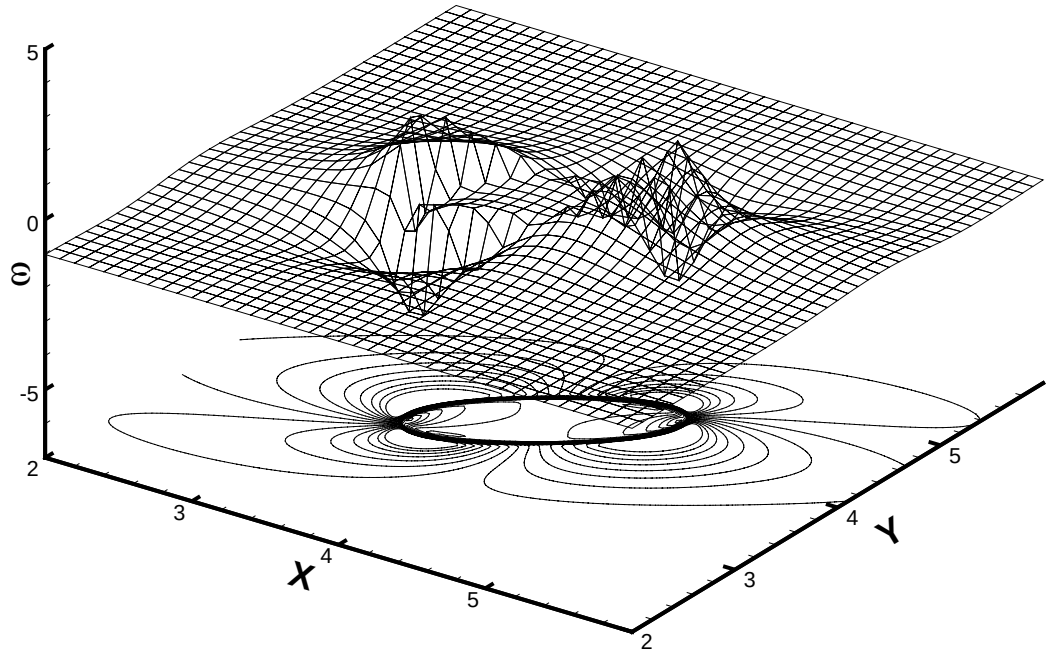

(b)

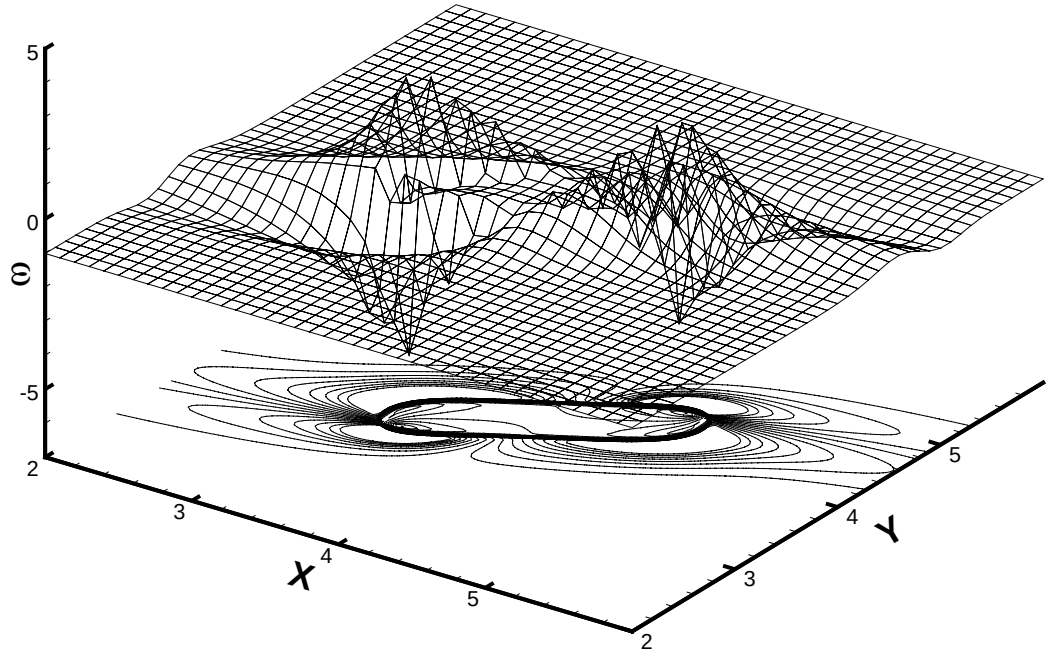

(c)

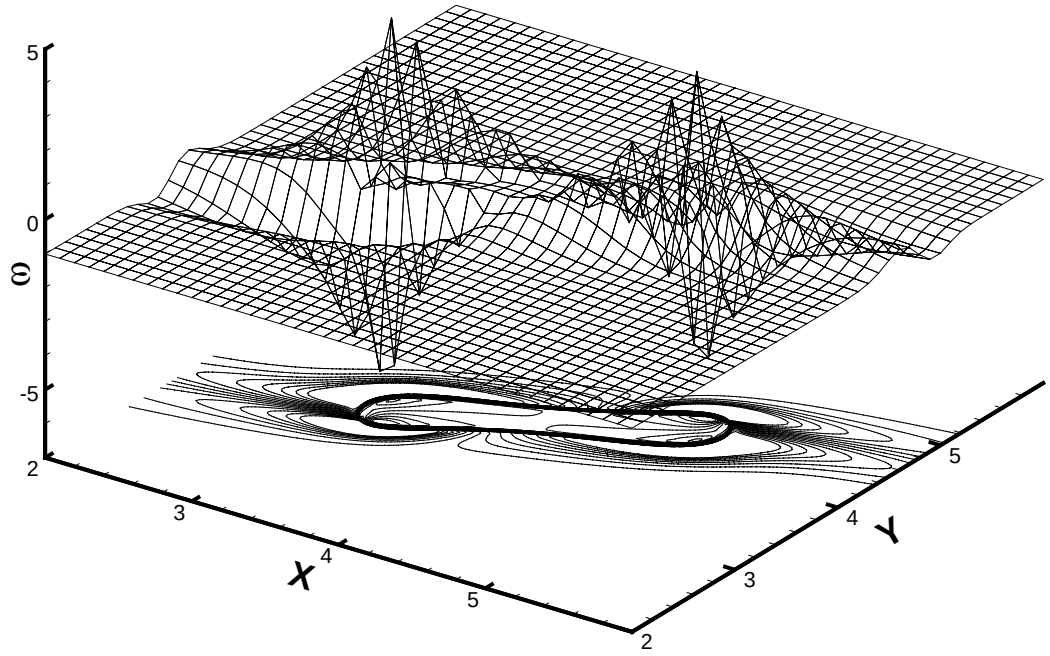

(d)

Figure 4.11 Three-dimensional and contour plots of vorticity for G = 0.04 at (a) Re = 1; (b) Re = 10; (c) Re = 50; (d) Re = 100

Chapter 5 A Hybrid Method to Study Flow-induced Deformation of Three-Dimensional Capsules*

The hybrid immersed boundary and multi-block lattice Boltzmann method, developed in Chapter 2, is capable to study the flow-induced deformation of two-dimensional capsules. However, real capsules are three-dimensional. Although two-dimensional simulation shares a number of common features with three-dimensional study, it must be noted that for flow-induced deformation of capsules, two-dimensional simulation is a large simplification and may miss some features. Two-dimensional membrane model can not suitably describe real three-dimensional capsule membrane properties. Furthermore, the numerical modeling capsules in two and three dimensions are very different. Three-dimensional numerical modeling is much more complicated. The main difficulty comes from modeling the capsule interface. For example, the membrane of a two-dimensional capsule is an elastic ring, and it is not difficult to discretized it into a set of line elements. The membrane tension can also be easily obtained from the strain of the line elements. For three-dimensional capsules, the discretization of the membrane involves plane elements, and the approach to obtain the membrane tension is not so straightforward as that of two-dimensional study.

* The results in this chapter have been accepted and will be published as "Sui, Y., Chew, Y. T., Roy, P. and Low, H. T., A hybrid method to study flow-induced deformation of three-dimensional capsules, J. Comput. Phys., 228: 6351-6371, 2008."

In this chapter, the IB-LBM with multi-block strategy of Chapter 2, is extended to three-dimensional simulation. The new idea incorporated is discretizing the three-dimensional capsule membrane into unstructured flat triangular elements, and incorporating a finite element model (Charrier et al., 1989; Shrivastava and Tang, 1993) into the multi-block IB-LBM to obtain the forces acting on the membrane nodes.

The present method is validated by studying the transient deformation of initially spherical and oblate spheroidal capsules with various membrane constitutive laws under shear flow. The versatility of the present method is demonstrated by studying the deformation of capsules with inertia effects, and the deformation of capsules with very complex shape like the biconcave discoid.

5.1. Membrane model

Three different membrane laws are tested. The three-dimensional capsule is discretized into flat triangular elements. The forces acting on the membrane nodes are obtained from a finite element model.

5.1.1 Membrane constitutive laws

In the present study, three different membrane constitutive laws are employed and tested. The capsule membranes are usually relatively thin, and thus the thickness can

be neglected. A simple constitutive equation is the neo-Hookean (NH) law, with strain energy function having the form:

$$W^{NH} = \frac{1}{6} E(I_1 - 1 + \frac{1}{I_2 + 1}) \tag{5.1}$$

where E is the surface shear elasticity modulus, and I_1 and I_2 are the first and second strain invariants, with $I_1 = \lambda_1^2 + \lambda_2^2 - 2, I_2 = (\lambda_1 \lambda_2)^2 - 1$. The term λ_1 and λ_2 are the principle strains, which are eigenvalues of the deformation tensor and represent the principle stretching ratios. The NH law corresponds to membranes made of polymerized material. The area dilation is unrestricted and is compensated by the thinning of the membrane.

The zero-thickness (ZT) shell equation is another version of the neo-Hookean (NH) law, which has been used by Ramanujan and Pozrikidis (1998):

$$W^{ZT} = \frac{1}{6} E[I_1 - \log(I_2 + 1) + \frac{1}{2} \log^2(I_2 + 1)] \tag{5.2}$$

The two strain energy functions (Equation 5.1 and 5.2) are equivalent for small deformation.

Another constitutive equation is the Skalak's law (SK) proposed by Skalak et al. (1973) to model the membrane of red blood cells:

$$W^{SK} = \frac{1}{4} E(\frac{1}{2} I_1^2 + I_1 - I_2) + \frac{1}{8} CEI_2^2 \tag{5.3}$$

In the right hand side of the equation, the first term represents the shear effects, and second term accounts for the area dilation. The term C is the ratio between shear elasticity modulus and area dilation modulus, which is quite large for incompressible biological membranes.

5.1.2 Membrane disretization

The three-dimensional capsule membrane is discretized into flat triangular elements. The triangulation procedure is similar to that of Ramanujan and Pozrikidis (1998). To discretize the unstressed interface, each triangular face of a regular octahedron is subdivided into 4^n triangular elements. These elements are then projected radically onto a sphere. The geometry of each element is described by its three vertices. The discretization of a sphere surface is shown in Figure 5.1(a). For oblate spheroid with aspect ratio *b/a*, the mapping system is stated as:

$$x_{obl} = Rx,\ y_{obl} = Ry,\ z_{obl} = (b/a)Rz \tag{5.4}$$

For the biconcave discoid, which is chosen to be the shape of red blood cell at rest, the mapping system is as follows:

$$x_{rbc} = Rx,\ y_{rbc} = Ry,\ z_{rbc} = 0.5R(1-r^2)^{0.5}(0.207 + 2.003r^2 - 1.123r^4) \tag{5.5}$$

where $r^2 = x^2 + z^2$, the term *R* in Equation 5.4 and 5.5 is the adjusting factor to keep the capsule volume constant. The discretization of a biconcave discoid surface is shown in Figure 5.1(b). Re-meshing is not needed during the computation, as the membrane is elastic and the elastic modulus will avoid the membrane points from being too far apart.

5.1.3 Finite element membrane model

A finite element membrane model is employed to obtain the forces acting at the discrete nodes of the membrane. In this section, only a brief description of this model is given. The detailed treatment can be found in Charrier et al. (1989) as well as Shrivastava and Tang (1993).

In the finite element model, the membrane of the capsule is represented by a patchwork of flat triangular elements which remain flat after deformation, and the load on an element is represented by concentrated loads on the membrane nodes. Only in-plane stresses and strains exist. In the three-dimensional deformation of the capsule, the membrane elements do not stay in the same plane after being displaced. In this model, the deformed element is transformed to the plane of the undeformed element, so that the relative displacement of the nodes and the corresponding forces are easily determined. The equations developed for the force exerted at the nodes of an element of the deformed membrane are given in the plane of the element.

The displacements are approximated by linear shape functions in the plane of the element with coordinates (x', y'). They are described by: $\chi(x', y') = ax' + by' + c$. The unknown coefficients a, b, and c are determined using known values of the displacements at the three nodes of the element. After the displacements of the three nodes of an element are known, its state of strain λ_1 and λ_2 can be obtained. The relation of membrane strain and membrane energy is governed by the constitutive law, which is determined by the membrane materials. With a constitutive law chosen, one can follow the usual finite element procedure and derive the relations between nodal forces and nodal displacements. The principle of virtual work is used to calculate the forces at the three nodes of an element, which are finally in the form of:

$$\{F_x\} = V_e \frac{\partial W}{\partial \lambda_1} \left\{ \frac{\partial \lambda_1}{\partial u} \right\} + V_e \frac{\partial W}{\partial \lambda_2} \left\{ \frac{\partial \lambda_2}{\partial u} \right\}$$

$$\{F_x\} = V_e \frac{\partial W}{\partial \lambda_1} \left\{ \frac{\partial \lambda_1}{\partial v} \right\} + V_e \frac{\partial W}{\partial \lambda_2} \left\{ \frac{\partial \lambda_2}{\partial v} \right\} \tag{5.6}$$

where $\{F_x\}$ and $\{F_y\}$ are the nodal forces in the x and y directions corresponding to the current deformed state of the membrane element, V_e is the original area of the element, and W is the strain energy density.

Because each node of the discrete membrane belongs to more than one element, the resultant force on a node is the sum of the forces exerted by the m elements attached to the node. So far, the force calculated is the fluid force acting on the capsule membrane. Its equal and opposite counterpart is the force acting on the fluid. It is distributed to the surrounding fluid by the approach described by the immersed boundary method.

5.2 Numerical Method

In the present hybrid approach, several methods are combined to simulate the flow-induced deformation of three-dimensional capsules. The immersed boundary concept is introduced into the framework of lattice Boltzmann method. The multi-block strategy is employed to refine the mesh near the capsule to increase the accuracy and efficiency of computation. The finite element membrane model, described in the previous section, is incorporated to obtain the membrane forces of the immersed boundary method.

5.2.1 The immersed boundary method

In the immersed boundary method of Peskin (1977, 2002), a force density is distributed to the Cartesian mesh in the vicinity of the moving boundary in order to

account for the effect of the boundary. The general idea of the immersed boundary method has been explained in detail in Chapter 2.

In this chapter of the three-dimensional computation, the non-slip boundary condition is satisfied by letting the flexible membrane move at the same velocity as the fluid around it. That is:

$$\frac{\partial \mathbf{X}(\mathbf{s},t)}{\partial t} = \mathbf{u}(\mathbf{X}(\mathbf{s},t),t) \tag{5.7}$$

This motion will cause the capsule to deform. The membrane force density **F**(**s**, t) is obtained from the finite element membrane model discussed in Section 5.1.3, and is distributed to the fluid mesh points near it by:

$$\mathbf{f}(\mathbf{x},t) = \int_{\Gamma} \mathbf{F}(\mathbf{s},t)\delta(\mathbf{x}-\mathbf{X}(\mathbf{s},t))d\mathbf{s} \tag{5.8}$$

where δ is a smoothed approximation of the Dirac Delta function. In the present three-dimensional study, it is chosen to be:

$$\delta(\mathbf{x}-\mathbf{X}(\mathbf{s},t)) = \delta(x-X(\mathbf{s},t))\delta(y-Y(\mathbf{s},t))\delta(z-Z(\mathbf{s},t)) \tag{5.9}$$

where

$$\delta(r) = \begin{cases} \frac{1}{4}(1+\cos(\frac{\pi|r|}{2})) & r \le 2 \\ 0 & r > 2 \end{cases} \tag{5.10}$$

The same approximation function is used to obtain the velocities of the Lagrangian nodes on the moving boundary. The mathematical form can be written as follows:

$$\frac{\partial \mathbf{X}}{\partial t} = \int_{\Omega} \mathbf{u}(\mathbf{x},t)\delta(\mathbf{x}-\mathbf{X}(\mathbf{s},t))d\mathbf{x} \tag{5.11}$$

5.2.2 The multi-block lattice Boltzmann method

In the lattice Boltzmann method, the D3Q19 model (see Figure 5.2) is one of the commonly used models in three-dimensional simulation, in which the discrete lattice Boltzmann equation has the form of:

$$f_i(\mathbf{x}+\mathbf{e}_i\Delta t, t+\Delta t) - f_i(\mathbf{x},t) = -\frac{1}{\tau}[f_i(\mathbf{x},t) - f_i^{eq}(\mathbf{x},t)] \tag{5.12}$$

where $f_i(\mathbf{x},t)$ is the distribution function for particles with velocity $\mathbf{e}_i$ at position $\mathbf{x}$ and time t, Δt is the lattice time interval, $f_i^{eq}(\mathbf{x},t)$ is the equilibrium distribution function and τ is the non-dimensional relaxation time.

In the D3Q19 model, the fluid particles have the possible discrete velocities stated as follows:

$$\begin{aligned}&[\mathbf{e}_0,\mathbf{e}_1,\mathbf{e}_2,\mathbf{e}_3,\mathbf{e}_4,\mathbf{e}_5,\mathbf{e}_6,\mathbf{e}_7,\mathbf{e}_8,\mathbf{e}_9,\mathbf{e}_{10},\mathbf{e}_{11},\mathbf{e}_{12},\mathbf{e}_{13},\mathbf{e}_{14},\mathbf{e}_{15},\mathbf{e}_{16},\mathbf{e}_{17},\mathbf{e}_{18}]\\ =&\begin{bmatrix} 0&1&-1&0&0&0&0&1&1&-1&-1&1&-1&1&-1&0&0&0&0\\ 0&0&0&1&-1&0&0&1&-1&1&-1&0&0&0&0&1&1&-1&-1\\ 0&0&0&0&0&1&-1&0&0&0&0&1&1&-1&-1&1&-1&1&-1 \end{bmatrix}\end{aligned} \tag{5.13}$$

The equilibrium distribution function $f_i^{eq}(\mathbf{x},t)$ is in the form of:

$$f_i^{eq} = E_i(\rho,\mathbf{u}) \tag{5.14}$$

$$\text{with } E_i(\rho,\mathbf{u}) = \omega_i\rho[1+\frac{\mathbf{e}\cdot\mathbf{u}}{c_s^2}+\frac{\mathbf{uu}:(\mathbf{e}_i\mathbf{e}_i - c_s^2\mathbf{I})}{2c_s^4}] \tag{5.15}$$

where ω_i is the weighing factor, it equals 1/3 for $i=0$, 1/18 for $i=1\sim6$ and 1/36 for $i=7\sim18$. The term c_s represents the sound speed, and equals $\Delta x/(\sqrt{3}\Delta t)$.

The relaxation time is related to the kinematic viscosity in Navier-Stokes equation in the form of:

$$\nu = (\tau - \frac{1}{2})c_s^2 \Delta t \tag{5.16}$$

Once the particle density distribution is known, the fluid density and momentum are calculated, using:

$$\rho = \sum_i f_i \ , \ \rho \mathbf{u} = \sum_i \mathbf{e}_i f_i \tag{5.17}$$

In this chapter, the multi-block lattice Boltzmann method proposed by Yu and Girimaji (2006) is employed. The computational domain is divided into blocks which are connected through the interface. On the interface between blocks, the exchange of variables follows a certain relation so that the mass and momentum are conserved and the stress is continuous across the interface.

Consider a two-block system to explain the idea of the multi-block method. The ratio of lattice space between the two blocks is defined as: $m = \Delta x_c / \Delta x_f$, where Δx_c and Δx_f are the lattice space of the coarse and fine mesh blocks respectively. For a given lattice space, the fluid viscosity can be obtained from Equation 5.16. In order to keep a constant viscosity, the relaxation parameter τ_f in fine mesh and τ_c in coarse mesh, must satisfy the following relation: $\tau_f = 0.5 + m(\tau_c - 0.5)$. The variables and their derivatives on the grid must be continues across the block interface. To keep this continuity, the relation of the density distribution function in the neighboring blocks is proposed as:

$$\tilde{f}_i^c = f_i^{eq,f} + m\frac{\tau_c - 1}{\tau_f - 1}[\tilde{f}_i^f - f_i^{eq,f}] \ , \ \tilde{f}_i^f = f_i^{eq,c} + \frac{\tau_f - 1}{m(\tau_c - 1)}[\tilde{f}_i^c - f_i^{eq,c}] \tag{5.18}$$

where $\tilde{f}_i$ is the post-collision density distribution function.

The typical structure of interface is illustrated in Figure 5.3. The fine block boundary MN, is in the interior of the coarse block. The coarse block boundary AB, is in the interior of the fine block. This arrangement is convenient for information exchange. Here, MN and AB represent planes projected onto the paper. On the boundary of fine block MN, there is no information on the grid points denoted by the solid symbol ● in Figure 5.3. It is obtained from spatial interpolation based on the information on the grid nodes denoted by the open symbol ○ on MN. The symmetric, 2D cubic spline spatial fitting of Yu and Girimaji (2006) is employed. Because the fluid particle has the same streaming velocity on each block, the computation marches *m* steps on the fine-mesh block for every one step on the coarse-mesh block. On the fine block boundary MN, temporal interpolation is needed to obtain $\widetilde{f}_{\alpha}(t^{n+1/m}, \mathrm{MN})$. The three-point Lagrangian formula of Yu and Girimaji (2006) is employed for temporal interpolation.

5.2.3 The hybrid method

In the present paper, the immersed boundary method is combined with the multi-block lattice Boltzmann method. The membrane forces of the immersed boundary method are obtained from the finite element membrane model. In order to solve the flow field with a force density the lattice Boltzmann equation must be modified. Several forms of LBE which can handle a force density have been proposed. Guo's approach (2001) is employed as it is accurate for unsteady flow with force changing with time and space, in which the modified lattice Boltzmann equation is in the form of:

$$f_i(\mathbf{x}+\mathbf{e}_i\Delta t, t+\Delta t) - f_i(\mathbf{x},t) = -\frac{1}{\tau}[f_i(\mathbf{x},t) - f_i^{eq}(\mathbf{x},t)] + \Delta t F_i \tag{5.19}$$

where $$f_i^{eq} = E_i(\rho, \mathbf{u}^*) \tag{5.20}$$

with $$\rho\mathbf{u}^* = \sum_i \mathbf{e}_i f_i + \frac{1}{2}\mathbf{f}\Delta t \tag{5.21}$$

$$F_i = (1-\frac{1}{2\tau})\omega_i[\frac{\mathbf{e}_i - \mathbf{u}}{c_s^2} + \frac{(\mathbf{e}_i \cdot \mathbf{u})}{c_s^4}\mathbf{e}_i]\cdot\mathbf{f} \tag{5.22}$$

In the computation in this chapter, a two-grid system is employed. The lattice space ratio between coarse and fine grids equals two. The capsules are immersed in the fine mesh block. The present procedure for multi-block computation is very similar to that proposed by Yu and Girimaji (2006). The only difference exists in the computation on the fine mesh block. That is, a subroutine implementing the immersed boundary method is added before the streaming and collision steps.

5.3. Results and Discussion

The present method is applied to simulate the deformation of spherical, oblate spheroidal and biconcave discoid capsules in simple shear flow. The capsules are unstressed at their initial shapes. The internal and external fluids have the same property. The dimensionless shear rate is defined as: $G = \mu k a / E$, where μ is the viscosity of the surrounding fluid, k is the shear rate, E is the shear elasticity of the membrane. The equivalent radius a is defined as: $a = (3V/4\pi)^{1/3}$, where V is capsule

volume. The Reynolds number in the present study is defined as: $\mathrm{Re} = \mu(ka)a/\rho$, where ρ is the density of the surrounding fluid.

5.3.1 Spherical capsules

5.3.1.1 Neo-Hookean membrane

To validate the present method, the transient deformation of spherical capsules in unbounded simple shear flow (illustrated in Figure 5.4) is studied. It has been well studied by Pozrikidis (1995) with ZT membrane law and Lac et al. (2004) with NH membrane law. In the present section, the capsule membrane follows NH law. The Reynolds number is at 0.025.

It is important to choose a computational domain which is large enough to neglect the boundary effect and has sufficient grid resolution to obtain convergent results. Numerical simulations are carried out under various computational domain sizes and grid resolutions. The temporal evolution of the capsule's Taylor shape parameter D_{xz} is chosen as the indicator. It is defined as: $D_{xz} = (L - B)/(L + B)$, where L and B are the semimajor and semiminor lengths of the capsule in the plane of shear (Lac et al., 2004). The dimensionless shear rate is chosen to be $G = 0.2$, at which the deformation is large.

The computational domain is a cubic box. The capsule is at the center of the domain, and its membrane is discretized into 8192 triangular elements connecting 4098 nodes. The fine mesh block covers a small cubic box, which has a side length of $4a$ and its center is coinciding with that of the computational domain. The other area is covered with coarse mesh. The grid resolutions in the fine and coarse blocks are

$\Delta x_f = \Delta y_f = a/12$ and $\Delta x_c = \Delta y_c = a/6$, respectively. The computational domains with outer boundary length of 8*a*, 10*a* and 12*a* are tested. The outer boundary condition is set to be the unperturbed simple shear flow. The temporal evolutions of Taylor shape parameter under various domain sizes at $G = 0.2$ are presented in Figure 5.5(a). It is shown that a cubic computational domain with side 10*a* is large enough to neglect the boundary effect.

Grid convergence study is carried out on the computational domain with side 10*a*. The diameter of the spherical capsule 2*a* was covered by 20, 24 or 32 lattice spaces of the fine mesh block. With the finest mesh, the capsule membrane is disretzed into 32768 flat triangular elements connecting 16386 nodes. The temporal evolutions of Taylor shape parameter under various grid resolutions at $G = 0.2$ is presented in Figure 5.5 (b). From the result it is seen that the grid resolution of $\Delta x_f = \Delta y_f = a/12$, with the capsule membrane discretized into 8192 triangular elements connecting 4098 nodes, is sufficient to capture the important characteristics. This computational domain and grid resolution are used in the simulations presented in this section and Section 5.3.2.

Another simulation is done for the same capsule and shear rate, using uniform mesh resolution of $\Delta x_f = \Delta y_f = a/12$ covering the whole computational domain, which is actually the original IB-LBM. It is seen that the temporal evolution of Taylor shape parameter curve (Figure 5.5b) nearly coincide with that of the present multi-block IB-LBM. In the present method, only 6.4% of the computational domain is covered with fine mesh, thus quite a lot of computational effort is saved.

The deformation of spherical capsules with the dimensionless shear rate G ranging from 0.0125 to 0.2 is studied. The results show that after being immersed in the flow, a capsule deforms to a steady shape and inclination; then the membrane rotates around the liquid inside (tank-treading motion). These observations are similar to those reported by Pozrikidis (1995) and Lac et al. (2004). For G = 0.0125, the steady deformed capsule and the flow field around the capsule's cross section in the plane of shear is presented in Figure 5.6. It is observed that the cross section of the capsule resembles a closed streamline which shows that the capsule has achieved a steady shape. Recirculating regions are found at two ends of the capsule. When comparing the flow pattern with that of 2D circular capsules, it is interesting to find that they are very similar, which shows that 2D study share some common features with the 3D study.

The temporal evolutions of the capsules' Taylor deformation parameter D_{xz} are presented in Figure 5.7 (a), and are compared with the results of Lac et al. (2004) who used the boundary element method. The present model has considered inertia, but due to the very small Reynolds number of 0.025, the inertia effect is negligible. Good quantitative agreements are observed. It is seen the time taken to achieve steady shape is shorter if the dimensionless shear rate is lower. A lower shear rate means the ratio between elastic and shear forces is larger, thus the capsule only needs to deform a little to generate enough elastic force to balance the viscous shear force. At small dimensionless shear rates, the steady Taylor shape parameter is compared with that predicted by Barthes-Biesel (1980) who used the second order small-deformation theory. For G = 0.0125 and 0.025, the agreement is satisfactory (Figure 5.7a). For G =

0.05, due to the relatively large deformation, the agreement is not good as the small deformation theory is not valid.

Figure 5.7(b) presents the temporal evolution of the capsule's inclination angle (with respect to x-axis). With the shear rate increasing, the capsules are observed to be more aligned with the flow. At low shear rates, the steady inclinations of the present simulation agree well with that predicted by Barthes-Biesel (1980) using second order small-deformation theory.

After the capsules have achieved steady shapes, their cross sections in x-z plane are presented in Figure 5.8. It is seen that at low shear rates, the capsules are slightly deformed and their cross sections are elliptical; at high shear rates, the cross sections of the deformed capsules are slender and sigmoidal.

5.3.1.2 Skalak membrane

As another validation of the present method, the transient deformation of spherical capsules with Skalak membrane in unbounded shear flow is studied. The moduli ratio C in Equation 5.3 is chosen to be 1 i. e. the same as that of Lac et al. (2004) who used the BEM. The Reynolds number in the present study equals 0.025. The computational domain and grid resolution are the same as that in the last section.

Similar to the results of previous Section 5.3.1.1, the capsule deforms to a steady shape and then the membrane carries out tank-treading motion. The temporal evolutions of the capsules' Taylor deformation parameter are presented in Figure 5.9 (a). The steady values are compared with the previous results reported by Lac et al. (2004) using boundary element method. Satisfactory agreements are observed with

the results of Lac et al. whose capillary number ε is related to the dimensionless shear rate G of the present study by: $\varepsilon = 2G$. Figure 5.9 (b) presents the temporal evolution of the capsule's inclination angle. However there is no previous result with SK membrane available for comparison. It is seen that with the shear rate increasing, the capsules are more aligned with the flow.

5.3.1.3 Spherical capsules with large inertia

To demonstrate the versatility of the present method, the deformation of capsules with inertia effects is studied. The linear shear flow past spherical capsules with neo-Hookean membranes is studied at Reynolds number ranging from 0.25 to 25. To our knowledge, the effect of inertia on the transient deformation of three-dimensional liquid-filled capsules with elastic membranes has not been explored so far.

The linear shear flow is generated by two solid walls moving in opposite directions. The computational domain is a cubic box with length $8a$, which is the distance between the two moving walls. The capsule is at the center of the domain. The boundary conditions at the upper and lower planes of the computational domain are set as solid walls moving in opposite directions. Periodic boundary conditions are employed on the other four boundary planes. For Re = 0.25 and 2.5, the fine mesh block covers from $2a$ to $6a$ in all axes. The grid resolutions in coarse and fine blocks and the disretization of the membrane are the same as those in the previous sections. For Re = 10 and 25, the fine mesh block covers from $1.5a$ to $6.5a$ in all axes, and the grid resolutions are: $\Delta x_c = \Delta y_c$ = a/8, $\Delta x_f = \Delta y_f$ = a/16. The membrane is discretized

into 32768 flat triangular elements connecting 16386 nodes. Grid convergence studies showed that the mesh resolutions are sufficient.

The temporal evolutions of the capsules' Taylor shape parameter and inclination angle are presented in Figure 5.10(a, b) for $G = 0.05$ and in Figure 5.11(a, b) for $G = 0.1$, with Reynolds number ranging from 0.025 to 25. At moderate Reynolds numbers, it is quite interesting to find that before the capsules achieve steady states, there is a transient process due to the inertia effect, especially apparent at higher Reynolds numbers. This phenomenon is quite different from that of capsule deformation in simple shear flow at vanishing Reynolds number, in which the capsules achieve steady states monotonically. In the transient period, the Taylor shape parameter and capsule inclination show dampened oscillations. Under the same dimensionless shear rates, the dimensionless transient period increase with increasing Reynolds number. Similar transient process, which is due to the effect of inertia, has been observed for two-dimensional capsules in simple shear flow in Chapter 4.

After the transient period, the capsules achieve steady configurations. Through comparison of the steady Taylor shape parameters at different Reynolds numbers, it is found that the inertia effect promotes the capsule deformation. It is also found that the curves for $Re = 0.25$ are comparable with that for $Re = 0.025$, which may suggest that the inertia effect on the capsule deformation is still very small up to $Re = 0.25$.

For all cases considered, the capsule achieves a steady state. The flow fields in the plane of shear around the cross sections of the capsules for $G = 0.1$ are plotted in Figure 5.12 for different Reynolds number from 0.25 to 25. It is seen that the cross sections of the capsules, which are represented by bold solid lines, resemble closed

streamlines. This shows that the capsules have achieved steady shapes. Through comparison of the flow field, it is found that inertia has significant effect. For example, the size of recirculating regions increases with the Reynolds number increasing. This is similar to that observed for two-dimensional capsules in Chapter 4.

It is also interesting to investigate steady three-dimensional configuration of the capsules at various Reynolds numbers. Figure 5.13 presents the steady profiles of capsules at Re = 0.25, 2.5, 10 and 25 at dimensionless shear rate G = 0.1. The corresponding cross-sections of the capsules can be found in the previous Figure 5.12. At small Re = 0.25, the capsule achieves an ellipsoidal shape. However at moderate Re = 25, the steady shape looks very different. It resembles a flat disk, with two ends of large curvature pointing upwards or downwards.

In general, it can be found that the results for three-dimensional capsules indicate an initial transient process, which is qualitatively similar to that of two-dimensional capsules (in chapter 4). Also, inertia significantly affects the steady shape of both two-dimensional and three-dimensional capsules. These may suggest that two-dimensional and three-dimensional capsules behave qualitatively similar under the effect of inertia.

5.3.2 Oblate spheroidal capsules

As a further validation of the present method, the transient deformation of oblate spheriodal capsules, with major to minor axes ratio of 10:9 and 2:1, in shear flow is studied. These cases are more challenging than those in the previous section because of the more complicated capsule shapes. In this section, the capsules membrane

follows zero-thickness law, same as that of Ramanujan and Pozrikidis (1998) who used BEM. The Reynolds number in the present study is at 0.025. The computational domain and grid resolution is this section is the same as that in the previous sections.

For a spherical capsule in shear flow, the capsule deforms and then the membrane performs tank treading around the liquid inside. During this tank treading motion, the shape and inclination of the capsule remains unchanged. The motion of oblate spheroidal capsules is different. It has been observed that after a transient stage, the capsule membrane rotates around the liquid inside; during this tank treading motion, the capsule undergoes periodical shape deformation and inclination oscillation. The results are similar to those predicted by Ramanujan and Pozrikidis (1998). For a capsule with major to minor axes ratio of 10:9 at G = 0.1, the snapshots of the capsule's cross section in the plane of shear during the unsteady tank treading motion are presented in Figure 5.14. It is seen that the capsule are changing shape and inclination while its membrane is rotating round the liquid inside.

The temporal evolutions of the capsules' Taylor deformation parameter and inclination angle are presented in Figure 5.15(a, b) for capsules with major to minor axes ratio of 10:9 at G = 0.1 and 0.2. The results of a more oblate capsule is presented in Figure 5.16(a, b), which are for capsules with major to minor axes ratio of 2:1 at G = 0.2. The results of Ramanujan and Pozrikidis (1998) are also presented in Figure 5.15(a) and Figure 5.16(a). Satisfactory agreements are observed.

5.3.3 Biconcave discoid capsules

For biconcave capsules, whose shape resembles that of red blood cells, it is expected that they will carry out tank treading motion in simple shear flow if the internal liquid is same as that outside and the shear rate is large (Ramanujan and Pozrikidis, 1998). However, due to the complex geometry of the capsule, numerical instabilities were encountered in previous computations, and the behaviour was followed for an initial short stage (Ramanujan and Pozrikidis, 1998; Eggleton and Popel, 1998). So far, the tank treading motion for three-dimensional biconcave capsules has not been fully recovered by numerical simulation.

To demonstrate the capacity of the present method, the deformation of capsules with biconcave shape is studied in simple shear flow in this section. The membrane of the capsule follows Skalak's law (Equation 5.3), in which the moduli ratio C is chosen to be 200 to take the membrane incompressibility into account. The computational domain is a cubic box with side length $10a$. The fine mesh block covers from $2a$ to $8a$ in all axes, and the grid resolutions are: $\Delta x_c = \Delta y_c = \Delta z_c = a/8$, $\Delta x_f = \Delta y_f = \Delta z_f = a/16$. The membrane is discretized into 32768 flat triangular elements connecting 16386 nodes, which is sufficient to capture the important characteristics.

Simulations are carried out for the deformation of capsules at G = 0.6, 0.9 and 1.2, with Re = 0.25. The tank treading motion (the membrane rotates around the liquid inside) is observed. Similar to that of oblate spheroidal capsules, during this tank treading motion, the capsule undergoes periodic shape deformation and inclination oscillation. This unsteady tank-treading motion had been expected by Ramanujan and

Pozrikidis (1998) in their study in which the motion was followed for an initial short stage.

The temporal evolution of the capsules' inclination angle is presented in Figure 5.17. To illustrate the capsules' shape evolution during this unsteady tank-treading motion, the snapshots of the capsule' profiles at $G = 0.9$ are presently in Figure 5.18 at sequential dimensionless times. The legends at the lower right of the figures represent the cross sections of the capsule in the plane of shear. The diamond symbol represents the same membrane node which is moving. It is seen from Figure 5.18 that during the membrane rotating around the liquid inside, the capsule is changing its shape and inclination. It is interesting to find that when the capsule is most elongated, its width (in y direction) is smallest, and vice visa. This phenomenon can also be observed from Figure 5.19, in which the temporal evolution of the capsule's length and width is presented. The simulation is stopped after the capsule membrane has been rotating for a whole period. For all cases in this section, the membrane area change is within 1% and the capsule volume change is within 0.2% during the computation.

5.4 Concluding remarks

A hybrid method is proposed to study the flow-induced deformation of three-dimensional, liquid-filled capsules with elastic membranes. In the present approach, the immersed boundary concept is incorporated into the lattice Boltzmann method, the multi-block strategy is employed to refine the mesh near the capsule, and a finite

element model is incorporated to obtain the forces acting on the membrane nodes of the three-dimensional capsule which is discretized into flat triangular elements. The present method was validated by studying the transient deformation of initially spherical and oblate spheroidal capsules with various membrane laws under shear flow. The present results agree well with published theoretical or numerical results. Compared with the original immersed boundary-lattice Boltzmann method, the present method is much more efficient. The present method is capable to take the inertia effect into account. This was demonstrated by studying the deformation of spherical capsules in shear flow at moderate Reynolds numbers, which has not be investigated so far. It was found that inertia has significant effects on the transient deforming process and steady configurations of capsules, as well as on the flow field. The transient deformation of capsules with initially biconcave disk shape was also simulated. The unsteady tank treading motion was followed for a whole period in the present work. Due to numerical instabilities encountered in previous computations, this motion has not been fully recovered by numerical simulation so far.

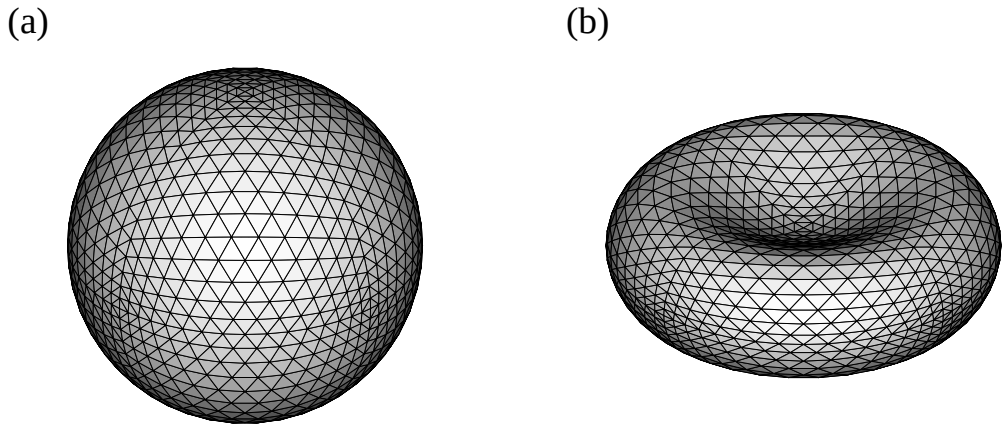

Figure 5.1 Discretization of (a) a sphere; (b) a biconcave disk shape

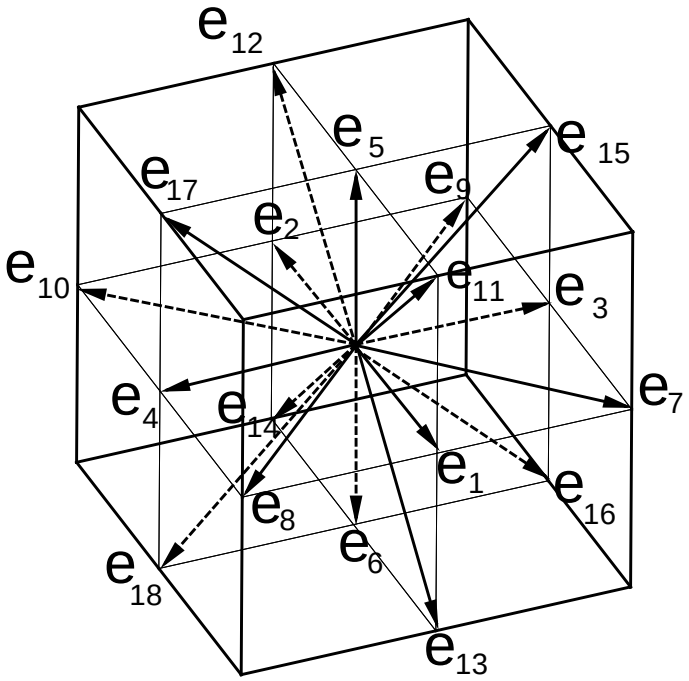

Figure 5.2 D3Q19 model

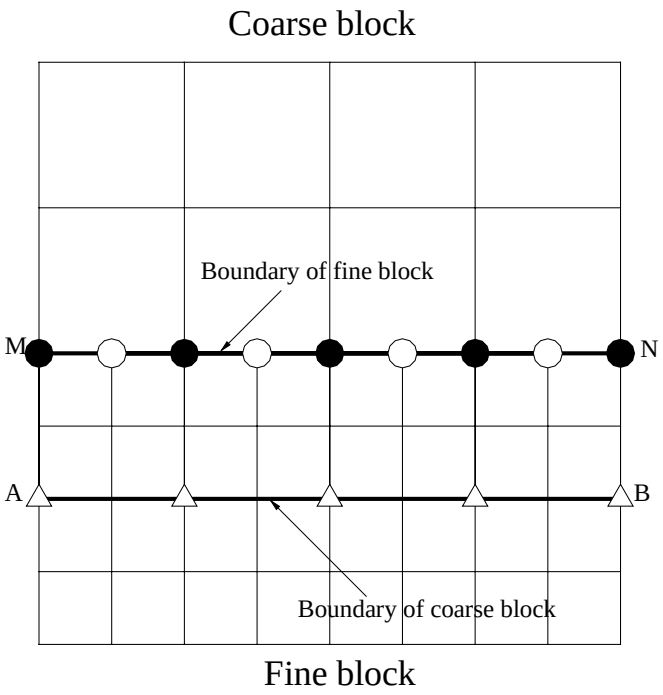

Figure 5.3 Interface structures between two blocks

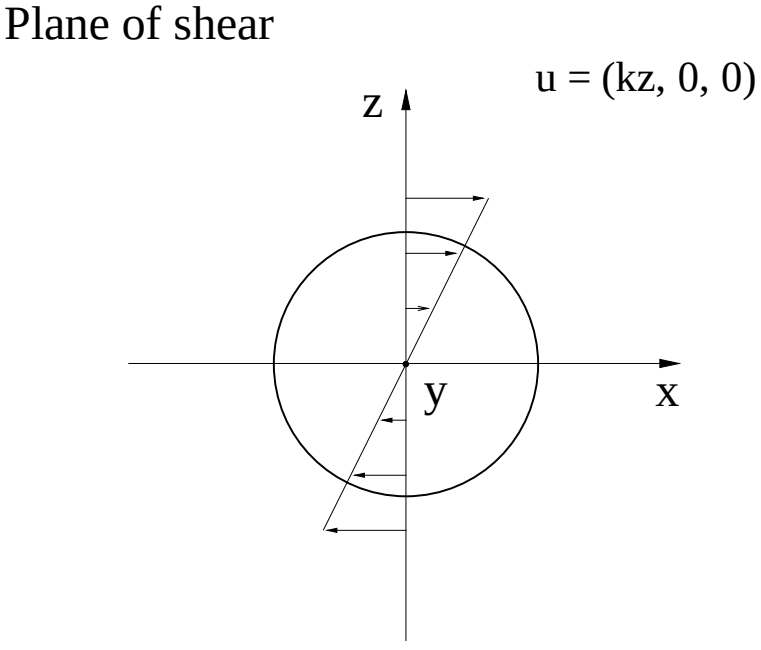

Figure 5.4 Illustration of a capsule in simple shear flow

(a)

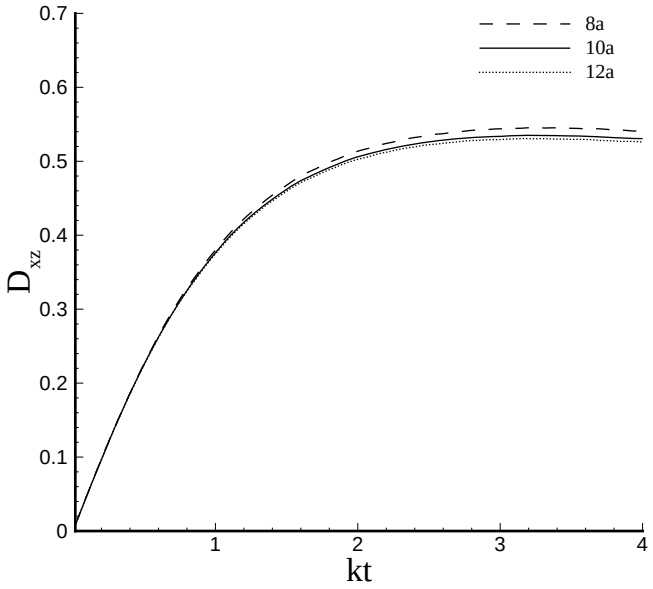

(b)

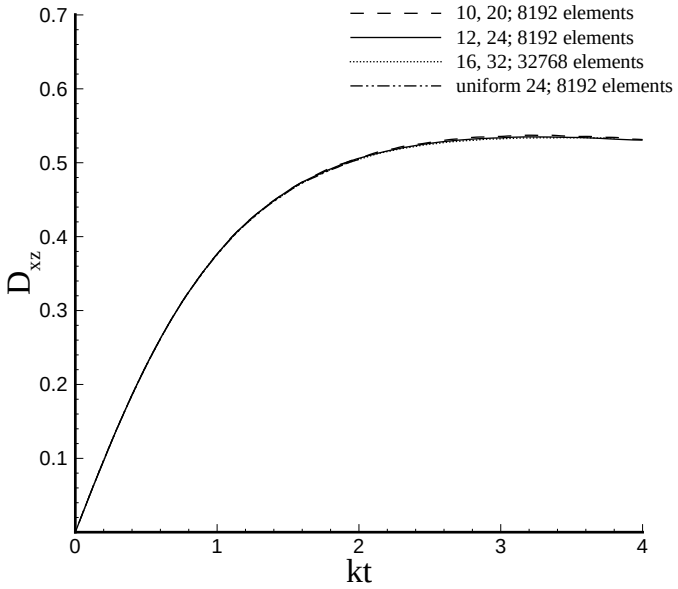

Figure 5.5 Temporal evolution of the capsule's Taylor shape parameter at $G = 0.2$ under various (a) computational domain sizes; (b) grid resolutions

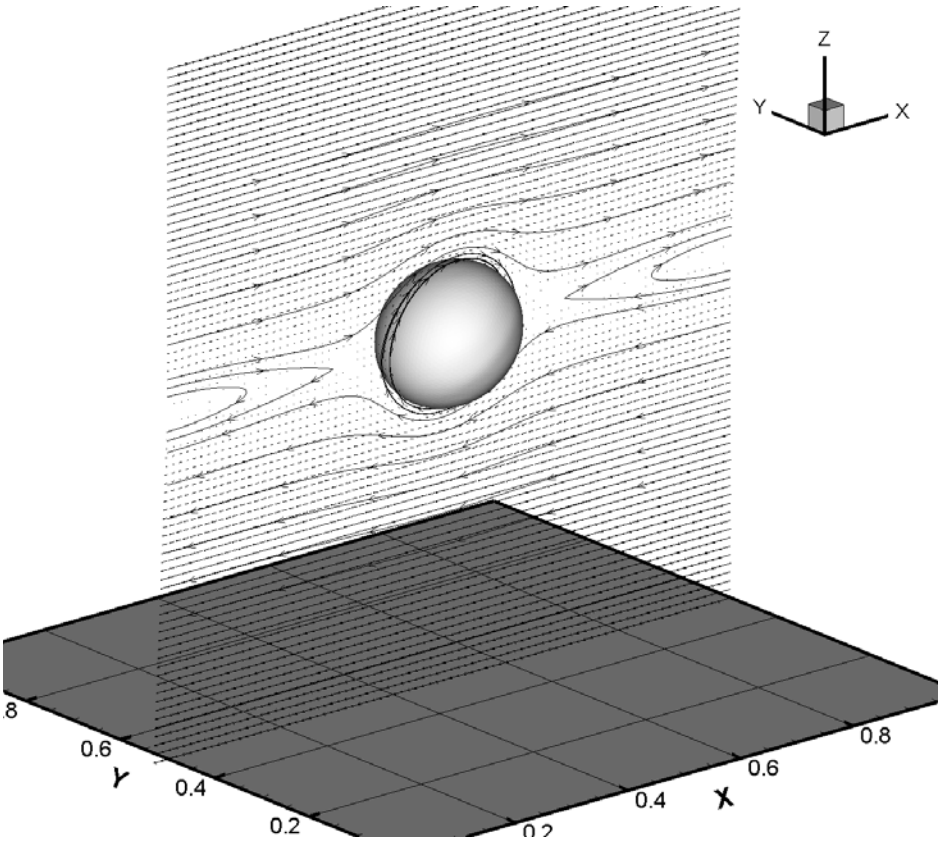

Figure 5.6 Steady deformed capsule and the flow field around the cross section of the capsule in the plane of shear (*x*-*z* plane)

(a)

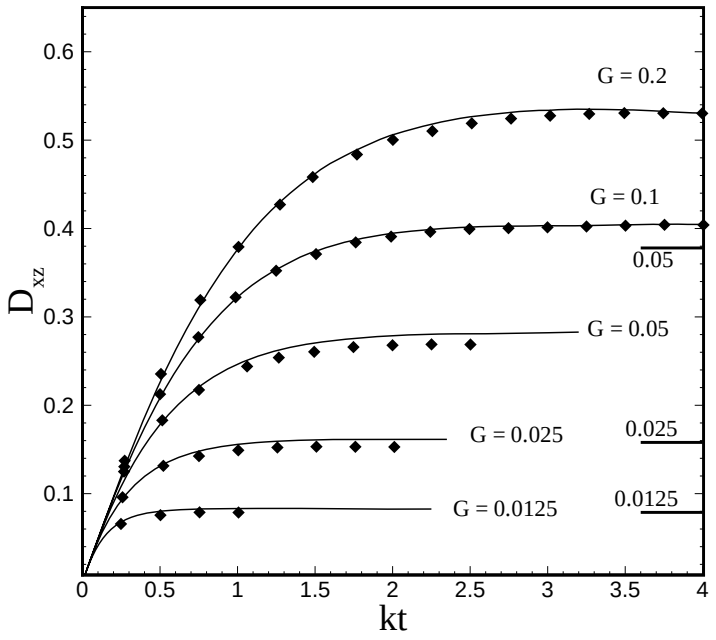

(b)

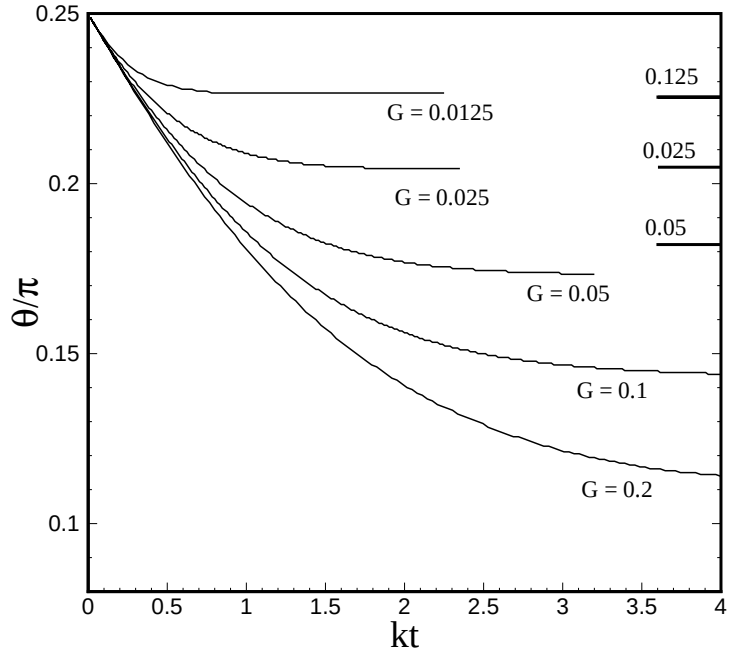

Figure 5.7 Temporal evolution of (a) Taylor shape parameter; (b) inclination angle of the initially spherical capsules with NH membranes. The symbols ♦ represent the results of Lac et al. (2004) with the boundary element method. The straight horizontal bold line represents the predictions of the second order small-deformation theory of Barthès-Biesel (1980) for $G = 0.0125, 0.025, 0.05$

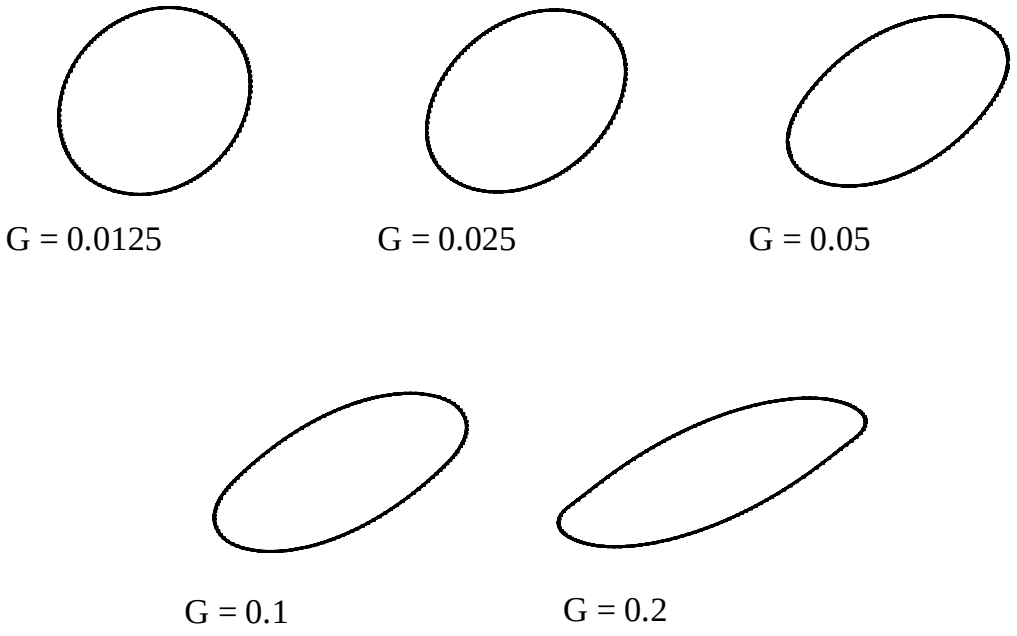

Figure 5.8 Cross sections of the steady formed capsules in the plane of shear

(a)

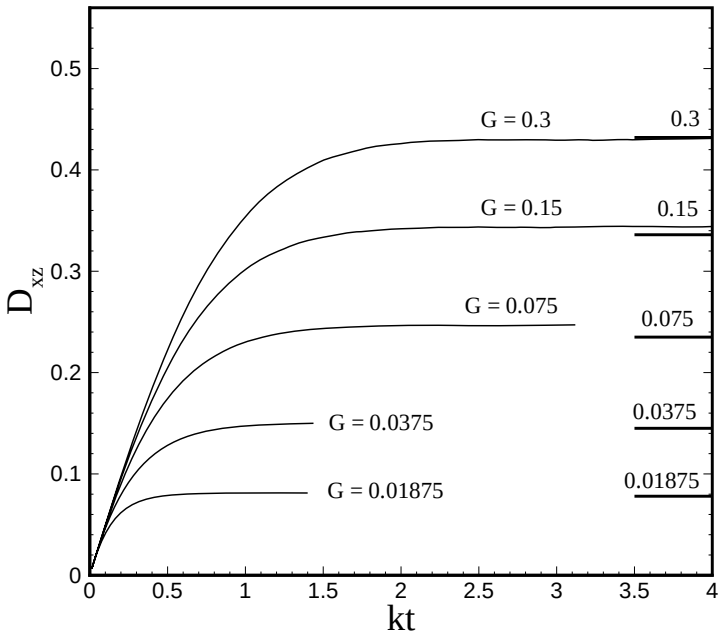

(b)

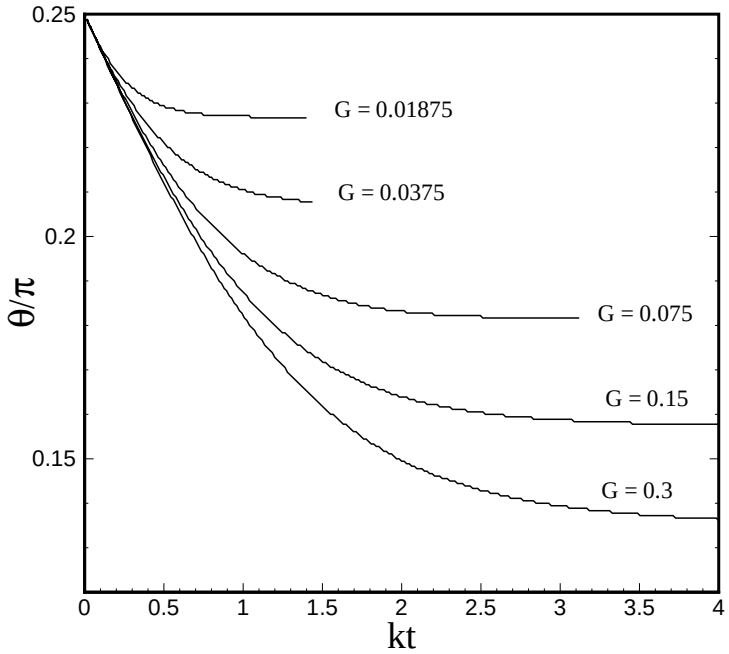

Figure 5.9 Temporal evolution of (a) Taylor shape parameter; (b) inclination angle of the initially spherical capsules with SK membranes. The straight horizontal bold line represents results of Lac et al. (2004)

(a)

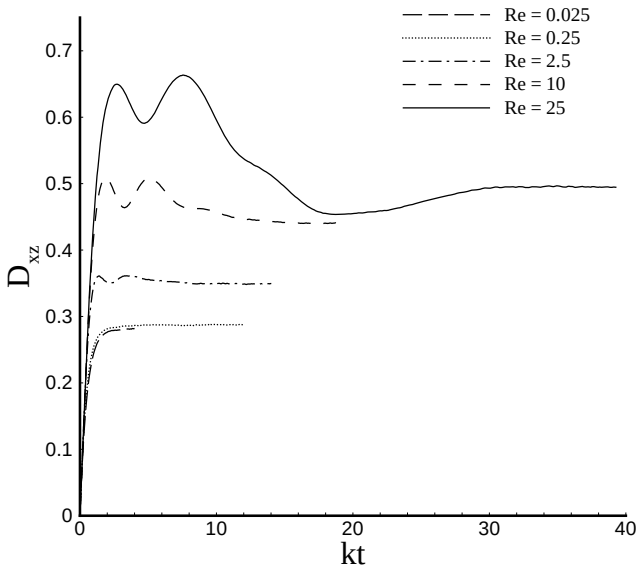

(b)

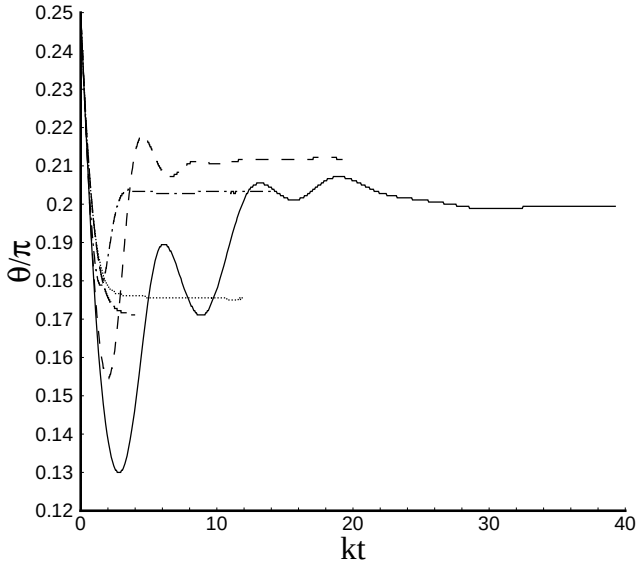

Figure 5.10 Temporal evolution of (a) Taylor shape parameter; (b) inclination angle of spherical capsules with NH membrane at G = 0.05 under various Reynolds numbers

(a)

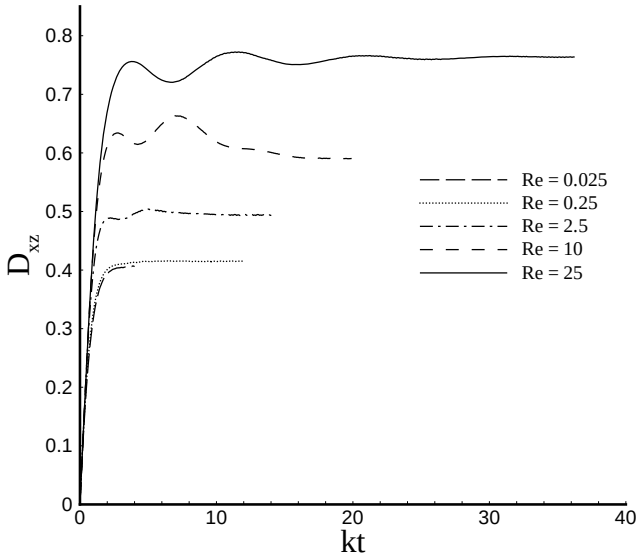

(b)

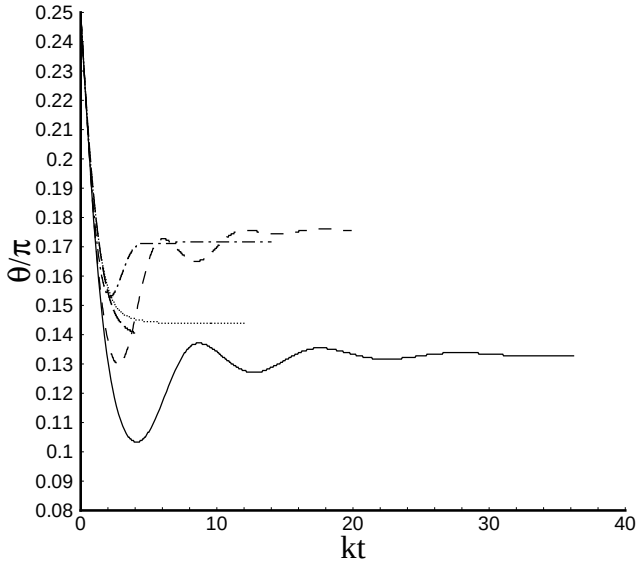

Figure 5.11 Temporal evolution of (a) Taylor shape parameter; (b) inclination angle of spherical capsules with NH membrane at G = 0.1 under various Reynolds numbers

(a)

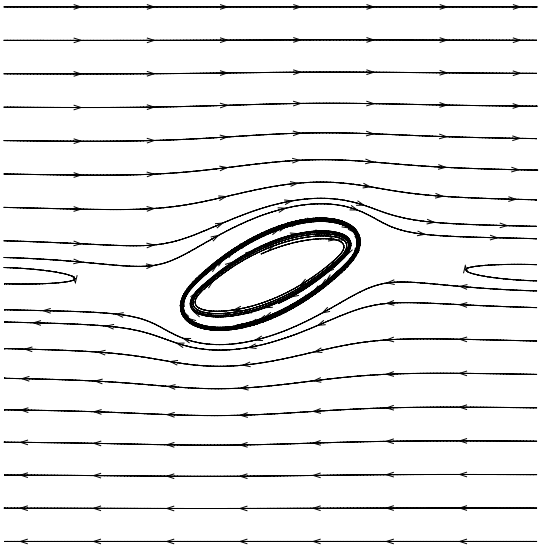

(b)

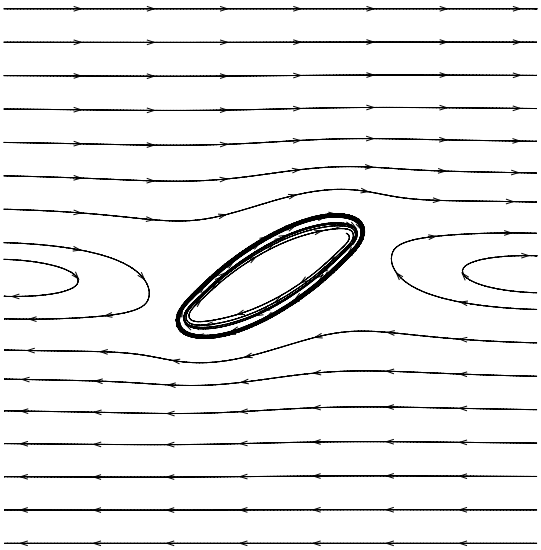

(c)

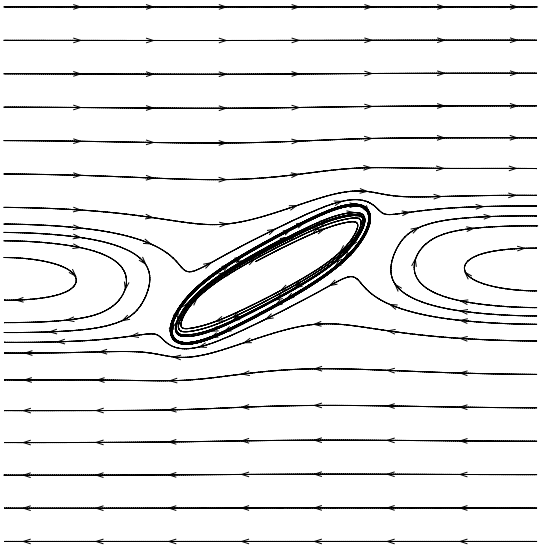

(d)

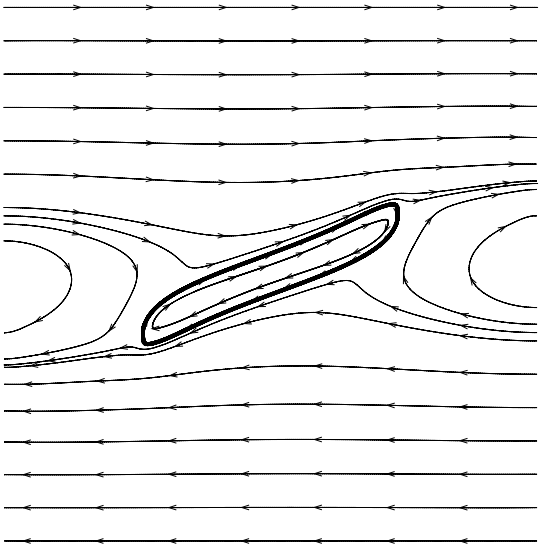

Figure 5.12 Flow fields in the plane of shear (*x*-*z* plane) around the cross sections of the capsules for G = 0.1 at Re = (a) 0.25; (b) 2.5; (c) 10 and (d) 25

(a)

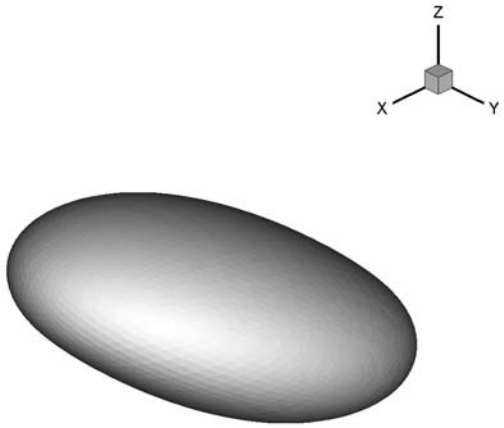

(b)

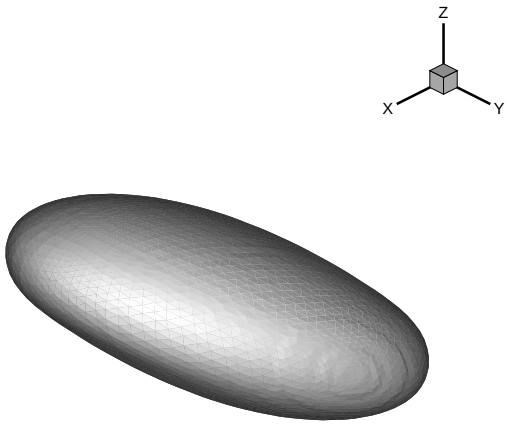

(c)

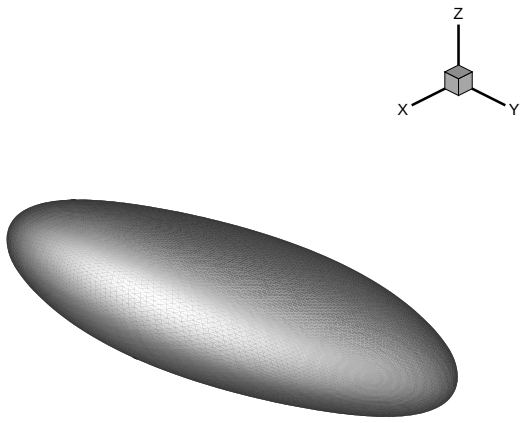

(d)

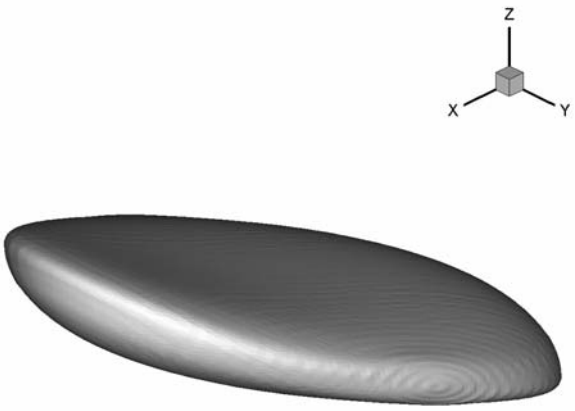

Figure 5.13 Three-dimensional steady profiles of the capsules at Re = (a) 0.25; (b) 2.5; (c) 10; (d) 25

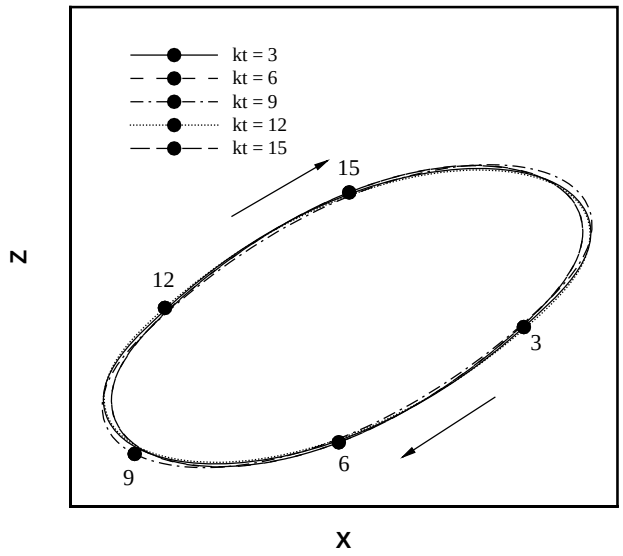

Figure 5.14 Snapshots of an initially oblate spheroidal capsule's cross section in the plane of shear during the tank treading motion. The symbol ● represents the same membrane node which is moving

(a)

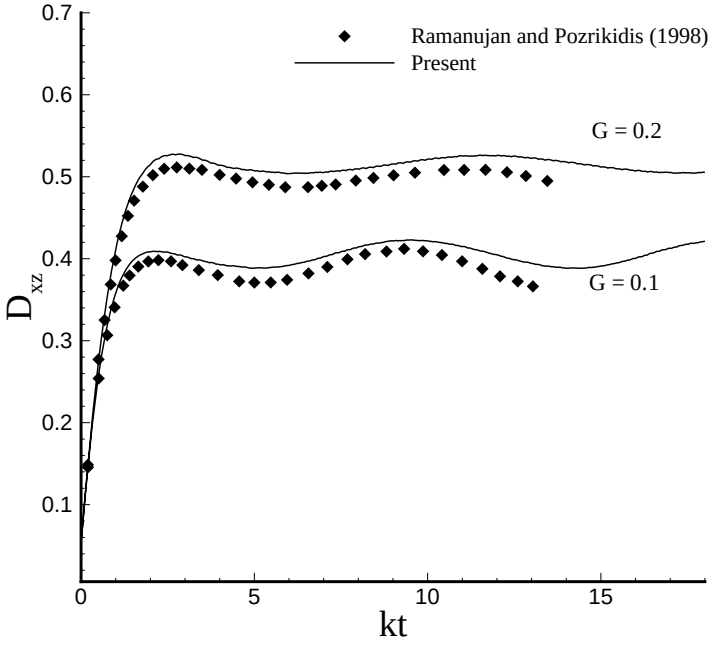

(b)

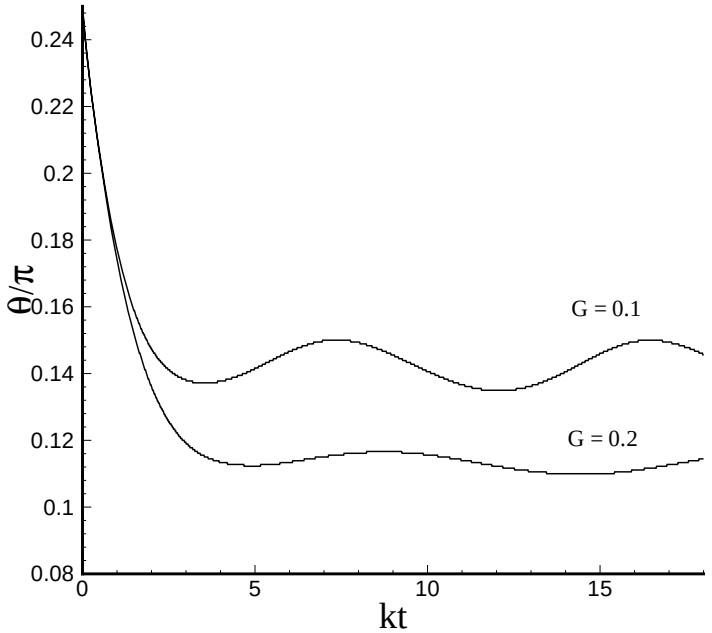

Figure 5.15 Temporal evolution of (a) Taylor shape parameter; (b) inclination angle of oblate spheroidal capsules with semimajor to semiminor axes ratio of 10:9

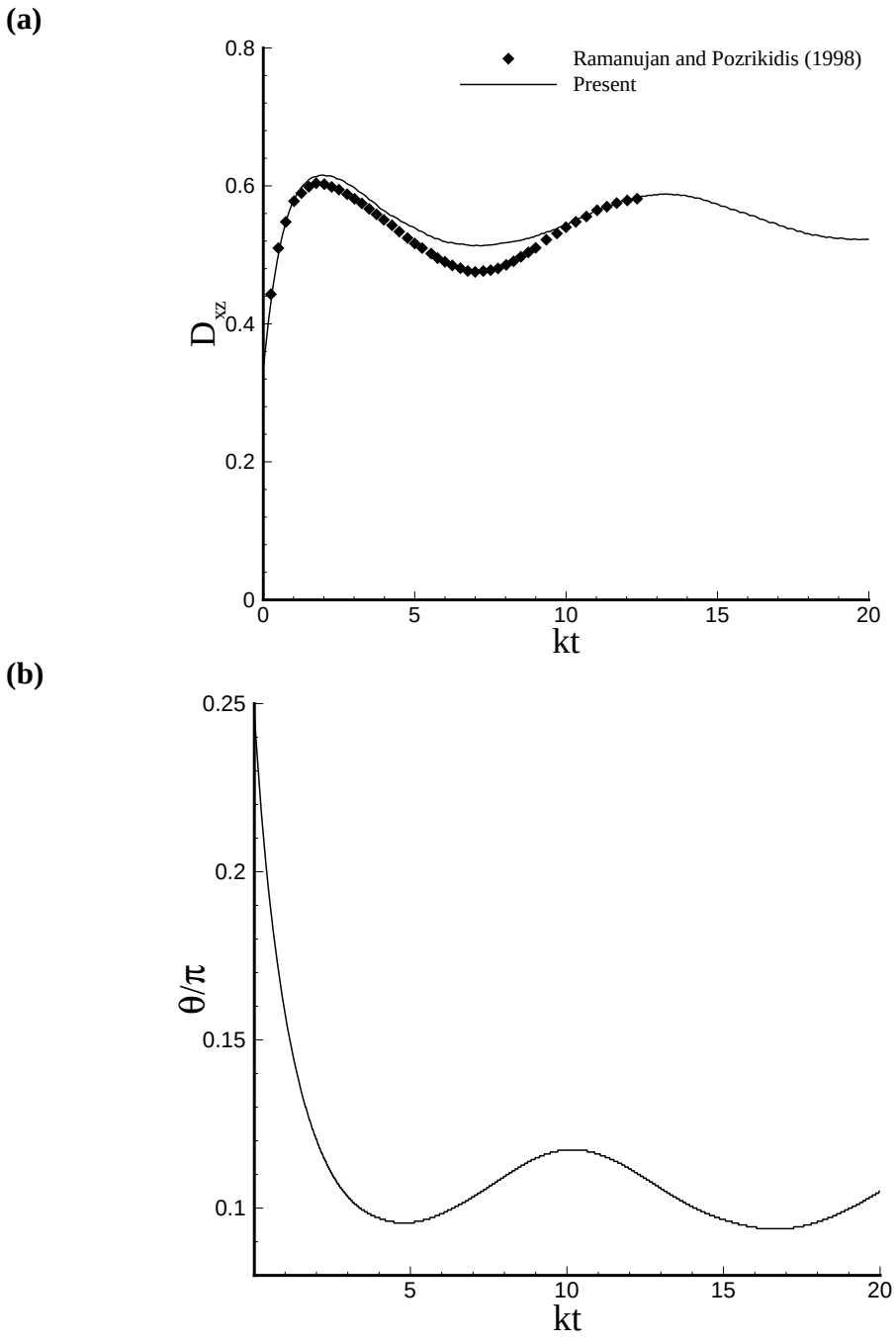

Figure 5.16 Temporal evolution of (a) Taylor shape parameter; (b) inclination angle of oblate spheroidal capsules with semimajor to semiminor axes ratio of 2:1

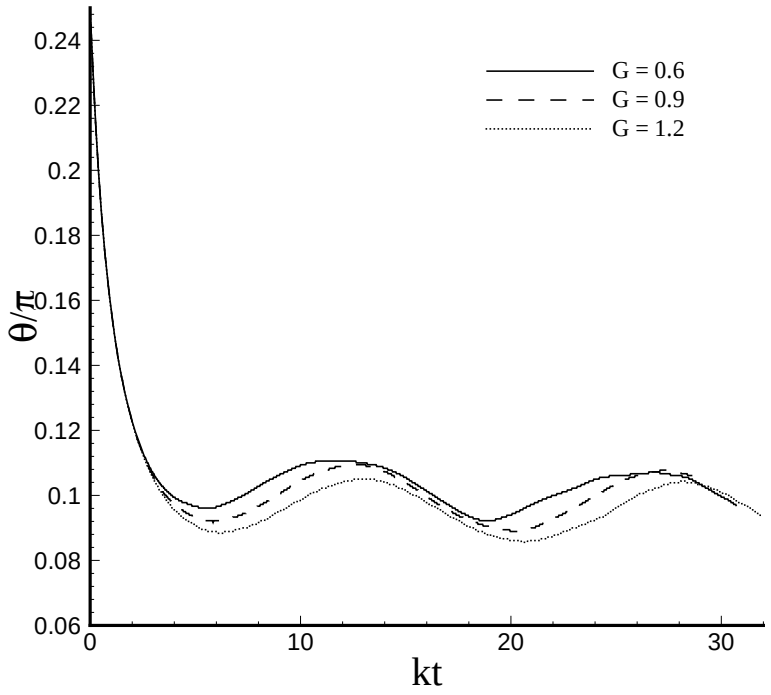

Figure 5.17 Temporal evolution of the inclination angle of the initially biconcave capsule

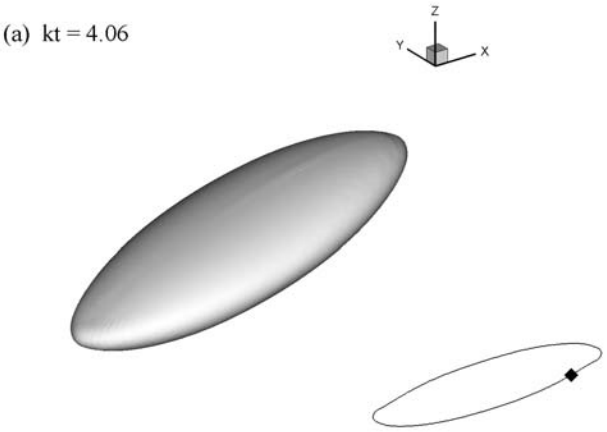
(a) kt = 4.06
Z
Y
X

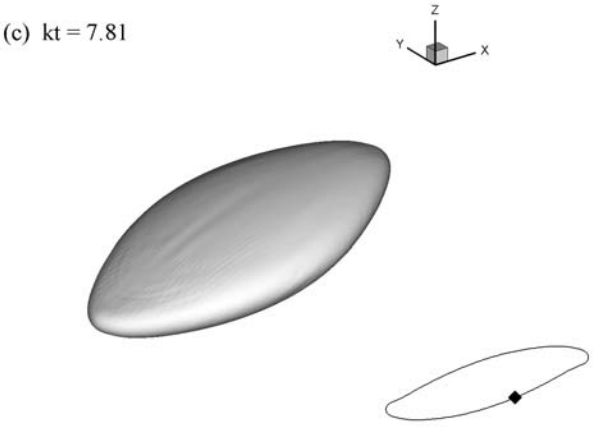
(c) kt = 7.81
Z
Y
X

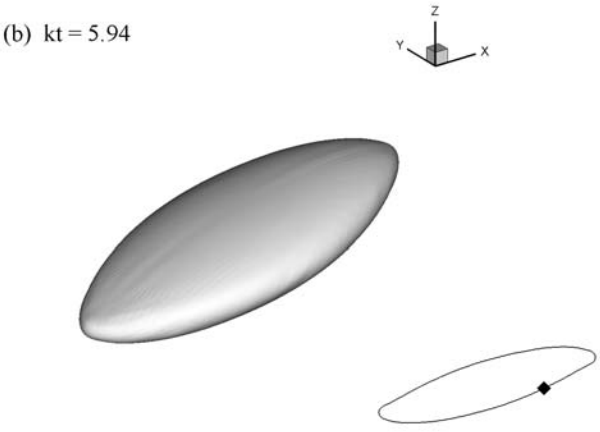
(b) kt = 5.94
Z
Y
X

(d) kt = 9.69

(e) kt = 11.56

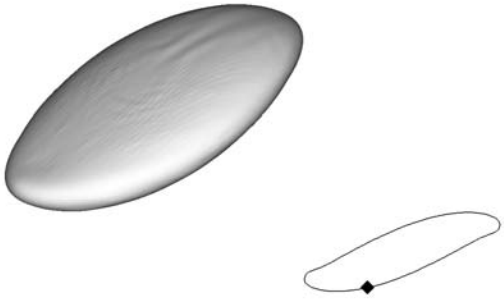

(f) kt = 13.44

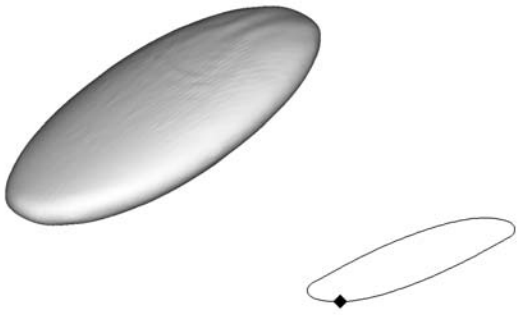

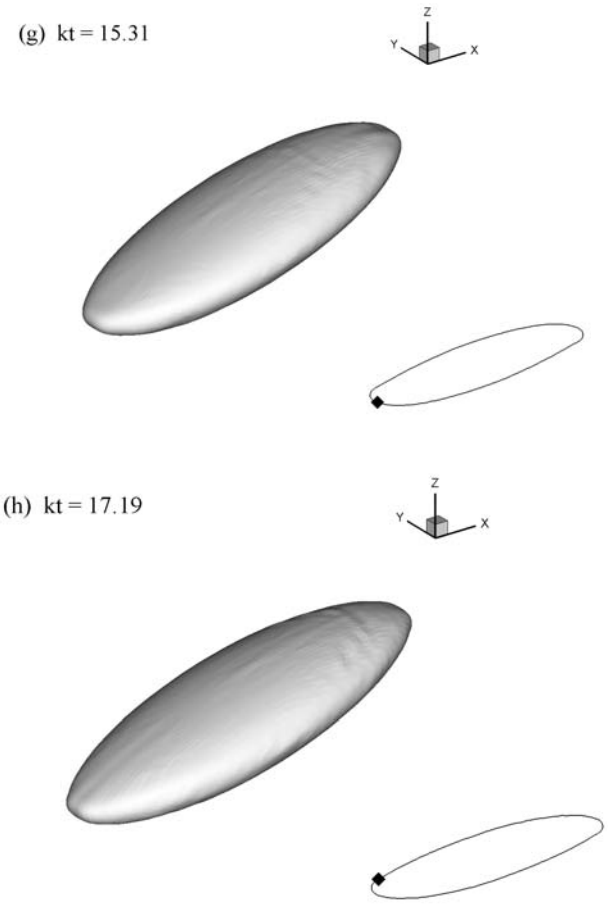

Figure 5.18 Snapshots of the capsule during the tank-treading motion. The diamond symbol represents the same membrane node on the capsule's cross section in the plane of shear

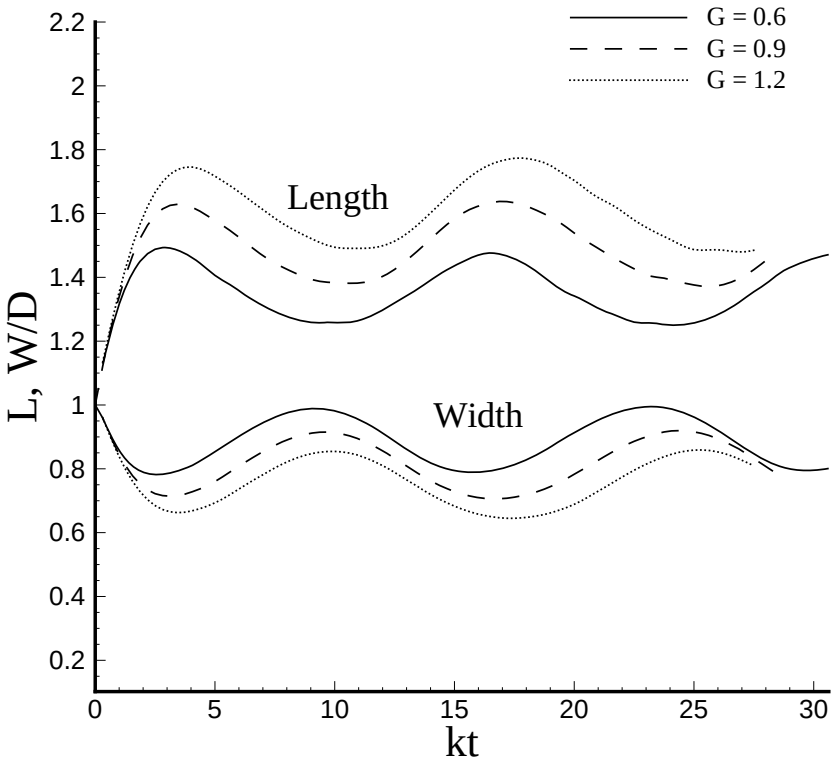

Figure 5.19 Temporal evolution of the capsule's length and width

Chapter 6 A Shear Rate Induced Swinging-to-Tumbling Transition of Three-dimensional Elastic Capsules in Shear Flow*

In Chapter 5, a hybrid method was proposed to study the flow-induced deformation of three-dimensional capsules. The method was validated by studying capsules with various initial shapes and membrane models. In this chapter, the dynamic motion of three-dimensional capsules in shear flow is studied, with an emphasis on investigating the relation between shear rate and the capsule's motion mode.

It has been long recognized that in shear flow, capsules immersed in a low viscosity fluid tumble continuously, and capsules immersed in a fluid with sufficiently high viscosity carry out tank-treading motion. In order to study the physics involved, Keller and Skalak (1982) theoretically analyzed the deformation of an ellipsoidal capsule in simple shear flow. It was found that for a capsule with a given geometry, the transition from tank-treading mode to tumbling mode depends on the viscosity ratio between internal fluid and external fluid, and it was independent of shear rate.

Only recently, Walter et al. (2001) studied synthetic microcapsules in shear flow experimentally. It was found that during the tank-treading motion of the membrane,

* The results of this chapter have been published as "Sui, Y., Low, H. T., Chew, Y. T. and Roy, P., Tank-treading, swinging and tumbling of liquid-filled elastic capsules in shear flow, Phys. Rev. E, 77: 016310, 2008."

the capsule undergoes periodic shape deformation and inclination oscillation; the inclination oscillation amplitude increases as the shear rate decreases. Similar motion has also been found for red blood cells in shear flow (Abkarian et al. 2007): the cells present an oscillation of their inclination superimposed to the tank-treading motion, and the tank-treading-to-tumbling transition can be triggered by decreasing the shear rate. These novel experimental findings show that in shear flow, the mode transition of these capsules depends not only on viscosity ratio, but also on shear rate. This contradicts the well-known theory of Keller and Skalak (1982). To our knowledge, for three-dimensional liquid-filled capsules with elastic membrane, the shear-rate induced transition of capsules' motion has not been reported in studies which take into account the deformation of the capsules.

In this chapter, the dynamic motion of three-dimensional capsules in shear flow is investigated by direct numerical simulation. The capsules are modeled as enclosed elastic membranes filled with Newtonian liquid same as that outside. The capsule membrane is assumed to be infinitely thin and the bending stiffness is neglected. The dynamic motion of initially spherical, oblate spheroidal and biconcave discoid capsules with various membrane constitutive laws is considered. The present numerical study is based on the hybrid method, which has been described in detail and well calibrated in Chapter 5.

6.1. Initially spherical capsules

The transient deformation of initially spherical capsules in unbounded simple shear flow is studied, under various dimensionless shear rates. The capsules are unstressed at their initial shape. Due to the small length scale of the capsule, the Reynolds number is at the order of 0.1, and the inertia effect can be neglected. The dimensionless shear rate plays an essential role in determining the capsule deformation. It is defined as: $G = \mu k a / E$, where the term μ is the viscosity of the surrounding fluid, k is the shear rate, E is the shear elasticity of the membrane. The term a is the equivalent radius, in the form of: $a = (3V / 4\pi)^{1/3}$, where the term V is capsule volume.

In the present simulation, the computational domain is a cubic box with side-length $10a$. Numerical experiment shows that it is large enough to neglect the boundary effect. The capsule is at the center of the domain, and its membrane is discretized into 8192 flat triangular elements connecting 4098 membrane nodes. The fine mesh block covered from $3a$ to $7a$ in all axes. The other domain was covered with coarse mesh. The grid resolutions in fine and coarse block were $\Delta x_f = \Delta y_f = \Delta z_f = a/12$ and $\Delta x_c = \Delta y_c = \Delta z_c = a/6$, respectively. Grid-independent study (in chapter 5) showed that this mesh density was sufficient.

First studied is the deformation of initially spherical capsules with ZT membrane (given by Equation 5.2). The dimensionless shear rate G ranges from 0.0125 to 0.2. The present results show that after immersed in the flow, a capsule deforms to a steady profile, and then the membrane rotates around the liquid inside (steady tank-

treading motion). These are similar to the results reported by Ramanujan and Pozrikidis (1998) and Lac et al. (2004). For G = 0.05, the steady deformed capsule and the flow field around the capsule's cross section in the plane of shear are presented in Figure 6.1. It is observed that the cross section of the capsule resembles a closed streamline. Recirculating regions are found at two ends of the capsule.

The deformation of the capsule is measured by the Taylor deformation parameter D_{xz} , which is defined as $D_{xz} = (L - B)/(L + B)$, where L and B are the length and width of the capsule in the plane of shear. The temporal evolutions of the capsules' Taylor deformation parameter are presented in Figure 6.2(a). It is seen that the time taken to achieve steady shape is shorter if the dimensionless shear rate is lower. A lower shear rate means the ratio between elastic and shear forces is larger, thus the capsule only needs to deform a little to generate enough elastic force to balance the viscous shear force. The present results were compared with that of Ramanujan and Pozrikidis (1998), in which the same case was studied with the boundary element method. The differences of the results are within 5%, which further validated the present numerical model. Figure 6.2(b) presents the temporal evolutions of the capsules' inclination angle (with respect to x-axis) in the plane of shear. With the shear rate increasing, the capsules are observed to be more aligned with the flow.

The ZT law corresponds to membranes made of polymerized material. The area dilation is unrestricted. For above cases, the maximum membrane area change ranges from 0.4% for G = 0.0125 to 23.5% for G = 0.2. The membranes of biological cells are usually incompressible; for example red blood cells, which membrane follows SK law (given in Equation 5.3). The deformation of initially spherical capsules with SK

membrane is studied. The moduli ratio C is chosen to be 100 in order to take the membrane-area incompressibility into account. For capsules with SK membrane, the steady configuration of the capsule and the time taken to achieve a steady shape depends not only on the dimensionless shear rate, but also on the moduli ratio. A small dimensionless shear rate or a large moduli ratio will restrict the capsule deformation and shorten the time it takes to achieve a steady shape. The temporal evolutions of the capsules' Taylor deformation parameter D_{xz} and the inclination angle are presented in Figure 6.3. From the results, it is seen that the overall behavior of the capsules is qualitatively similar to that of capsules with ZT membrane. The steady tank-treading mode of the capsule is achieved after an initial transient stage. The membrane area changes for capsules with SK membrane are much smaller than those with ZT membrane. At $G = 0.3$, the membrane area change is within 1.8%.

From above results and discussion, it is found that for the spherical capsule in shear flow, it will always achieve a steady tank-treading motion after an initial transient stage.

6.2. Initially oblate spheroidal capsules

Perfectly spherical capsules are hardly encountered in practice. In this section, the deformation of oblate spheroidal capsules, with aspect ratios of 10:9, 3:2 and 2:1, is studied in unbounded shear flow under various dimensionless shear rates. The

computational domain, block system and grid resolutions are the same as that in Section 6.1.

6.2.1. Swinging motion

First studied is the motion of capsules with ZT membrane. From the results, it is observed that at large shear rates, the capsules undergo an unsteady "swinging" motion, in which while the capsules' membranes are rotating around the liquid inside, the capsules undergo periodic shape deformation and inclination oscillation. For a capsule with aspect ratio of 3:2 at $G = 0.2$, its snapshots of the cross section (in the plane of shear) during the swinging motion are presented in Figure 6.4(a). The snapshots of the capsule's 3D profiles are presented in Figure 6.5, which gives a clearer illustration of the swinging motion.

The cross sections of the same capsule at $G = 0.05$ during the swinging motion are presented in Figure 6.4(b). It is seen from the results that the deformation of the capsule is smaller compared with that at $G = 0.2$, however, the inclination oscillation amplitude becomes larger. In the experiment of Walter et al. (2001), the dynamic motion of synthetic microcapsules with polymerized membrane was studied under shear flow conditions. It was found that the capsules undergo a similar swinging motion at large shear rates. It was also observed that as the shear rate decreases, the capsules' inclination oscillation amplitude increases. It is exciting that the present results qualitatively agree with experimental observations. In the experimental study, the matrix fluid is much more viscous than the liquid inside the capsule. However, the same case can not be studied by the current method, which can only consider capsules with the internal fluid viscosity same as that outside.

6.2.2. Swinging-to-tumbling transition

With the shear rate further decreased to G = 0.0125, the snapshots of the same capsule's cross sections are presented in Figure 6.4(c). It is quite interesting to find that the capsule's motion has changed from swinging to tumbling.

To give a more quantitative description of the capsules' motion, the temporal evolutions of the capsule's Taylor shape parameter and inclination angle in the plane of shear are presented in Figure 6.6. It is seen that the evolution curves undergo oscillations. The oscillation amplitudes of the Taylor shape parameter and inclination angle under different shear rates are presented in Figure 6.7. It is found from the results that within the swinging region, the oscillation amplitudes increase with the shear rate decreasing. The mode transition happens between G = 0.025 and G = 0.0125, below which the oscillation amplitude the inclination angle equals π, which indicates than the capsule is tumbling.

The dynamic motion of oblate spheroidal capsules, with aspect ratios of 10:9 and 2:1, is also studied under various dimensionless shear rates. The temporal evolutions of the capsules' inclination angle in the plane of shear are presented in Figure 6.8. From the results, it is seen that the behavior of the capsules are similar to that of the capsule with aspect ratio of 3:2. With the shear rate decreasing, the capsules' inclination oscillation amplitude increases, and finally triggers the transition from swinging to tumbling.

It must be noted that the deformation of oblate spheroidal capsules with NH membrane has been studied by Ramanujan and Pozrikidis (1998) with boundary element method. All shear rates considered in their study falls into the swinging

region. Within this region, the present results are comparable to those of Ramanujan and Pozrikidis.

In the recent experiment of Abkarian et al. (2007) on red blood cells in shear flow, it is observed that the cells present an oscillation of their inclination superimposed to the tank-treading motion, and tank-treading-to-tumbling transition can be triggered by decreasing the shear rate. These novel findings can not be covered by the well-known theory of Keller and Skalak (1982), in which the capsule is assumed to have a fixed ellipsoidal shape with moving membrane. The present study is the first direct numerical simulation which predicts the shear rate induced transition.

It is well known that the membrane of red blood cells is strongly resistant to membrane area dilation. Here, the oblate spheroidal capsules with SK membrane and moduli ratio C = 100, are employed as a simplified model of the red blood cells. The dynamic motion of capsules with aspect ratios of 10:9, 3:2 and 2:1 is studied. For all cases considered, the shear-rate decreasing induced transition from swinging to tumbling is observed. The temporal evolutions of the inclination angle in the plane of shear are presented in Figure 6.9, for the capsule with aspect ratio of 3:2. Similar results are obtained for capsules with aspect ratios of 10:9 and 2:1.

In the theory of Skotheim and Secomb (2007), the swinging-to-tumbling transition of an elastic capsule was found to occur via a narrow intermittent regime of successive swinging and tumbling. Abkarian et al. (2007) also observed this phenomenon in the experiment. In Figure 6.10, the temporal evolution of the inclination angle, for a capsule with NH membrane and aspect ratio 3:2, is presented at G = 0.0221 and 0.0225, which is actually near the transition region of shear rate. It

is seen that in the initial stage, the capsule carries out alternate tumbling and swinging motions, which shows some similarities to the intermittent mode of Skotheim and Secomb (2007), as well as Abkarian et al. (2007). After this initial stage, only swinging motion is observed. Similar behaviour has also been observed for elastic capsules with SK membrane and aspect ratios of 10:9 and 2:1. In much longer computation, wrinkles of the membrane due to a lack of bending resistance became severe and the computation results tended to become unreliable. Thus the present simulations may suggest that the swinging-to-tumbling transition of an elastic capsule occurs via a narrow intermittent regime of successive swinging and tumbling, similar to that of Skotheim and Secomb; however, there is not sufficient evidence in the present study to conclude that the present capsules carried out a steady intermittent motion.

6.3. Initially biconcave discoid capsules

In this section, a periodic file of initially biconcave discoid capsules with Skalak membrane, as a model of red blood cells, are considered in wall-bounded shear flow. The linear shear flow is generated by two solid walls, with distance 5*a*, moving in opposite directions, as illustrated in Figure 6.11. The Reynolds number equals 0.1 so that Stokes flow condition is satisfied. The computational domain is a cuboid box with side length 6*a* in x-axis, and 5a in y-axis and z-axis. The capsule is at the center of the domain. The boundary conditions at the upper and lower planes of the computational domain are set as solid walls moving in opposite directions. Periodic

boundary conditions are employed on the flow and spanwise directions. Uniform grid is employed, with a grid resolution of $\Delta x = \Delta y = \Delta z = a/16$. The capsule membrane is discretized into 32768 flat triangular elements connecting 16386 nodes. Grid convergence studies showed that the mesh resolutions are sufficient. In the present study, the ratio between the capsule membrane area dilation modulus and shear elasticity modulus is chosen to be large enough to keep the membrane area change within 0.5%, however not too large to make the computation diverge (Eggleton and Popel, 1998). With the dimensionless shear rate ranging from 0.0005 to 2.8, the moduli ratio C ranges from 1 to 400. For all cases considered, the cell volume changes are also within 0.5%.

6.3.1. Swinging motion

In the present study, first considered are the dynamic motion of biconcave discoid capsules in simple shear flow at shear rates: G = 0.47 ~ 2.8. From the simulation results, it is found that the capsule deforms to oblate ellipsoidal shapes and then the membrane rotates around the internal liquid. During this tank-treading motion, the capsule inclination oscillates periodically and the capsule profile undergoes periodic vacillating-breathing deformation. These behaviors are consistent with the swinging mode reported by Abkarian et al. (2007). The transient 3D and 2D profiles of the capsule during the swinging motion at G = 1.87 are presented in Figure 6.12. In the 2D images of the capsule in x-z plane, which is parallel to the shear plane, the black dots represent the same material point on the capsule membrane. From the 2D images, it is noted that the capsule inclination is changing while the capsule membrane is

rotating around the liquid inside. It is also not difficult to observe the vacillating-breathing deformation of the capsule from the 2D images in x-y plane, which is parallel to the solid moving wall, as well as from the 3D profiles of the capsule.

The temporal evolutions of the capsule's length, width and thickness under various dimensionless shear rates are presented in Figure 6.13. The temporal evolutions of the capsule's middle cross section in the plane of shear are presented in Figure 6.14. At larger shear rate, the capsule is more elongated and more aligned with the flow direction. With the shear rate ranges from 0.47 to 2.8, the capsule inclination oscillation amplitude is in the range of 2.9 ~ 3.5 degrees. Further increasing the dimensionless shear rate increases the capsule elongation and decreases the swinging amplitude. However, the steady tank treading mode of the capsule is not observed. Instead, the capsule carries out a swinging motion. The swinging mode could also be called unsteady tank-treading mode because when the membrane is rotating around the liquid inside (tank-treading), the capsule undergoes periodic shape deformation and inclination oscillation.

The average time T for the capsule membrane to complete a rotation is computed to obtain the unsteady tank treading frequency by $f = 2\pi / T$. When normalized by the shear rate k, the non-dimensional frequency f/k is presented in Figure 6.15. It is found that the normalized tank treading frequency is higher at lower dimensionless shear rate, and ranges from 0.20 to 0.24 with the dimensionless shear rate ranging from 0.47 to 2.8. Tran-Son-Tay et al. (1984) found experimentally that for younger red blood cells suspend in a medium of comparable viscosity, f/k equals 0.22. It is thus

encouraging that the present numerical modelling gives realistic estimates of the tank treading frequency.

6.3.2. Swinging-to-tumbling transition

The dynamic motion of initially biconcave discoid capsules in simple shear flow at moderate and small dimensionless shear rates is considered. Figure 6.16 presents the temporal evolutions of the inclination of the capsule's middle cross section in the plane of shear at G = 0.0045, 0.015 and 0.045. It is seen that at G = 0.045, the capsule still carries out swinging motion with amplitude much bigger than that presented in Figure 6.14. At G = 0.015, the capsule shows initial tumbling and then swinging motion, similar to that of initially oblate spheroidal capsules in previous section. With further decreasing the shear rate, the cell's motion falls into tumbling region, as shown in Figure 6.16 for G = 0.0045. The 3D profiles of the capsules during the tumbling motion at G = 0.0005 are presented in Figure 6.17. Due to a lack of membrane bending stiffness, wrinkles develop on the cell interface. The 3D profiles of the capsule are symmetric with respect to x-z plane.

6.4. Discussion

From the results of the present direct numerical simulation, it is found that the steady tank treading motion is only observed for initially spherical capsules. Similar motion for initially spherical capsules has been reported by Pozrikids (1995),

Ramanujan and Pozrikidis (1998), and Lac et al. (2004). For non-spherical capsules, for example initially oblate spheroidal or biconcave discoid capsules, they only carry out swinging motion at large shear rate as described in previous sections. In the study of Ramanujan and Pozrikidis (1998) of non-spherical capsules with elastic membranes in simple shear flow, swinging motion of the capsules, similar to the present study, was observed.

This is due to the fact that for spherical capsules, the material points on the membrane are equivalent, because of their initially spherical equilibrium shape; but for initially non-spherical capsules, they are not the case. Assuming both spherical and non-spherical capsules could achieve steady tank-treading mode. For spherical capsule, the membrane elastic energy can keep unchanged during the motion, because of the equivalent membrane points, and thus the steady mode can be maintained. However, for non-spherical capsules, during the tank treading motion, the membrane shear elastic energy undergoes periodic variation, and passes two minima in one period due to the symmetry of the initial reference shape. This is actually the so called "shape memory effect", which is due to the non-spherical initial minimum energy shape and the shear elasticity, and has been observed in Fischer's experiment (2004). The variation of the membrane elastic energy will provide a perturbation force to the steady tank-treading mode, and the steady motion can not be maintained. The initially non-spherical capsule thus can only carries out swinging motion in shear flow when the shear rate is high.

For liquid-filled capsules with elastic membranes, it has been long recognized that the tank treading to tumbling transition can be induced by increasing the internal

liquid viscosity or membrane viscosity of the cell. In both cases due to the fact that the viscosity increases, the transfer of shear torque to the membrane becomes more and more difficult; and then the capsule would behave like a solid body which undergoes tumbling motion.

Recently, the experimental findings of Abkarian et al. (2007) for red blood cells, as well as the present numerical results for non-spherical capsules show that in shear flow, the swinging-to-tumbling transition can be induced by lowering the shear rate. This contradicts with well-known theory of Keller and Skalak's (1982). In fact, the shear rate induced transition, is also due to the shape memory effect of the three-dimensional capsules.

In Keller and Skalak's theory, the capsule is assumed to have a fixed ellipsoidal shape during the membrane tank treading motion, and the membrane elastic energy was kept unchanged. These assumptions actually have excluded the shape memory effect. Based on the fixed-shape theoretical model of Keller and Skalak (1982), and further assumed that the membrane elastic energy undergoes a periodic variation during the tank-treading motion (which actually includes the shape memory effect), both the swinging motion and shear rate induced swinging-to-tumbling transition can be successfully predicted by the recent theoretical model of Skotheim and Secomb (2007), as well as Abkarian et al. (2007). However, it is not so realistic that the capsule can simultaneously keep its shape unchanged while its membrane elastic energy changing. The present study is by direct numerical simulation and relaxes all these assumptions.

Lowering the shear rate could induce the swinging-to-tumbling transition. This is due to the shape memory effect of the three-dimensional capsules. When the shear rate is very small, the fluid shear force acting on the capsule membrane is not big enough to drive the membrane tank treading up the elastic energy gradient. The capsule is then relatively solidified and can only tumble like a rigid body.

It is also interesting to observe that the shear rate induced transition of a capsule's motion from tank-treading mode to tumbling mode was observed in three-dimensional non-spherical but not in the two-dimensional non-circular capsules. This is because of the differences of geometry and thus mechanics of two-dimensional and three-dimensional capsules. For two-dimensional capsules, the interfacial elasticity modulus can only resist stretching or compression, not like the membrane shear elasticity of three-dimensional capsules. The transverse shear tension of the two-dimensional capsule is related to the membrane bending moment. When bending rigidity is neglected, two-dimensional capsule can not resist any shear deformation and thus behave qualitatively different with three-dimensional non-spherical capsules.

The computational load for the present three-dimensional is very heavy. Even with the multi-block technique, the typical computational time ranges from one day for a steady case to around four weeks for the unsteady biconcave discoid case (running on SVU linux 64 cluster).

6.5. Concluding remarks

The dynamic motion of capsules in shear flow is studied by direct numerical simulation. The capsules consist of Newtonian liquid droplets enclosed by elastic membranes with or without considering the membrane-area incompressibility. The dynamic motion of capsules with initially spherical, oblate spheroidal and biconcave discoid unstressed shapes is studied, under various shear rates. The results show that spherical capsules deform to stationary shapes and achieve steady tank-treading motion. Such a steady mode has not been observed for non-spherical capsules. At large shear rates, non-spherical capsules carry out a swinging motion, in which a capsule undergoes periodic shape deformation and inclination oscillation while its membrane is rotating around the liquid inside. With the shear rate decreasing, the capsules' inclination oscillation amplitude increases, and finally triggers the swinging-to-tumbling transition.

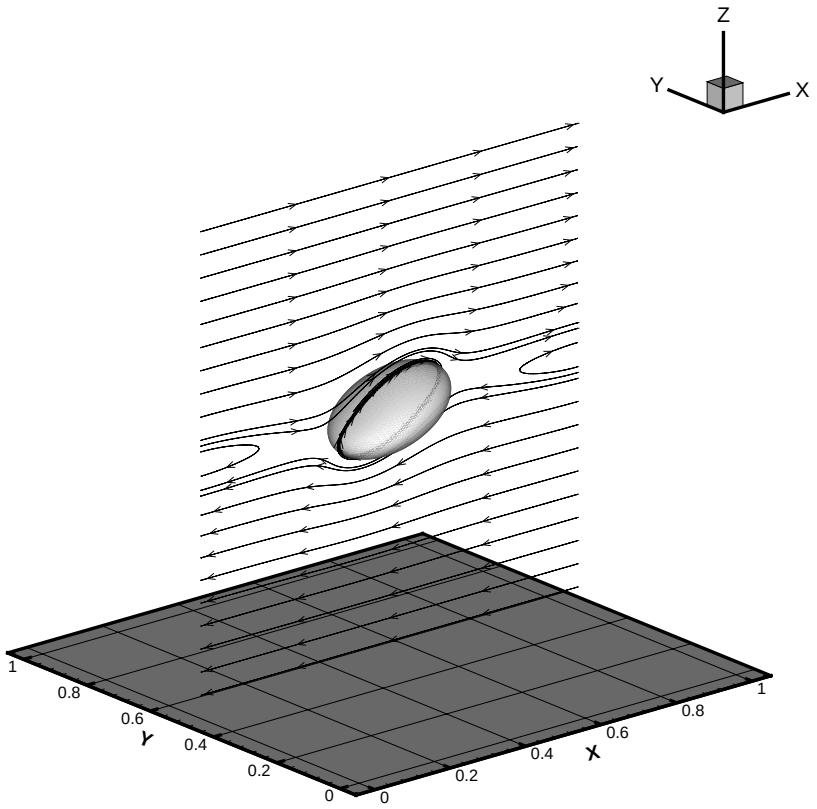

Figure 6.1 Steady deformed capsule and the flow field around the cross section of the capsule in the plane of shear at $G = 0.05$

(a)

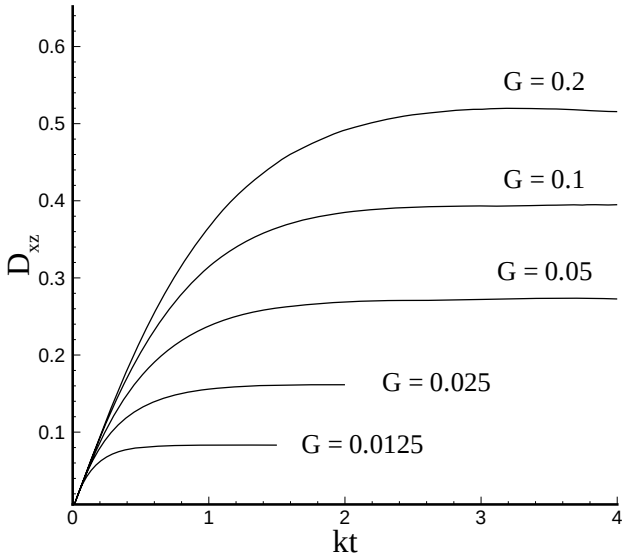

(b)

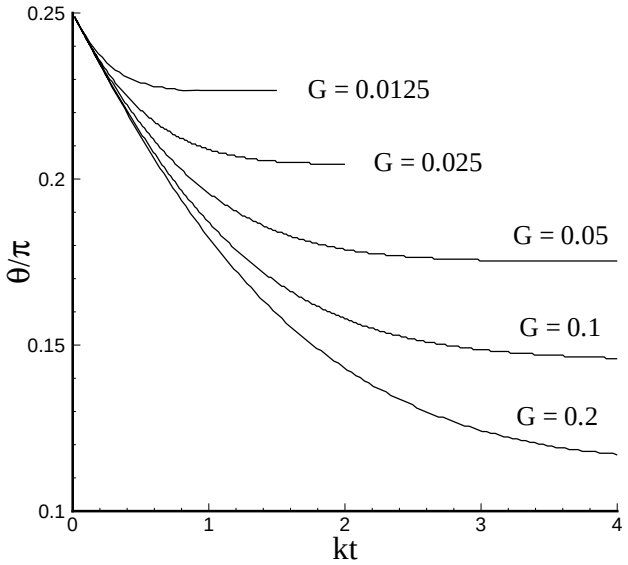

Figure 6.2 Temporal evolutions of the (a) Taylor shape parameter, (b) inclination angle of the initially spherical capsules with ZT membrane

(a)

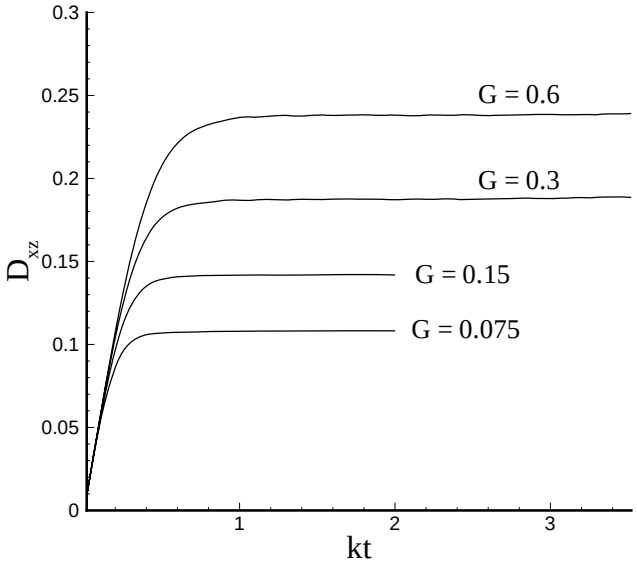

(b)

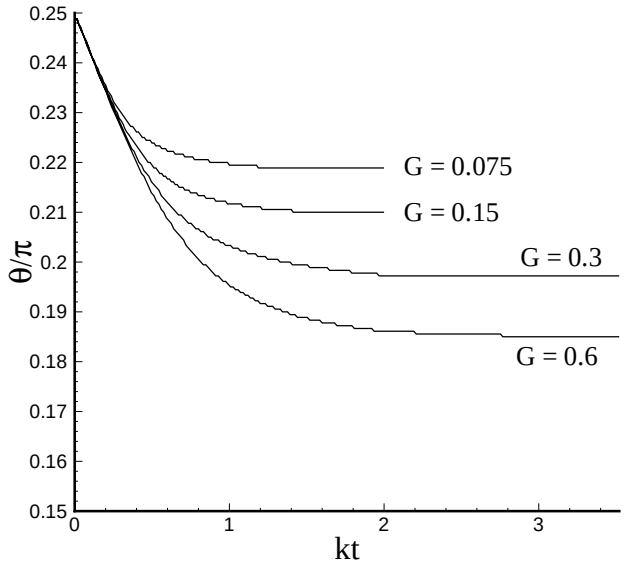

Figure 6.3 Temporal evolutions of the (a) Taylor shape parameter, (b) inclination angle of the initially spherical capsules with SK membrane at $C = 100$

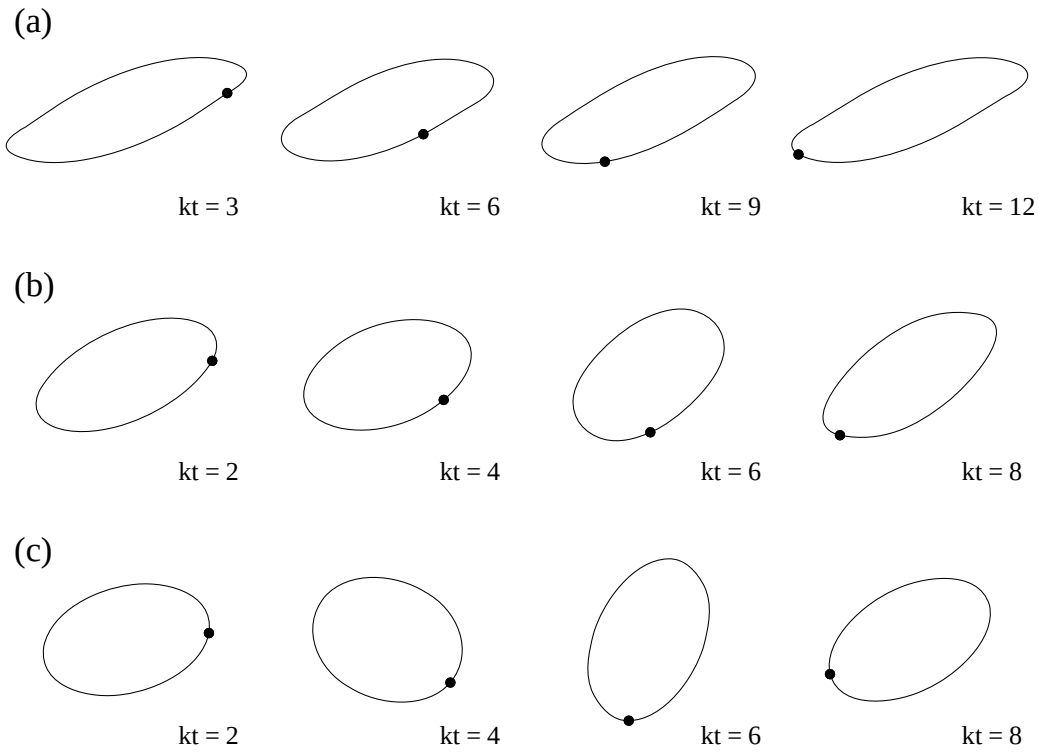

Figure 6.4 Membrane profiles in the plane of shear for initially oblate spheroidal capsules with aspect ratio of 3:2. (a) $G = 0.2$; (b) $G = 0.05$; (c) $G = 0.0125$

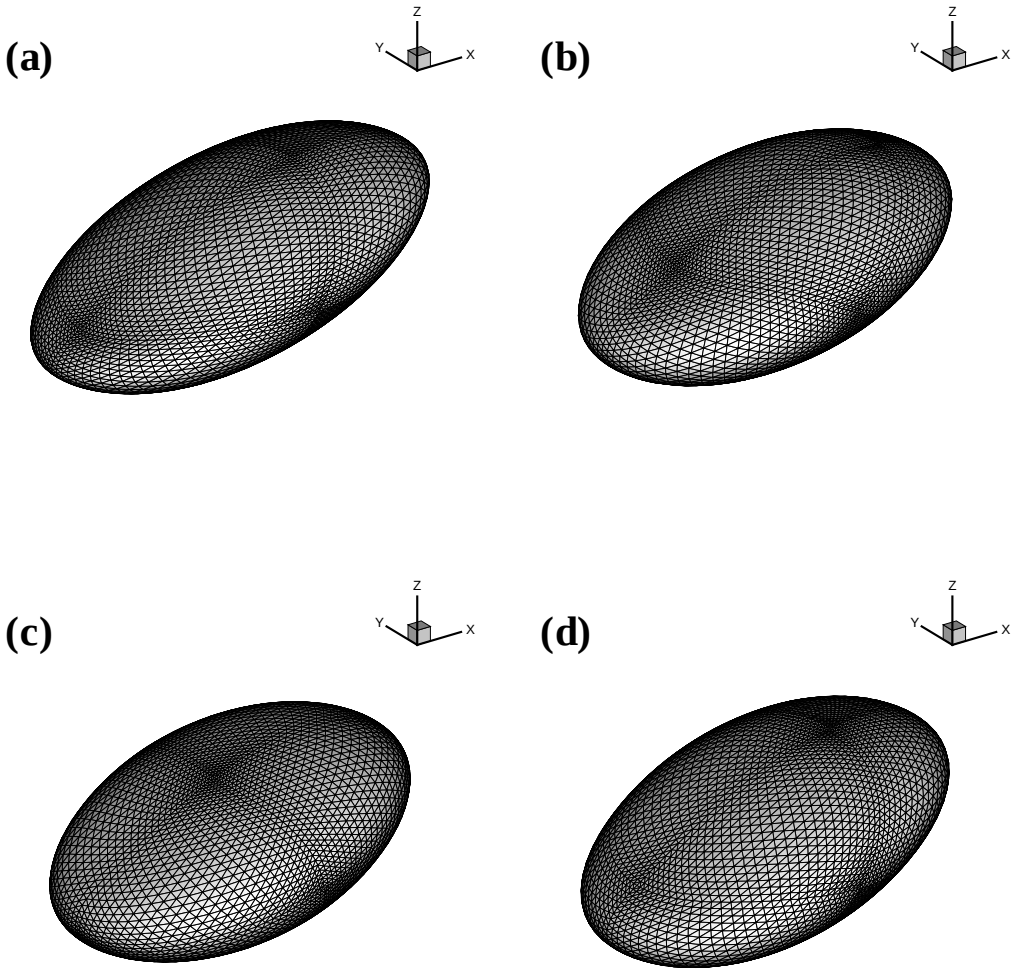
(a)
Z
Y
X
(b)
Z
Y
X
(c)
Z
Y
X
(d)
Z
Y
X

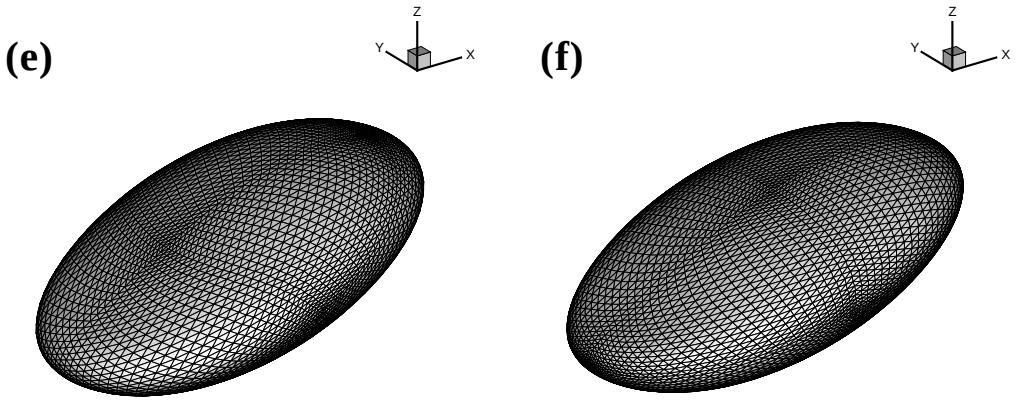

Figure 6.5 3D profiles of the capsule (in Fig. 6(a)) during the swinging motion. The dimensionless time kt = (a) 3; (b) 5; (c) 7; (d) 9; (e) 11; (f) 13

(a)

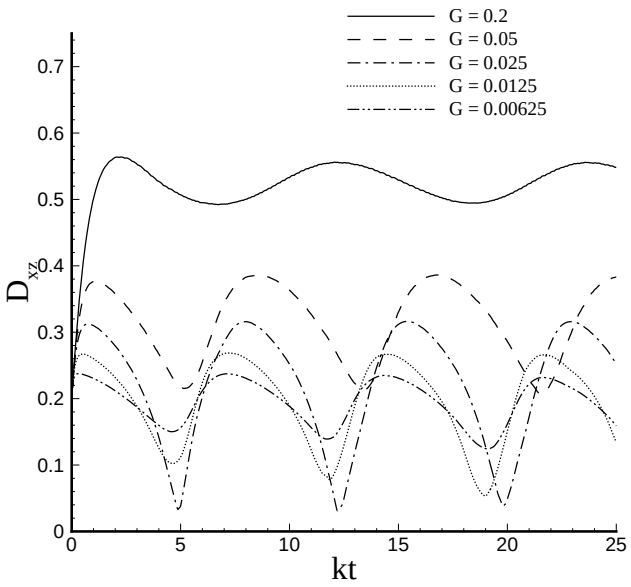

(b)

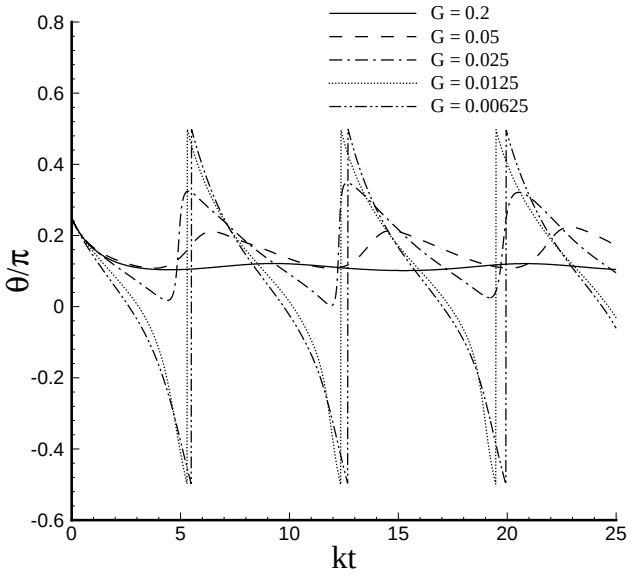

Figure 6.6 Temporal evolutions of the (a) Taylor shape parameter, (b) inclination angle of the initially oblate spheroidal capsules (aspect ratio 3:2) with ZT membrane

(a)

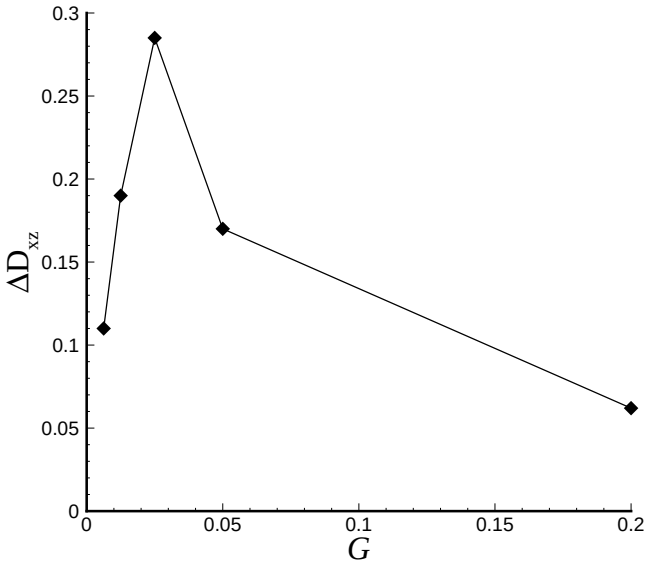

(b)

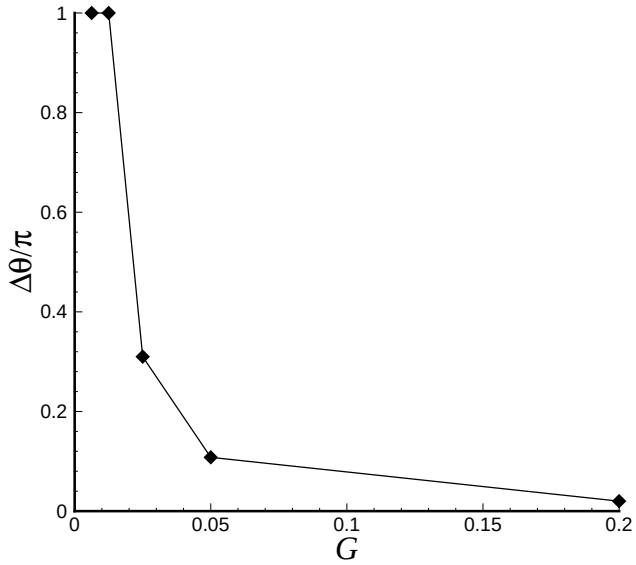

Figure 6.7 Oscillation amplitudes of the (a) Taylor shape parameter, (b) inclination angle of the initially oblate spheroidal capsules (aspect ratio 3:2) with ZT membrane

(a)

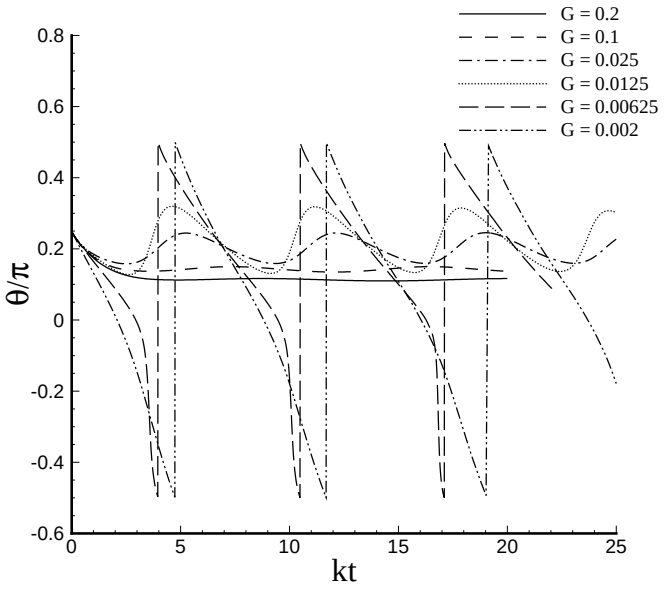

(b)

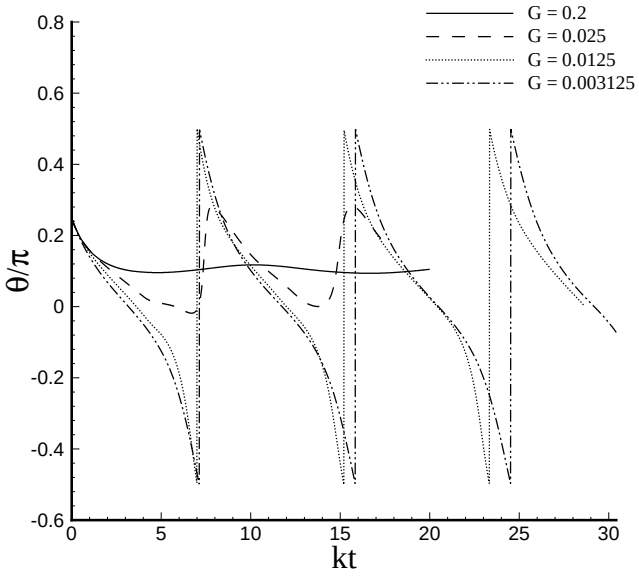

Figure 6.8 Temporal evolutions of the inclination angle of the initially oblate spheroidal capsules with ZT membrane, the aspect ratios are (a) 10:9; (b) 2:1

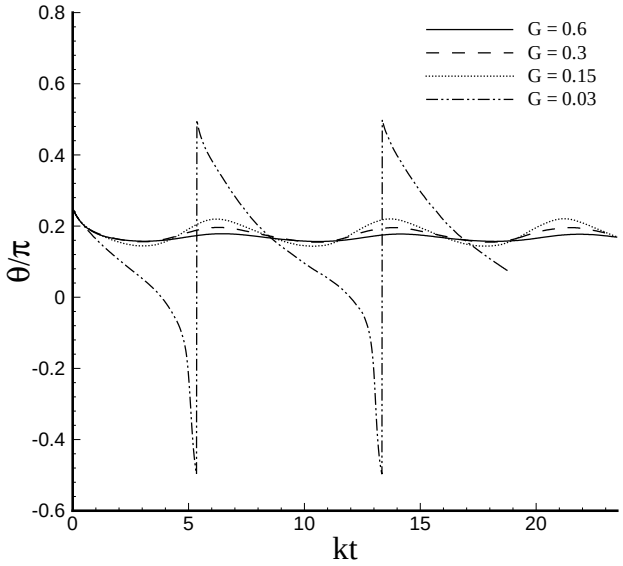

Figure 6.9 Temporal evolutions of the inclination angle of the initially oblate spheroidal capsules (aspect ratio 3:2) with SK membrane at C = 100

(a)

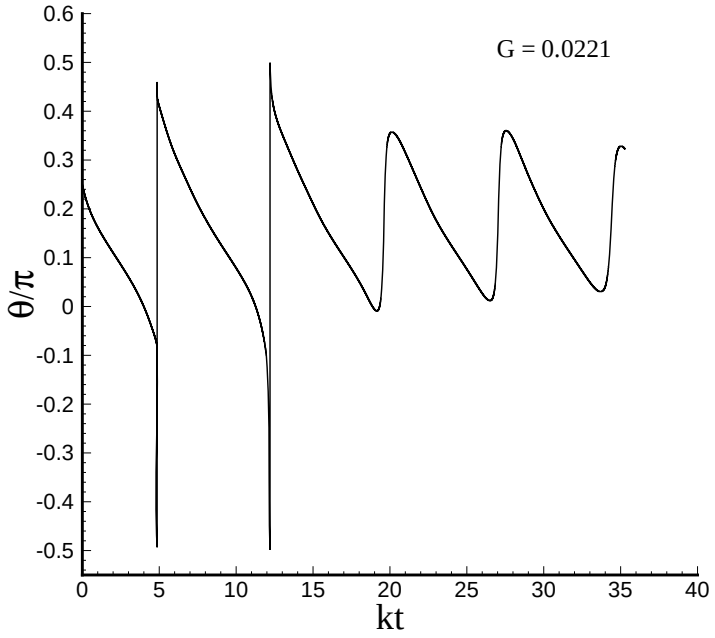

(b)

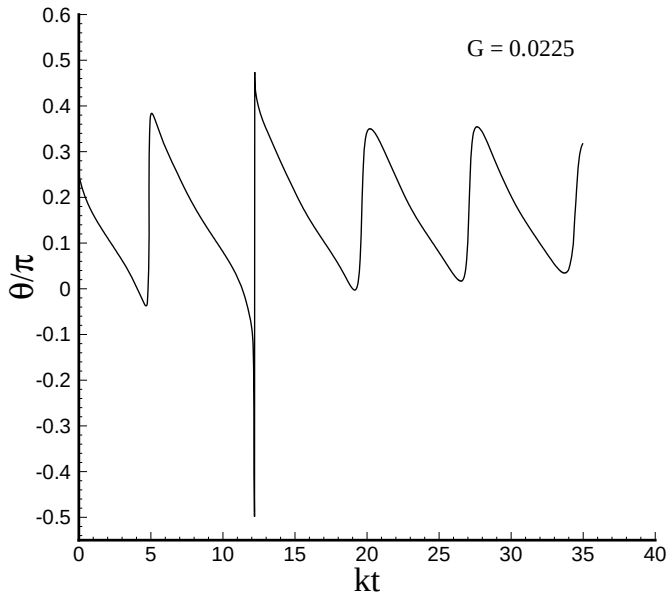

Figure 6.10 Temporal evolutions of the inclination angle of the initially oblate spheroidal capsules (aspect ratio 3:2) with ZT membrane at G = (a) 0.0221; (b) 0.0225

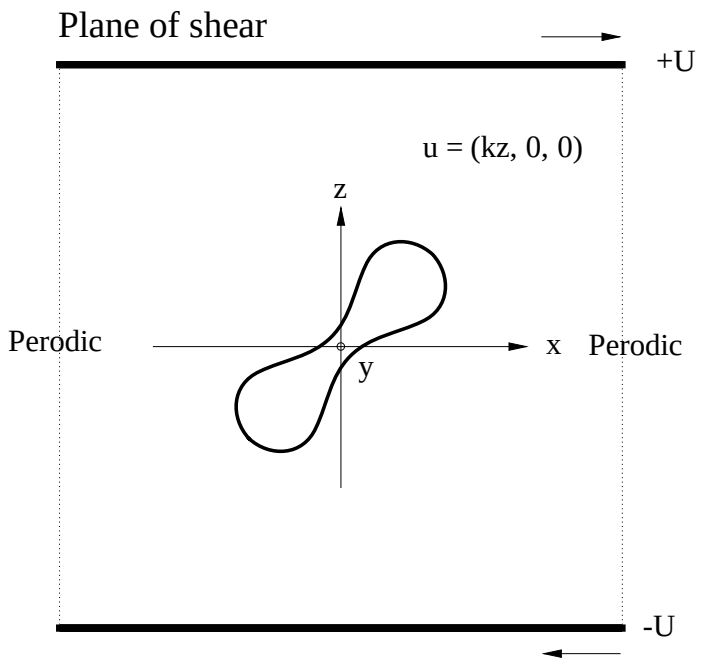

Figure 6.11 A periodic suspension of initially biconcave-discoid cells in shear flow

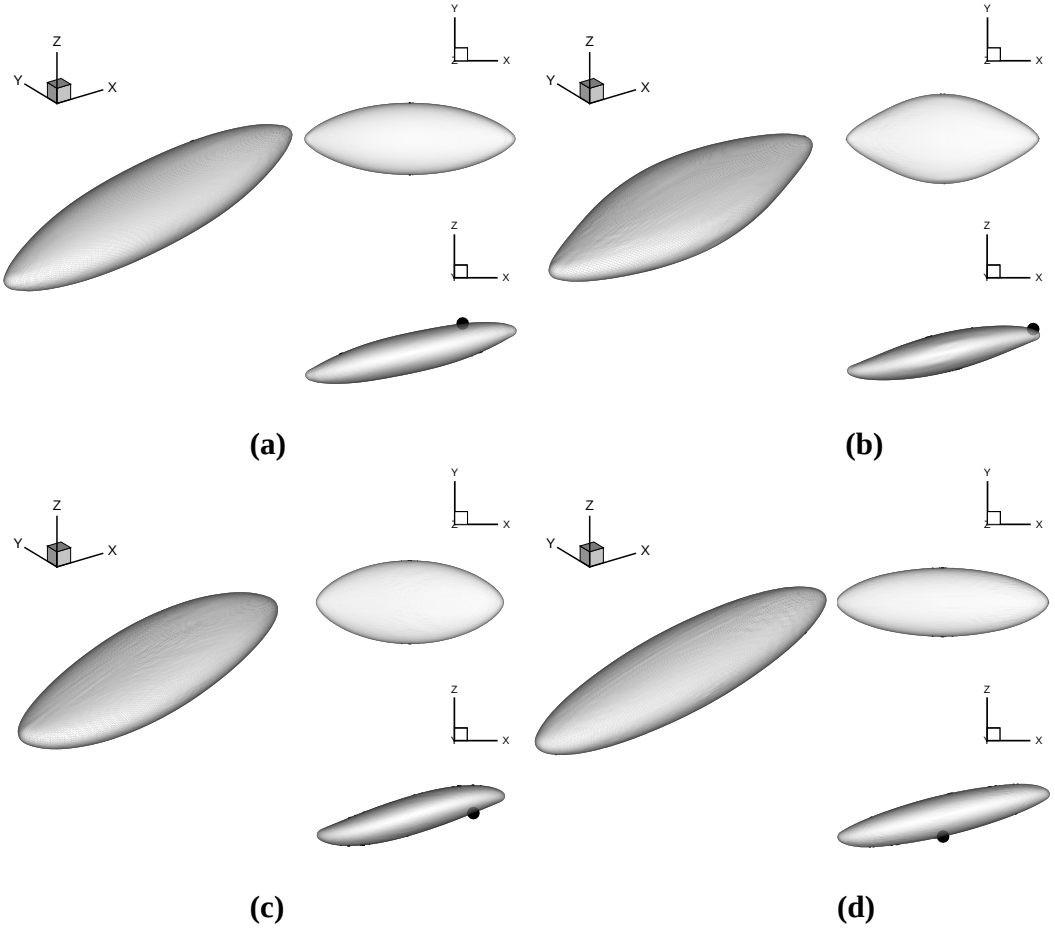

Figure 6.12 Profiles of the ghost cell in the swinging motion at G = 1.87 and kt = (a) 5; (b) 9; (c) 13; (d) 17

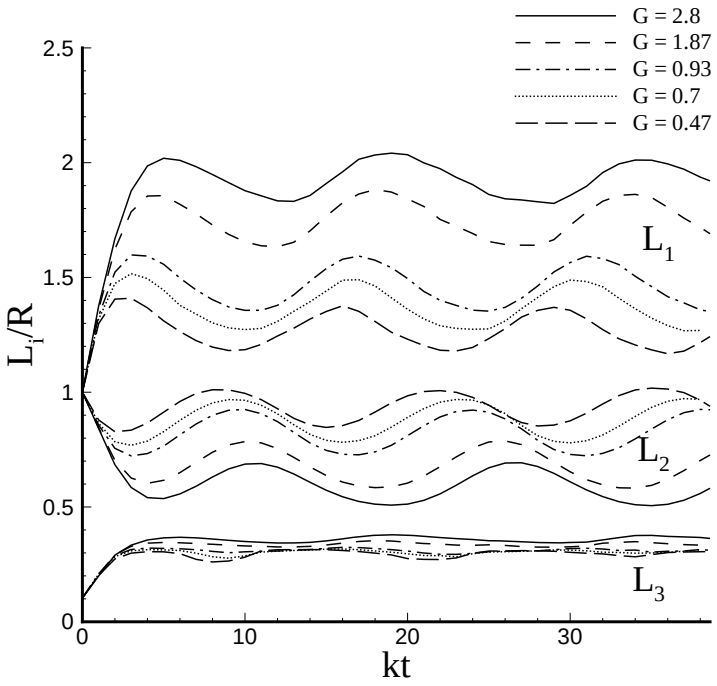

Figure 6.13 Temporal evolution of the ghost cell's length (L_1), width (L_2) and thickness (L_3) under various dimensionless shear rates

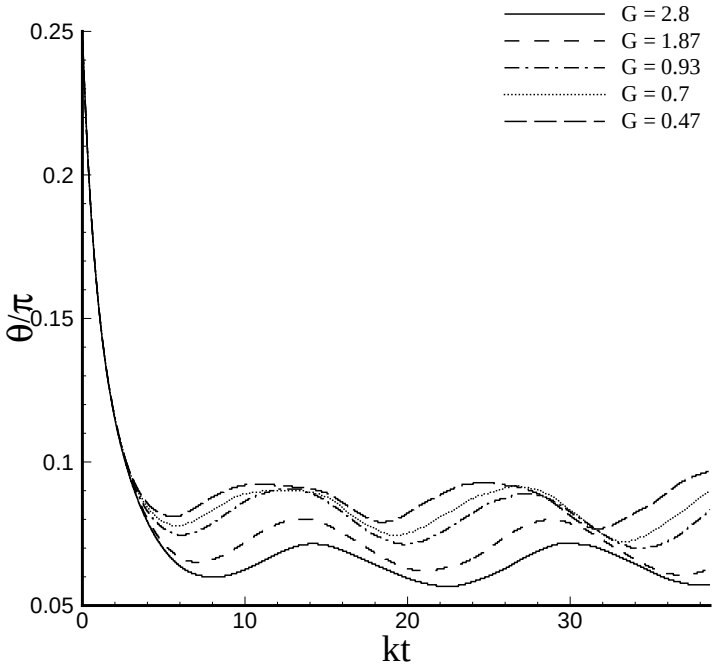

Figure 6.14 Temporal evolution of the inclination angle of the ghost cell's middle cross section (in the plane of shear) under various dimensionless shear rates

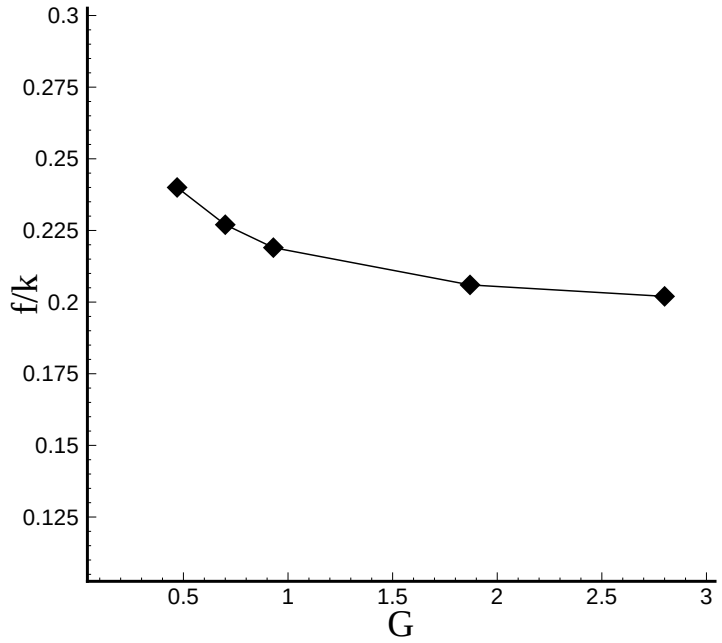

Figure 6.15 Tank-treading frequency of the ghost cell membrane under various dimensionless shear rates

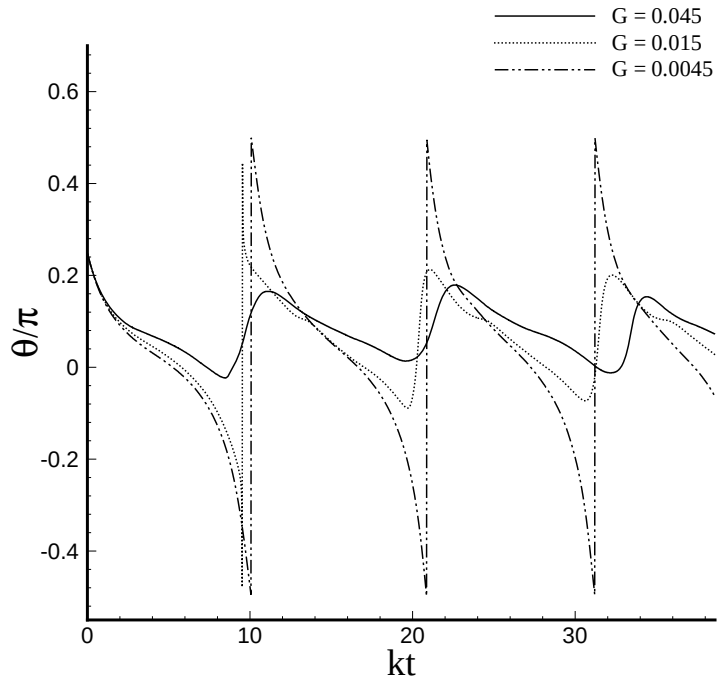

Figure 6.16 Temporal evolution of the inclination angle of the ghost cell's middle cross section (in the plane of shear) under various dimensionless shear rates

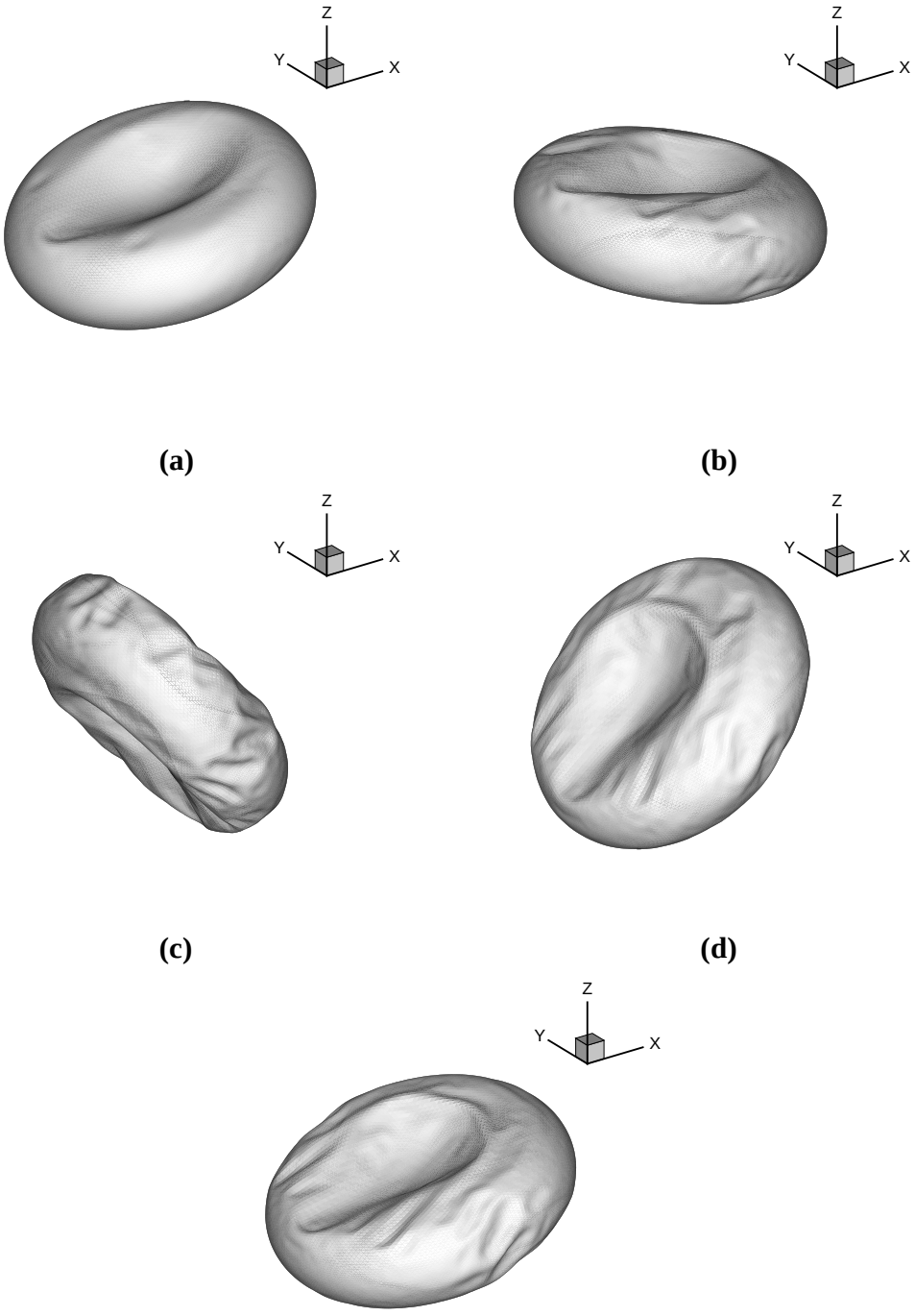

Figure 6.17 3D profiles of the ghost cell during the tumbling motion. The dimensionless time kt = (a) 2; (b) 6; (c) 9; (d) 11; (e) 13 and G = 0.0005

Chapter 7 Conclusions and Recommendations

7.1 Conclusions

A hybrid method, combining the immersed boundary method and the multi-block lattice Boltzmann method, was proposed to simulate moving boundaries interacting with incompressible viscous fluid. The present method preserves the advantages of the immersed boundary method and lattice Boltzmann method; and at the same time improves their accuracy and efficiency by employing a multi-block strategy. Besides dealing with elastic boundaries interacting with fluid, the method can also efficiently simulate solid moving boundaries; this is achieved by employing the direct forcing technique. Four benchmark computations were carried out to validate the present method: flow past a circular cylinder, two cylinders moving with respect to each other, flow around a hovering wing, and the deformation of a circular liquid-filled elastic capsule in simple shear flow. The results agree well with published literatures and show that the present numerical method could be an alternative approach for the simulation of fluid/structure interactions.

Based on the hybrid approach proposed, the effect of membrane bending stiffness on the deformation of two-dimensional liquid-filled capsules enclosed by elastic membranes, was investigated numerically in simple shear flow. The deformation of

capsules with initially circular, elliptical and biconcave resting shapes was studied; the capsules' minimum bending-energy configurations were considered as either uniform-curvature shapes (like circle or flat plate) or their initially resting shapes. The results show that for capsules with minimum bending-energy configurations having uniform curvature (circle or flat plate), the membrane carries out tank-treading motion; and the steady deformed shapes become more rounded if the bending stiffness is increased. For elliptical and biconcave capsules with resting shapes as minimum bending-energy configurations, it is quite interesting to find that with the bending stiffness increasing or the shear rate decreasing, the capsules' motion changes from tank-treading mode to tumbling mode, and resembles Jeffery's tumbling mode at large bending stiffness. The present study shows that, besides viscosity ratio and membrane viscosity, the membrane bending stiffness may be another factor which can lead to the transition of a capsule's motion from tank treading to tumbling.

Based on the hybrid approach proposed, the effect of inertia on the transient deformation of two-dimensional liquid-filled elastic capsules and the flow structure around them, was investigated numerically in simple shear flow. The simulation results show that the inertia effect gives rise to a transient process, in which the capsule elongation and inclination overshoot and then show dampened oscillations towards the steady states. Inertia effect also promotes the steady deformation, and decreases the tank treading frequency of the capsule. Inertia strongly affects not only the capsule deformation, but also the flow pattern. There is flow separation inside the

capsule. Also, the vorticity magnitude and gradient on the capsule interface increase with increasing Reynolds number.

The proposed hybrid method was extended to three-dimensional to study the flow-induced deformation of liquid-filled capsules with elastic membranes. The membrane of the three-dimensional capsule was discretized into unstructured flat triangular elements, and a finite element model was incorporated to obtain the forces acting on the membrane nodes. The present method was validated by studying the transient deformation of initially spherical and oblate spheroidal capsules with various membrane laws under shear flow. The present results agree well with published theoretical or numerical results. Compared with the original immersed boundary-lattice Boltzmann method, the present method is much more efficient. The present method is capable to take the inertia effect into account. This was demonstrated by studying the deformation of spherical capsules in shear flow at moderate Reynolds numbers. The transient deformation of capsules with initially biconcave disk shape was also simulated. The unsteady tank treading motion was followed for a whole period in the present work. Due to numerical instabilities encountered in previous computations, this motion has not been fully recovered by numerical simulation so far.

Based on the three-dimensional hybrid approach proposed, the dynamic motion of three-dimensional capsules in shear flow is studied by direct numerical simulation. The capsules consist of Newtonian liquid droplets enclosed by elastic membranes with or without considering the membrane-area incompressibility. The dynamic

motion of capsules with initially spherical, oblate spheroidal and biconcave discoid unstressed shapes was studied, under various shear rates. The results show that spherical capsules deform to stationary shapes and achieve steady tank-treading motion. At large shear rates, non-spherical capsules carry out a swinging motion, in which a capsule undergoes periodic shape deformation and inclination oscillation while its membrane is rotating around the liquid inside. With the shear rate decreasing, the capsules' inclination oscillation amplitude increases, and finally triggers the swinging-to-tumbling transition.

7.2 Recommendations

In the present study, because the immersed boundary method was employed, the simulations were restricted to capsules with the internal fluid viscosity same to that outside. In the future work, the present method could be improved to relax this assumption. This may be achieved by replacing the immersed boundary method with the front-tracking method (Unverdi and Tryggvason, 1992; Lallemand et al. 2007). This would point to a broader application of the numerical studies, for example, to use the observed dynamics to measure capsule properties, or use the simulations to suggest parameter regimes for experiments where the properties can be most sensitively deduced.

The membrane models in the present study do not incorporate the membrane viscosity effect. For some capsules, for example the red blood cells, the energy

dissipation due to the membrane viscosity has been shown experimentally to be between 2 and 4 times the dissipation in the cytoplasm (Fischer, 1980; Tran-Song-Tay et al. 1984). Thus it is needed to consider the membrane viscosity in the future work, when the simulation is carried out to model the red blood cells.

Reference

Abkarian, M., Faivre, M. and Viallat, A., Swinging of red blood cells under shear flow, Phys. Rev. Lett., 98: 188302, 2007.

Asinari, P. and Luo, L.-S., A consistent lattice Boltzmann equation with baroclinic coupling for mixtures, J. Comput. Phys., 227: 38785-3895, 2008.

Barthès-Biesel, D., Motion of spherical microcapsule freely suspended in a linear shear flow, J. Fluid Mech., 100: 831-853, 1980.

Barthès-Biesel, D. and Rallison, J. M., The time-dependent deformation of a capsule freely suspended in a linear shear flow, J. Fluid Mech., 113: 251-267, 1981.

Barthès-Biesel, D. and Sgaier, H., Role of membrane viscosity in the orientation and deformation of a spherical capsule suspended in shear flow, J. Fluid Mech., 160: 119-135, 1985.

Beaucourt, J., Rioual, F., Séon, T., Biben, T. and Misbah, C., Steady to unsteady dynamics of a vesicle in a flow, Phys. Rev. E, 69: 011906, 2004.

Benzi, R. and Succi, S., 2-dimensional turbulence with the lattice Boltzmann equation, J. of Phys. A, 23: L1-L5, 1990.

Bhatnagar, P. L., Gross, E. P. and Krook, M., A model for collision processes in gases. I. Small amplitude processes in charged and neutral one-component systems, Phys. Rev. 94: 511-525, 1954.

Biben, T. and Misbah, C., Tumbling of vesicles under shear flow within an advected-field approach, Phys. Rev. E, 67: 031908, 2003.

Breyiannis, G. and Pozrikidis, C., Simple shear flow of suspensions of elastic capsules, Theor. & Comp. Fluid Dyn., 13: 327-347, 2000.

Charrier, J. M., Shrivastava, S. and Wu, R., Free and constrained inflation of elastic membranes in relation to thermoforming non-axisymmetric problems, J. Strain Anal., 24: 55-74, 1989.

Chen, S.Y., Diemer, K, Doolen, D, Eggert, K., Fu, C., Gutman, S. and Travis, B. J., Lattice Gas Automata for flow through porous-media, Physica D., 47: 72-84, 1991.

Chen, S., Martinez, D. and Mei, R., On boundary conditions in lattice Boltzmann methods, Phys. Fluids, 8(9): 2527-2536, 1996.

Chen, S. and Doolen, G. D., Lattice Boltzmann method for fluid flows, Ann. Rev. Fluid Mech., 30: 329–364, 1998.

Chew, Y. T., Shu, C. and Niu, X. D., Simulation of unsteady and incompressible flows by using taylor series expansion- and least square- based lattice Boltzmann method, Int. J. Mod. Phys. C, 13: 719-738, 2002.

Chien, S., Red cell deformability and its relevance to blood flow, Annu. Rev. Physiol., 49: 177-192, 1987.

de Haas, K. H., Blom, C., van den Ende, D., Duits, M. H. G. and Mellema, J., Deformation of giant lipid bilayer vesicles in shear flow, Phys. Rev. E, 56: 7132-7137, 1997.

d'Humières, D., Generalized lattice-Boltzmann equations, Prog. Astronaut. Aeronaut., 159: 450-458, 1992.

Eggleton, C. D. and Popel, A. S., Large deformation of red blood cell ghosts in a simple shear flow, Phys. Fluids, 10 (8): 1834-1845, 1998.

Fadlun, E. A., Verzicco, R., Orlandi, P. and Mohd-Yusof, J., Combined immersed-boundary finite-difference methods for three-dimensional complex flow simulations, J. Comput. Phys., 161: 35-60, 2000.

Feng, Z. G. and Michaelides, E. E., The immersed boundary-lattice boltzmann method for solving fluid-particles interaction problems, J. Comput. Phys., 195: 602-628, 2004.

Feng, Z. G. and Michaelides, E. E., Proteus: a direct forcing method in the simulations of particulate flows, J. Comput. Phys., 202: 20-51, 2005.

Filippova, O. and Hänel, D., Grid refinement for lattice-BGK models, J. Comput. Phys., 147: 219-228, 1998.

Filippova, O. and Hanel, D., Acceleration of Lattice-BGK Schemes with Grid Refinement, J. Comput. Phys., 165: 407-427, 2000.

Fisher, T. M., On the energy dissipation in a tank-treading human red blood cell, Biophys. J., 32: 863-868, 1980.

Fisher, T. M., Shape memory of red blood cells, Biophys. J., 86: 3304-3313, 2004.

Fischer, T. M., Stöhr-Liesen, M. and Schmid-Schönbein, H., The red cell as a fluid droplet: tank tread-like motion of the human erythrocyte membrane in shear flow, Science, 202: 894-896 (1978).

Fung, Y. C., Foundations of Solid Mechanics, Prentice-Hall, Englewood Cliffs, NJ, 1965.

Ginzburg, I., Consistent lattice Boltzmann schemes for the Brinkman model of porous flow and infinite Chapman-Enskog expansion, Phys. Rev. E, 77: 066704, 2008.

Goldsmith, H. L., Deformation of human red cells in tube flow, Biorheology, 7: 235-242, 1971.

Goldsmith, H. L. and Marlow, J., Flow behavior of erythrocytes. I. Rotation and deformation in dilute suspensions, Proc. R. Soc. Lond. B., 182: 351-384, 1972.

Goldstein, D., Handler, R. and Sirovich, L., Modeling a no-slip flow boundary with an external force field, J. Comput. Phys., 105: 354-366, 1993.

Grunau, D., Chen, S., and Eggert, K., A lattice Boltzmann model for multiphase fluid flows, Phys. Fluids A, 5: 2557-2562, 1993.

Gunstensen, A. K., Rothman, D. H., Zaleski, S. and Zanetti G., Lattice Boltamann model of immiscible fluids, Phys. Rev. A, 43: 4320-4327, 1991.

Guo, Z. L., Zheng, C. G. and Shi, B. C., Discrete lattice effects on the forcing term in the lattice Boltzmann method, Phys. Rev. E, 65: 046308, 2002.

Guo, Z. L., Zheng, C. G. and Shi, B. C., Non-equilibrium extrapolation method for velocity and pressure boundary conditions in the lattice Boltzmann method, Chinese Physics, 11: 366-374, 2002.

He, X. and Doolen, G., Lattice Boltzmann method on curvilinear coordinates system: Flow around a circular cylinder, J. Comput. Phys., 134: 306-315, 1997a.

He, X. and Doolen, G., Lattice Boltzmann method on a curvilinear coordinate system: Vortex shedding behind a circular cylinder, Phys. Rev. E, 56: 434-440, 1997b.

Hinton, F.L., Rosenbluth, M.N., Wong, S.K., Lin-Liu, Y.R. and Miller, R.L., Modified lattice Boltzmann method for compressible fluid simulations, Phys Rev E, 63: 061212, 2001.

Hirt, C.W., Amsden, A.A. and Cook, J.L., An arbitrary Lagrangian–Eulerian computing method for all flow speeds, J. Comput. Phys., 14: 227–253, 1974.

Hou, S., Zou, Q., Chen, S., Doolen, G. and Cogley, A. C., Simulation of cavity flow by the lattice boltzmann method, J. of Comp. Phys., 118: 329-347, 1995.

Jeffery, J. B., The motion of ellipsoidal particles immersed in a viscous fluid, Proc. R. Soc. London A, 102: 161-179, 1922.

Kwak, S. and Pozrikids, C., Effect of membrane bending stiffness on the axisymmetric deformation of capsules in uniaxial extensional flow, Phys. Fluids, 13: 1234-1242, 2001

Keller, S. R. and Skalak, R., Motion of a tank-treading ellipsoid particle in a shear flow, J. Fluid Mech., 120: 27-47, 1982.

Kraus, M., Wintz, W., Seifert, U. and Lipowsky, R., Fluid vesicles in shear flow, Phys. Rev. Lett., 77: 3685-3688, 1996.

Lac, E., Barthes-Biesel, D., Pelekasis, N. A. and Tsamopoulos, J., Spherical capsules in three-dimensional unbounded Stokes flows: effect of the membrane constitutive law and onset of buckling, J. Fluid Mech. 516 (2004) 303-334.

Ladd, A.J.C., Numerical simulations of particulate suspensions via a discretized Boltzmann equation Part I. Theoretical foundation, J. Fluid. Mech., 271: 285–310, 1994a.

Ladd, A.J.C., Numerical simulations of particulate suspensions via a discretized Boltzmann equation. Part II. Numerical results, J. Fluid. Mech., 271: 311–339, 1994b.

Lai, M. C. and Peskin, C. S., An immersed boundary method with formal second-order accuracy and reduced numerical viscosity, J. Comput. Phys., 160: 705-719, 2000.

Lallemand, P. and Luo, L.-S., Theory of the lattice Boltzmann method: dispersion, dissipation, isotropy, Galilean invariance, and stability, Phys. Rev. E, 61: 6546–6562, 2000.

Lallemand, P., Luo, L.-S. and Peng, Y., A lattice Boltzmann front-tracking method for interface dynamics with surface tension in two dimensions, J. Comput. Phys., 226: 1367-1384, 2007.

Lee, J. and Pozrikidis, C., Effect of surfactants on the deformation of drops and bubbles in Navier-Stokes flow, Comput. Fluids, 35: 43-60, 2006.

Lipowsky, R., The conformation of membranes, Nature, 349: 475-481, 1991.

Liu, H. and Kawachi, K., A numerical study of undulatory swimming, J. Comput. Phys., 155: 223–247, 1999.

Luo, L.-S. and Girimaji, S.S., Lattice Boltzmann model for binary mixtures, Phys Rev E, 66:035301, 2002.

Luo, L.-S. and Girimaji, S.S., Theory of the lattice Boltzmann method: Two-fluid model for binary mixtures, Phys Rev E, 67:036302, 2003.

Misbah, C., Vacillating breathing and tumbling of vesicles under shear flow, Phys. Rev. Lett., 96: 028104, 2006.

Mohd-Yusof, J., Combined immersed-boundary/B-spline methods for simulations of flow in complex geometries, Annual Research Briefs (Center for Turbulence Research, NASA Ames and Stanford University), 317-327, 1997.

Nannelli, F. and Succi, S., The lattice Boltzmann equation on irregular lattices, J. Stat. Phys., 68: 401-407, 1992.

Niu, X. D., Chew, Y. T. and Shu, C., Simulation of flows around an impulsively started circular cylinder by taylor series expansion- and least squares-based lattice Boltzmann method, J. Comput. Phys., 188: 176-193, 2003.

Noguchi, H. and Gompper, G., Fluid vesicles with viscous membranes in shear flow, Phys. Rev. Lett., 93: 258102, 2004.

Noguchi, H. and Gompper, G., Dynamics of fluid vesicles in shear flow: effect of membrane viscosity and thermal fluctuations, Phys. Rev. E, 72: 011901, 2005.

Noguchi, H. and Gompper, G., Swinging and tumbling of fluid vesicles in shear flow, Phys. Rev. Lett., 98: 128103, 2007.

Pan, C., Hilpert, M. and Miller, C.T., Lattice-Boltzmann simulation of two-phase flow in porous media, Water Resour. Res., 40: W01501, 2004.

Peng, Y., Shu, C., Chew, Y. T., Niu, X. D. and Lu, X. Y., Application of multi-block approach in the immersed boundary-lattice Boltzmann method for viscous fluid flows, J. Comput. Phys., 218: 460-478, 2006.

Peng, Y. and Luo, L.-S., A comparative study of immersed-boundary and interpolated bounce-back methods in LBE, Progress Comput. Fluid Dyna., 8: 156-167, 2008.

Peskin, C. S., Numerical analysis of blood flow in the heart, J. Comput. Phys. 25: 220–252, 1977.

Peskin, C. S., The immersed boundary method, Acta Numer., 11: 479–517, 2002.

Pfafferott, C., Nash, G. B. and Meiselman, H. J., Red blood cell deformation in shear flow, J. Biophys. Soc., 47: 695–704, 1985.

Pozrikidis, C., Boundary integral and singularity methods for linearized viscous flow, Cambridge University Press, 1992.

Pozrikidis, C., Finite deformation of liquid capsules enclosed by elastic membranes in simple shear flow, J. Fluid Mech., 297: 123-152, 1995.

Pozrikidis, C., Effect of membrane bending stiffness on the deformation of capsules in simple shear flow, J. Fluid Mech., 440: 269-291, 2001.

Pozrikidis, C., Modeling and simulation of capsules and biological cells, Chapman & Hall/CRC, London, 2003a.

Pozrikidis, C., Numerical simulation of the flow-induced deformation of red blood cells, Annals Biomed. Eng., 31: 1194-1205, 2003b.

Qi, D. and Luo L-S. Rotational and orientational behaviour of a three-dimensional spheroidal particles in Couette flow, J. Fluid Mech., 447:201–203, 2003.

Ramamurti, R. and Sandberg, W.C., A three-dimensional computational study of the aerodynamic mechanisms of insect flight, J. Exp. Biol., 205: 1507–1518, 2002.

Ramanujan, S. and Pozrikidis, C., Deformation of liquid capsules enclosed by elastic membranes in simple shear flow: Large deformations and the effect of capsule viscosity, J. Fluid Mech., 361:117-143, 1998.

Rao, P. R., Zahalak, G. I. and Sutera, S. P., Large deformations of elastic cylindrical capsules in shear flows, J. Fluid Mech., 179: 283-305, 1994.

Rioual, F., Biben, T. and Misbah, C., Analytical analysis of a vesicle tumbling

Russell, D. and Wang, Z. J., A Cartesian grid method for modeling multiple moving objects in 2D incompressible viscous flow, J. Comput. Phys., 191: 177-205, 2003.

Saiki E. M. and Biringen, S., Numerical simulation of a cylinder in uniform flow: Application of a virtual boundary method, J. Comput. Phys., 123: 450-465, 1996.

Schmid-Schönbein, H. and Wells, R. E., Fluid drop like transition of erythrocyte under shear stress, Science, 165: 288-291, 1969.

Sheth, K. and Pozrikidis, C., Effects of inertia on the deformation of liquid drops in simple shear flow, Comput. Fluids, 24: 101-119, 1995.

Shrivastava, S. and Tang, J., Large deformation finite element analysis of non-linear viscoelastic membranes with reference to thermoforming, J. Strain Anal., 28: 31-51, 1993.

Shu, C., Niu, X. D. and Chew, Y. T., Taylor-series expansion and least squares-based lattice Boltzmann method: Two-dimensional formulation and its applications, Phys. Rev. E., 65: 036708, 2002.

Skalak, R., Tozeren, A., Zarda, R. P. and Chien, S., Strain energy function of red blood cell membranes, Biophys. J., 13: 245-264, 1973.

Skotheim, J. M. and Secomb, T. W., Red blood cells and other nonspherical capsules in shear flow: oscillation dynamics and the tank-treading-to-tumbling transition, Phys. Rev. Lett., 98: 078301, 2007.

Steigmann, D. J. and Ogden, R. W., Plane deformations of elastic solids with intrinsic boundary elasticity, Proc. R. Soc. London A, 453: 853-877, 1997.

Succi, S., Benzi, R. and Higuera, F., The lattice Boltzmann equation- A new tool for computational fluid dynamics, Physica D, 47: 219-230, 1991.

Sui, Y., Chew, Y. T., Roy, P. and Low H. T., A hybrid immersed-boundary and multi-block lattice Boltzmann method for simulating fluid and moving-boundaries interactions, Int. J. Numer. Meth. Fluids, 53: 1727-1754, 2007.

Sui, Y., Chew, Y. T. and Low, H. T., A lattice Boltzmann study on the large deformation of red blood cells in shear flow, Int. J. Mod. Phys. C, 18: 993-1011, 2007.

Sui, Y., Chew, Y. T., Roy, P., Chen. X. B. and Low H. T., Transient deformation of elastic capsules in shear flow: effect of membrane bending stiffness, Phys. Rev. E, 75: 066301, 2007.

Sui, Y., Low, H. T., Chew, Y. T. and Roy, P., Tank-treading, swinging and tumbling of liquid-filled elastic capsules in shear flow, Phys. Rev. E, 77: 016310, 2008.

Sui, Y., Chew, Y. T., Roy, P. and Low H. T., Inertia effect on the transient deformation of elastic capsules in simple shear flow, Comput. Fluids, 38: 49-59, 2009.

Sui, Y., Chew, Y. T., Roy, P. and Low, H. T., A hybrid method to study flow-induced deformation of three-dimensional capsules, J. Comput. Phys., 228: 6351-6371, 2008.

Sun, C., Simulations of compressible flows with strong shocks by an adaptive lattice Boltzmann model, J Comput Phys, 161:70 – 84, 2000.

Teixeira, C. M., Incorporating turbulence models into the lattice-Boltzmann method, Int. J. Mod. Phys. C, 9: 1159-1175, 1998.

Tran-Son-Tay, R., Sutera, S. P. and Rao, P. R., Determination of red blood cell membrane viscosity from rheoscopic observations of tank-treading motion, Biophys. J., 46: 65-72, 1984.

Unverdi, S. O. and Tryggvason, G., A front-tracking method for viscous, incompressible, multi-fluid flows, J. Comput. Phys., 100: 25-37, 1992.

Walter, A., Rehage, H. and Leonhard, H., Shear induced deformation of microcapsules: shape oscillations and membrane folding, Colloids Surf. A, 183–185: 123-132, 2001.

Wang, Z. J., Two dimensional mechanism for insect hovering, Phys. Rev. Lett., 85: 002216, 2000.

Xu, S. and Wang, Z. J., An immersed interface method for simulating the interaction of a fluid with moving boundaries, J. Comput. Phys., 216: 454-493, 2006.

Yan, G., Chen, Y. and Hu, S., Simple lattice Boltzmann model for simulating flows with shock wave, Phys Rev E, 59:454 – 459, 1999.

Yu, D., Mei, R., Luo, L. and Shyy, W., Viscous flow computations with the method of lattice Boltzmann equation, Progress in Aerospace Sciences, 39: 329-367, 2003.

Yu, D., Mei, R. and Shyy, W., A multi-block lattice Boltzmann method for viscous fluid flows, Int. J. Numer. Meth. Fluids, 39: 99–120, 2002.

Yu, D. and Girimaji, S. S., Multi-block lattice Boltzmann method: Extension to 3D and validation in turbulence, Physica A., 362: 118-124, 2006.

Yu, H., Luo, L.-S. and Girimaji, S.S., LES of turbulent square jet flow using an MRT lattice Boltzmann model, Comput. Fluids, 35: 957-965, 2006.

Yue, P., Feng, J. J., Bertelo, C. A. and Hu, H. H., An arbitrary Lagrangian-Eulerian method for simulating bubble growth in polymer foaming, J. Comput. Phys., 226: 2229-2249, 2007.

Zhou, H. and Pozrikidis, C., Deformation of liquid capsules with incompressible interfaces in simple shear flow, J. Fluid Mech., 283: 175-200, 1995.